

SnO₂(110) and Nano-SnO₂:
Characterization by Surface Analytical Techniques



SnO₂(110) und Nano-SnO₂:
Charakterisierung mit oberflächenspektroskopischen Methoden

DISSERTATION

der Fakultät für Chemie und Pharmazie der
Eberhard-Karls-Universität Tübingen

zur Erlangung des Grades eines Doktors
der Naturwissenschaften

2000

vorgelegt von

Martin Sinner-Hettenbach

Tag der mündlichen Prüfung:	8. Dezember 2000
Dekan:	Prof. Dr. Hansgeorg Probst
1. Berichterstatter:	Prof. Dr. Christiane Ziegler
2. Berichterstatter:	Prof. Dr. Klaus-Dieter Schierbaum

*für Katrin
und meine Eltern*

Contents

1	Introduction	11
I	Basics	15
2	Description of the Model System	19
2.1	Single Crystals	20
2.1.1	Growing SnO ₂ Single Crystals, an Overview	21
2.1.2	Helbig Method	21
2.2	SnO ₂ (110)	22
2.2.1	Preparation of clean Surfaces	23
2.2.2	Theoretical Approaches to the bare SnO ₂ (110) Surface	29
2.2.3	Interaction of Metals with SnO ₂ (110)	32
2.2.4	Adsorbate Systems	34
2.3	Polycrystalline SnO ₂	39
2.3.1	XPS Studies	40
2.3.2	Synchrotron Radiation Studies	40
2.3.3	Electronic Structure of Stannous Oxide	41
3	Measurement Techniques	43
3.1	Chemical Composition of a Surface	43
3.1.1	Photoelectron Spectroscopy (XPS / UPS / SRPES)	43
3.1.2	Auger Electron Spectroscopy (AES)	57
3.1.3	Instrumentation for Electron Spectroscopy	57
3.1.4	Secondary Ion Mass Spectrometry (SIMS)	61
3.2	Geometrical Information	61
3.2.1	Scanning Tunneling Microscopy (STM)	62
3.2.2	Low Energy Electron Diffraction (LEED)	63
II	Experimental	69
4	Sample Preparation	73

4.1	Sample Preparation of Single Crystalline SnO ₂	73
4.2	Thick Film Sensors	76
4.2.1	Production of SnO ₂ Nanocrystals by a Sol-Gel Method	76
4.2.2	Sensor Fabrication	78
5	Spectrometers	81
5.1	XPS / UPS / LEED	81
5.2	STM / LEED	82
5.3	MAXlab, Beamline I311	83
6	Data Evaluation	85
6.1	Factor Analysis	85
6.2	Peak Fitting	86
III	Results and discussion	89
7	Geometric Structure	93
7.1	Reconstruction Process	94
7.1.1	Monitoring the Reconstruction Process by XPS and LEED	97
7.2	STM Imaging	100
7.2.1	Atomically resolved Imaging on SnO ₂ (110)-4×1	101
7.2.2	STM on highly defective SnO ₂ (110)	105
7.2.3	Pd-Clusters on SnO ₂ (110)-4×1 imaged by STM	109
7.3	Discussion	110
8	Electronic Structure and Chemical Composition	113
8.1	SnO ₂ (110)	114
8.1.1	SRPES Core-Level Spectroscopy	114
8.1.2	ResPES on SnO ₂ (110)-4×1 and Sputtered SnO ₂ (110)	116
8.2	Nanocrystalline SnO ₂	126
8.2.1	Laboratory Source UPS Results	128
8.2.2	ResPES on doped and undoped Gas Sensors	129
8.3	CO Exposure monitored by UPS	140
9	Conclusions and Outlook	143
	Appendix	163
	List of Publications	163
	Danksagung	165
	Liste der akademischen Lehrer	166
	Lebenslauf	167

List of Abbreviations

$\Delta\chi$	Electron affinity difference
$\Delta\Phi$	Work function difference
AES	Auger Electron Spectroscopy
ARUPS	Angular Resolved Ultraviolet Photoelectron Spectroscopy
BIAS	Auxiliary voltage
CB	Conduction Band
CIS	Constant Initial State
CMA	Cylindrical Mirror Analyzer
CVD	Chemical Vapor Deposition
DOS	Density of States
EDC	Energy Distribution Curve
ESCA	Electron Spectroscopy for Chemical Analysis
FA	Factor Analysis
FFT	Fast Fourier Transform
FT-IR	Fourier Transform Infrared spectroscopy
FWHM	Full Width Half Maximum
GC	Gas Chromatography
GC-MS	Gas Chromatography - Mass Spectrometry
GGA	General Gradient Approximation

HMA	Hemispherical Analyzer
HRTEM	High Resolution Transmission Electron Microscopy
HV	High Vacuum
IMFP	Inelastic Mean Free Path
ISS	Ion Surface Scattering
ITO	Indium Tin Oxide
LDA	Local Density Approximation
LEED	Low Energy Electron Diffraction
NC-AFM	Non-Contact Atomic Force Microscopy
PCA	Principal Components Analysis]
PVD	Physical Vapor Deposition
ResPES	Resonant Photoemission Spectroscopy
RFA	Retarding Field Analyzer
SEM	Scanning Electron Microscopy
SIMS	Secondary Ion Mass Spectrometry
SRPES	Synchrotron Radiation Photoelectron Spectroscopy
SSIMS	Static Secondary Ion Mass Spectrometry
STM	Scanning Tunnelling Microscopy
SXES	Soft X-ray Emission Spectroscopy
S&A	Sputtering and Annealing

TEM..... Transmission Electron Microscopy

TPD..... Temperature Programmed Desorption

UHV..... Ultrahigh Vacuum

UPS..... Ultraviolet Photoelectron Spectroscopy

VB..... Valence Band

XPS..... X-ray Photoelectron Spectroscopy

Chapter 1

Introduction

Controlling of the ambient air in our environment, at work or at home, is a demanding task of the present time. Therefore, a number of approaches has been developed to reveal the chemical composition of our ambient air or to detect specific – potentially poisonous – compounds.

Among optical and chemical spectroscopy like FT-IR or GC/GC-MS, easily applicable methods are needed for a continuous, fast and inexpensive monitoring of the air we are living in. For portable operation and compact design, electrical transducers soon turned out to be best suited. Electrochemical cells, quartz microbalance sensors and metal oxide based gas sensors are a promising approach to either detect the specific amount of a single gas component or to get an integrated signal of all reducing or oxidizing gases present in the environment. Gas sensors used for the sensing of reducing or oxidizing gases based upon SnO_2 are well-suited to fit in this demand for a fast, sensitive, accurate and inexpensive determination of gas compositions in our environment, during industrial processes or for automotive applications.

Motivation

A detailed understanding of the physical properties of SnO_2 , which are relevant for gas-interaction, is necessary for understanding and systematically improving SnO_2 gas sensors. Since gases are interacting only with the uppermost atomic layers, a characterization of the material's surface is

the first step. But this interest in the surface properties of SnO₂ grows not only from gas sensing applications but also from its use as a base material for transparent electrodes, for example in solar cells, in electrochemistry or for heatable windows [98].

Investigating gas interaction and surface properties of real gas sensors is a challenging task and requires a model system, as easy as possible, to study basic chemical and physical parameters. A common approach to investigate a given material's surface is the application of surface science techniques to single crystal surfaces characteristic of the material. Well-defined surfaces offer the possibility to investigate fundamental surface properties on almost perfect surfaces. For this reason, a common approach is to choose the single crystal surface corresponding to the most frequent surface plane of the material and to study its chemical, electronic and geometric properties under UHV conditions. Nevertheless, the comparability to experiments under realistic conditions has been controversially discussed. In fact, the relevance of experiments in UHV to corresponding reactions in heterogeneous catalysis or gas sensor responses has only been proven in few cases like the reaction of CO on metal and metal oxide surfaces or the catalytic synthesis of NH₃ [6, 59, 60, 71–74, 132].

In spite of these restrictions on the comparison with surfaces under real, i.e. atmospheric conditions, the application of surface sensitive spectroscopy on single crystal surfaces, is the only approach to find fundamental correlations between electronic and geometric surface properties. Of course, not only the restriction to clean surfaces under UHV conditions, but also assuming it to be a perfect surface, is critical. It is essential to assume that observed phenomena are not dominated by surface defects like vacancies, step edges, crystallographic shear planes etc. since such surface defects are still present even after extensive preparation treatment.

Objectives

It is the emphasis of this study to investigate geometric and electronic surface properties of SnO₂ single crystal surfaces and to determine comparative data on SnO₂ gas sensors.

For this reason, two model systems were chosen to be characterized by surface science techniques. On the one hand, the SnO₂(110) single crystal surface as the thermodynamically

most stable surface termination [75] was investigated in detail by STM (Scanning Tunneling Microscopy), LEED (Low Energy Electron Diffraction) and photoemission spectroscopy. On the other hand, gas sensors based upon nanocrystalline grains of doped and undoped SnO₂ were investigated by photoemission spectroscopy and SIMS (Secondary Ion Mass Spectrometry). These sensors had already proved a very high reproducibility in gas test measurements of the sensor's resistance and the work function of the surface under ambient air conditions.

Characterizing fundamentally the surface properties is essential for an understanding of the interaction of as-prepared surfaces with incoming gas molecules, as for example in adsorption processes or catalytic reactions. Furthermore, such a knowledge is the prerequisite for any systematic study with surface sensitive methods on gas loaded surfaces. The electronic and geometric properties are especially important for gas sensing since gas interaction may lead to a change in the band bending, electron affinity or to an injection of charge carriers in the semiconducting tin oxide, which finally results in an electrical resistance change of the material, i.e. in a sensor response that can be used for gas detection.

In this way detailed measurements of single crystal surfaces of the best available quality form the basis for further investigation of the SnO₂ gas sensors by photoemission spectroscopy and for a comparative discussion of the results obtained by both model systems.

Structure of the Thesis

In the first part of the thesis called 'Basics', the model systems, SnO₂(110) and SnO₂ gas sensors based upon nanocrystalline material, are described. Starting with methods to grow single crystals of SnO₂, the preparation of clean surfaces and studies on such surfaces, as well as on gas and metal interaction are discussed. In the following, the measurement techniques applied on the model systems are described and discussed towards their benefits and restrictions.

The second part, 'Experimental', deals with details of the sample preparation, with the data evaluation techniques applied to the photoemission spectra and with the UHV equipment used in this study.

The third part concerns the 'Results and Discussion'. Starting with the geometric properties

of reduced $\text{SnO}_2(110)$, revealed by STM and LEED, results by photoemission spectroscopy on well-defined surfaces are shown. Comparative data collected on undoped and doped SnO_2 gas sensors are discussed following after the single crystal measurements. Finally the results of this study are compared and rated to the present knowledge on these model systems and conclusions as well as an outlook are given.

Part I

Basics

Table of Contents

2	Description of the Model System	19
2.1	Single Crystals	20
2.1.1	Growing SnO ₂ Single Crystals, an Overview	21
2.1.2	Helbig Method	21
2.2	SnO ₂ (110)	22
2.2.1	Preparation of clean Surfaces	23
	Oxidized Surface	23
	Annealing and Reconstruction Process of Oxygen-deficient SnO ₂	25
	Models for Reconstructed Surfaces	26
2.2.2	Theoretical Approaches to the bare SnO ₂ (110) Surface	29
	Relaxations	29
	Electronic Structure	30
2.2.3	Interaction of Metals with SnO ₂ (110)	32
	Palladium as Model System for Catalysis	32
	Pd on SnO ₂ (110)	33
	Other Metals deposited onto SnO ₂	34
2.2.4	Adsorbate Systems	34
	CO on SnO ₂ (110)	34
	H ₂ O on SnO ₂ (110)	36
	Hydrocarbons on SnO ₂ (110)	39
2.3	Polycrystalline SnO ₂	39
2.3.1	XPS Studies	40
2.3.2	Synchrotron Radiation Studies	40
2.3.3	Electronic Structure of Stannous Oxide	41
3	Measurement Techniques	43
3.1	Chemical Composition of a Surface	43

3.1.1	Photoelectron Spectroscopy (XPS / UPS / SRPES)	43
	Principle of Photoelectron Spectroscopy	44
	Mean free Path of Electrons	46
	Photoionization Cross-Sections	47
	Effects of Photon Momentum	51
	Resonance Effects due to Electronic Transitions (Fano-type Resonance) .	52
	Phenomenological Quantities revealed by UPS Spectra	56
3.1.2	Auger Electron Spectroscopy (AES)	57
3.1.3	Instrumentation for Electron Spectroscopy	57
	Hemispherical Analyzer (HMA)	58
	Cylindrical Mirror Analyzer (CMA)	58
	Light Sources for Photoelectron Spectroscopy	59
3.1.4	Secondary Ion Mass Spectrometry (SIMS)	61
3.2	Geometrical Information	61
3.2.1	Scanning Tunneling Microscopy (STM)	62
	STM: Principle of Operation	62
3.2.2	Low Energy Electron Diffraction (LEED)	63
	Diffraction by a two-dimensional Lattice	64
	Description of Overlay Structures	65
	LEED: Principle of Operation	65

Chapter 2

Description of the Model System

SnO_2 is a wide band gap n-type semiconductor, which crystallizes in the rutile structure (tetragonal structure, space group D_{4h}^{14} or – in another notation – $P4_2/mnm$) like for example TiO_2 , CeO_2 or GeO_2 [136]. The unit cell of SnO_2 contains six atoms, two tin and four oxygen atoms.

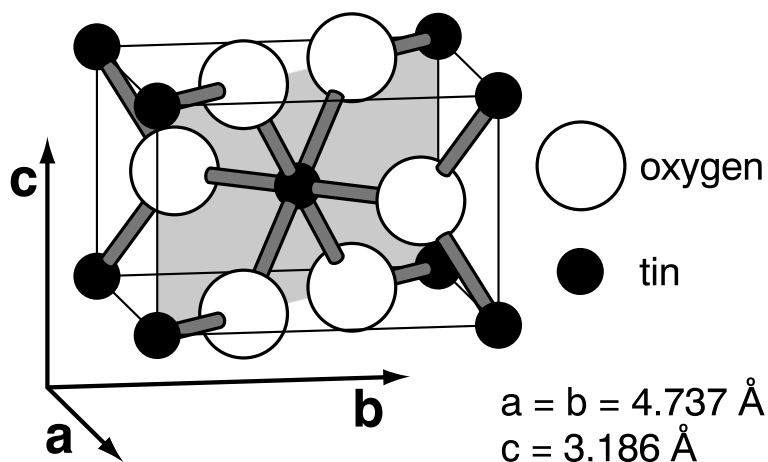


Figure 2.1: Unit cell of SnO_2 . The shaded area represents the (110) surface [4, 13].

With an optical band gap of 3.6 eV, this material has a low conductivity at room temperature. But its conductivity can be increased by introducing dopants that also are of importance to tailor SnO_2 based gas-sensors to higher sensitivity and selectivity towards gases of interest. Dopants used are for example In [98], Pd [17, 48], Pt [92], Sb [40] or V [39].

With its unique properties, SnO_2 is paid attention in a variety of applications [83–85]. Its

high conductivity (as doped material, ITO: Indium Tin Oxide) together with transparency makes it an ideal material for producing transparent electrodes, very important for example for solar cells or heatable windows. On the other hand, it is widely used in gas sensor production because of its chemical stability and its semiconducting properties and is yet unsurpassed in its sensitivity to reducing and oxidizing gases. A huge effort has been made in empirical optimization of this material by varying for example dopants, amount of doping, sintering conditions, grain size and operating temperature.

The first SnO₂ based gas sensors were developed by Taguchi [155–157] in the 60s and sensors of this company are still among the leading SnO₂ gas sensors.

In the following, the two types of SnO₂ material investigated in this study are described and the present knowledge about these two systems is summarized. On the one hand, there is the single crystal SnO₂(110) surface, which is – as the thermodynamically most stable face – the predominant termination of SnO₂ either in the case of macroscopic crystals [161] or in the nanoscopic scale and therefore a well-suited model system for SnO₂.

On the other hand, there are the sensors based on nanocrystalline material. These sensors have already proven to be highly sensitive and tunable to high selectivity by varying dopants and operating parameters under ambient air conditions.

2.1 Single Crystals

Despite the importance of SnO₂(110) surfaces as a model system for which the availability of single crystals is a prerequisite, only few successful attempts for growing single crystals have been made. To the author's knowledge almost all SnO₂(110) samples used in UHV studies can be traced back to the crystal growing experiments of two groups. One at the University of Erlangen-Nürnberg (Prof. R. Helbig) and the other at the LASMOS (Laboratoire de Spectroscopie Moléculaire de Surface) in Belgium.

Both groups applied the same method, a gas phase transport of SnO with reoxidation in the gas phase (see section 2.1.2).

Additionally, there is to the author's knowledge only one publication existing based upon

a SnO₂(110) slice which was cut from a natural single crystal (cassiterite) [103]. The reconstruction process of this natural single crystal surface shows the same behavior under sputtering and annealing (S&A) as it is reported from SnO₂(110) slices cut from artificially grown single crystals. Therefore it can be assumed that this behavior is true for every well-defined SnO₂(110) surface.

In the following, only a short overview how SnO₂ single crystals can be grown, is given. The main emphasis lies on the method for growing the single crystals which are used in this study.

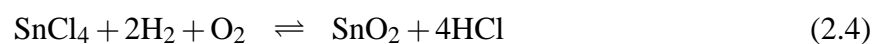
2.1.1 Growing SnO₂ Single Crystals, an Overview

In order to grow SnO₂ single crystals, temperatures of up to 1650°C under an O₂ atmosphere are needed. This causes immense problems, not only for the furnace but also for ensuring a high purity of the crystals.

One general attempt is to evaporate SnO₂ or SnO which leads – in both cases – to SnO in the gas phase, to reoxidize it and precipitate it onto a substrate.



The other attempt uses SnCl₄ as precursor and convert it under reaction with H₂O to SnO₂. It is the same reaction mechanism as used for the wet chemical method to obtain SnO₂ powder.



The drawback in this case is the higher impurity level in the crystals due to aggressive HCl in the gas phase [83, 161].

2.1.2 Helbig Method

This method uses the gas phase reaction described above. In order to lower the sublimation temperature to 1450°C, the reaction is supported by H₂.

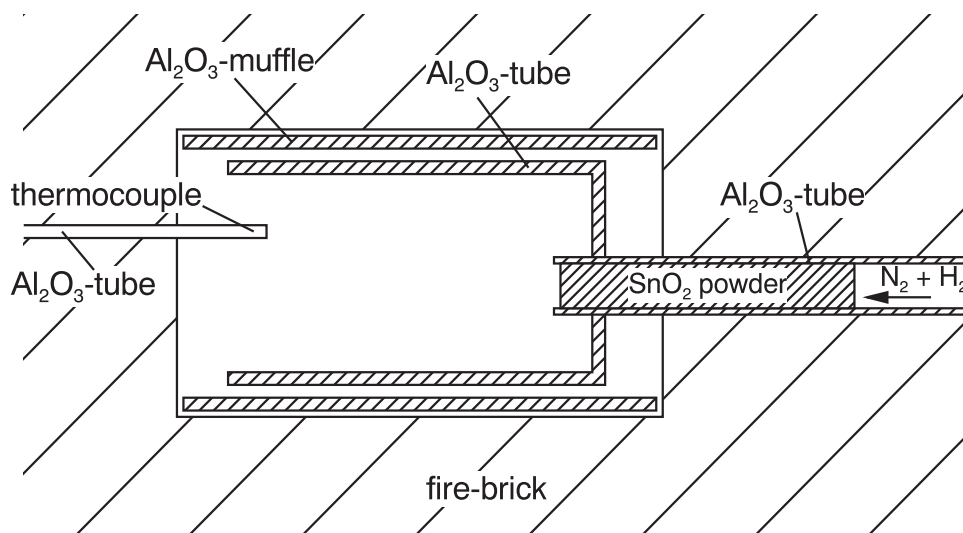


Figure 2.2: Scheme for the furnace used in the crystal growing experiments by Thiel and Helbig [161].

The hydrogen leads to a reduced partial pressure of O₂ in the sublimation region and therefore increases the partial pressure of SnO in the gas phase at a given temperature. The vaporized SnO is transported by a N₂ flow to the growth region where it reoxidizes to SnO₂ just by the oxygen which diffuses through the walls of the furnace.

After a typical growing time of 70 h, needle shaped crystals up to a size of $7 \times 7 \times 20 \text{ mm}^3$ are obtained with the (110) face as the predominant termination [161, 163].

The impurity concentrations were checked by emission and mass spectroscopy and were in the order of maximum 100 ppm in the case of Fe and Na.

2.2 SnO₂(110)

As the thermodynamically most stable surface, the 110 surface of SnO₂ has been paid wide attention as a model system for SnO₂ gas sensors. Since SnO₂ single crystals of sufficient size are rare, there are only few studies in comparison to other metal oxides (for example TiO₂, ZnO, MgO), which have been studied in detail during the last two centuries [73].

Nevertheless, a number of interesting publications concerning the electronic and geometric

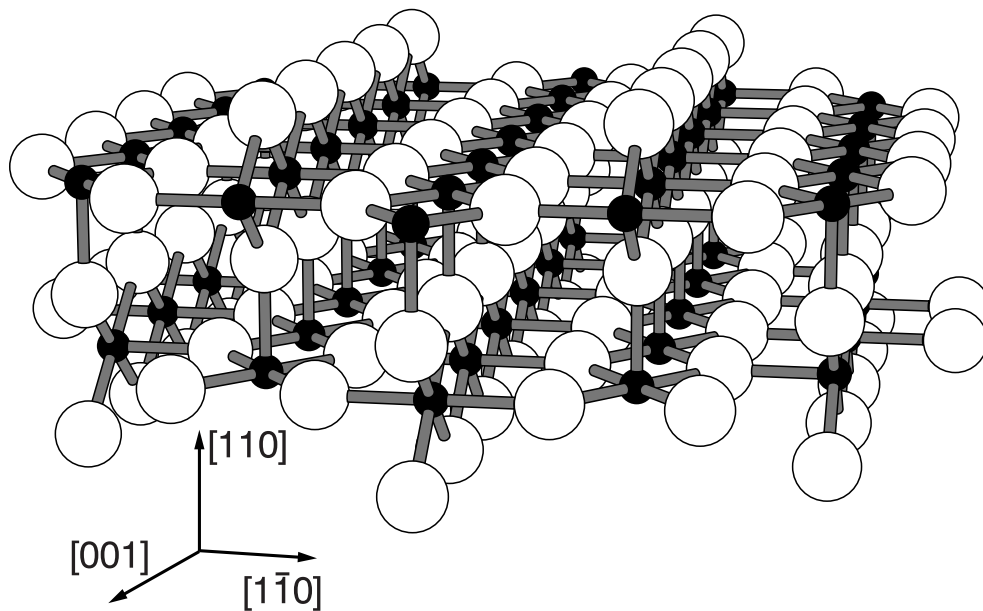


Figure 2.3: Stoichiometric SnO₂(110) surface.

structure of SnO₂(110) is existing.

2.2.1 Preparation of clean Surfaces

In general, two approaches for preparing clean and well-defined SnO₂(110) surfaces can be distinguished. On the one hand, the sputtered and UHV-annealed (S&A) and therefore oxygen-deficient surface and on the other hand the oxidized, stoichiometric surface.

Oxidized Surface

In order to prepare an oxidized SnO₂ surface, three different methods are used in the literature:

1. Thermal oxidation at 700 K and an O₂-pressure of at least 0.7 mbar for about 10 min [16, 18, 25, 103]
2. Thermal oxidation at 700 K by using N₂O as oxidant at about $7 \cdot 10^{-1}$ mbar [50–52]
3. Plasmaoxidation at room temperature [16, 18]

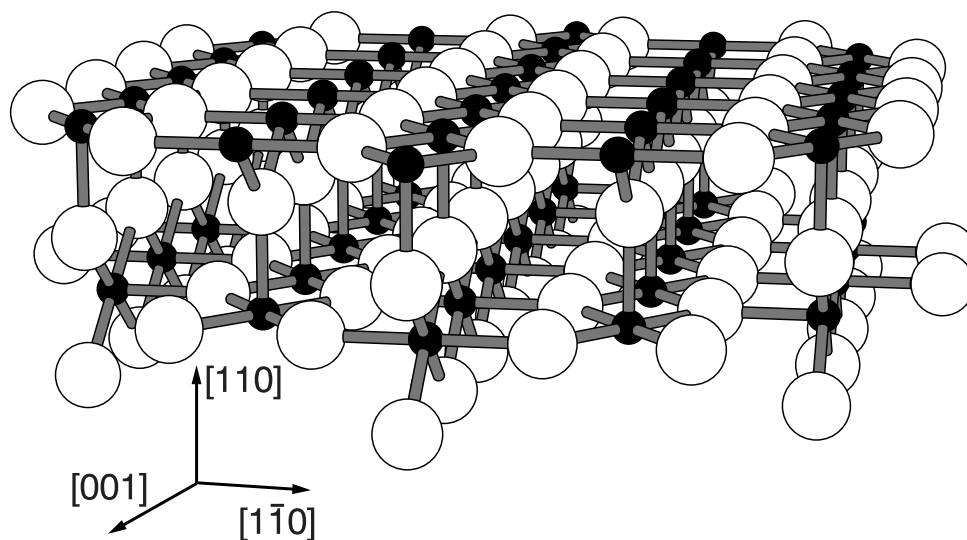


Figure 2.4: Reduced $\text{SnO}_2(110)$ surface.

'1.' is the most frequently used oxidation procedure. Nevertheless, the other two methods have some advantages. Oxidation by method '2.' has the advantage of lower oxidation pressure (N_2O is a stronger oxidant than O_2) and therefore pump-down faster after oxidation treatment. Additionally, the typical impurities of N_2O (N_2 , O_2 , CO and CH_4) can more easily be pumped out of the high-pressure cell than for example water which is a main contaminant in high-purity oxygen.

The plasma oxidation leads to a more oxygen-rich surface concluded from He I-UPS spectra [18] than the thermal oxidation procedure, but it is more difficult to apply and was only used by one group.

The oxidized surface can be illustrated by figure 2.3, where the bridging oxygen rows are complete. An as-prepared surface shows a 1×1 LEED pattern although it is reported that it is sometimes difficult to get a clear LEED pattern because of surface charging. A stoichiometric surface will lose its bridging oxygens (see figure 2.4) after heating to 700 K, but the LEED pattern remains the same [51]. Further heating removes in-plane oxygens and leads to an increased defect density. ISS measurements show that the O/Sn-ratio of the oxidized surface is decreased from 1 to about 0.2 during heating up to 1000 K whereas the O/Sn ratio of the S&A surface stays constant at below 0.1 and increases to 0.15 at 1100 K [25] (see figure 2.5).

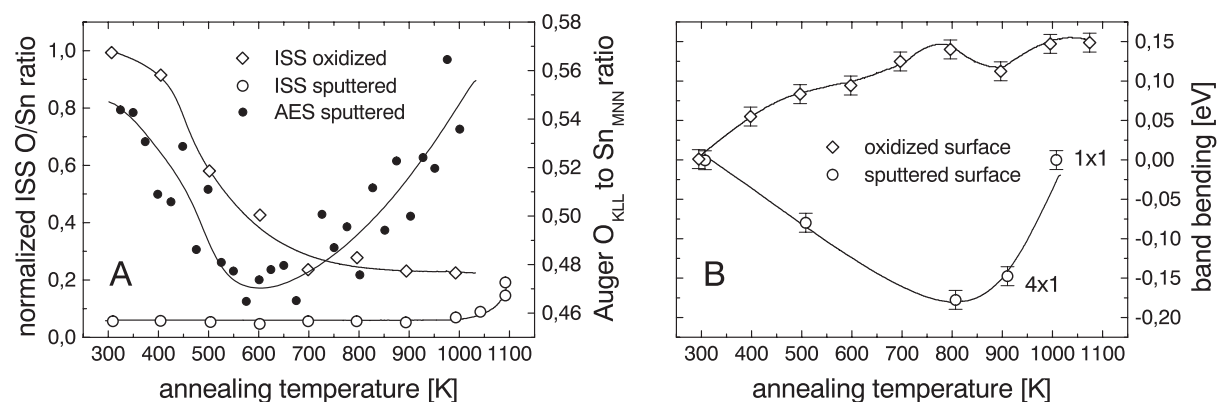


Figure 2.5: Annealing process of oxidized and ion-bombarded SnO₂(110) observed by LEED, ISS, AES, and UPS (band bending of the valence band maximum). Figure A refers to O/Sn ratios revealed either by ISS, i.e. sensitive only to the uppermost monolayer, or by AES, i.e. information depth of some monolayers. In figure B the band bending of oxidized and sputtered SnO₂(110) during annealing is shown. For further details and experimental conditions see references [25, 27, 143].

Annealing and Reconstruction Process of Oxygen-deficient SnO₂

The reconstruction process of oxygen-deficient annealed SnO₂(110) surfaces has been described in various publications [23, 25–27, 33–35, 42, 89, 117, 146, 147, 152–154, 160]. After sputtering, the surface undergoes some diffuse ordering at annealing temperatures between 500 K and 800 K described by a $c(2 \times 2)$ -pattern [27, 33, 34], leading to the most prominent 4×1 [27, 33, 34, 89, 146] (at about 900 K) and 1×1 surfaces [25, 27, 33, 34, 146] (1000 K). The high-temperature 1×2 -reconstruction at 1050–1200 K was not often observed [27, 81, 117, 143] and it was speculated to be induced by some sort of impurity as suggested by Cox et al. [27]. The centered spot at low annealing temperatures implies a strong two dimensional disorder in both, the $[\bar{1}10]$ and the $[001]$ direction, resulting from the previously applied ion-bombardment. This assumption can be demonstrated by optical transforms [27].

It is generally assumed that the reconstruction of the surface is driven at lower temperatures ($500 \text{ K} < T < 800 \text{ K}$) by an outdiffusion of Sn from tin-rich regions (enriched by preferential sputtering of oxygen [38]) with an outdiffusion of oxygen at higher temperatures that leads to

ordered and less defective surface structures. Evidence for this model is given by AES [27, 33] and ISS [27] measurements and from ISS measurements on oxidized $\text{SnO}_2(110)$ with ^{18}O -isotopic labeling [23].

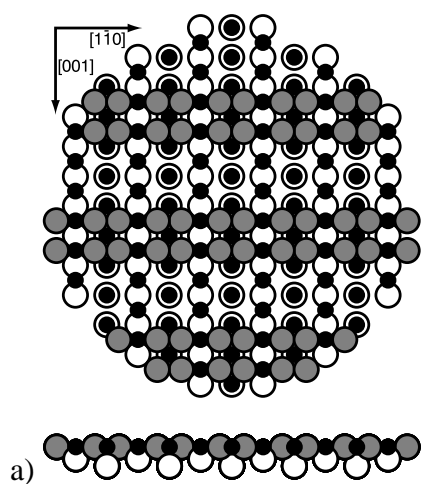
The measurements shown in figure 2.5 refer to ISS, AES and UPS data recorded by Cox, Fryberger and Semancik [25, 27, 143]. Most remarkable is the shape of the AES O/Sn ratio compared to the ISS O/Sn ratio in figure 2.5 A. The AES ratio shows a strong dependency as a function of annealing temperature, whereas the corresponding ISS ratio of the sputtered and annealed surface stays almost constant. When considering the information depth of these two methods, it can be clearly understood that the O/Sn ratio of the surface is more or less unaffected by the reconstruction process whereas the subsurface region is the subject of strong diffusion. The slight increase of the ISS ratio at highest annealing temperature indicates the beginning of the formation of the 1×2 termination which is – according to the model of Pang et al. [117] – determined by a loss of in-plane tin atoms (see table 2.2.1 f) and therefore by an increase in the surface O/Sn ratio.

Models for Reconstructed Surfaces

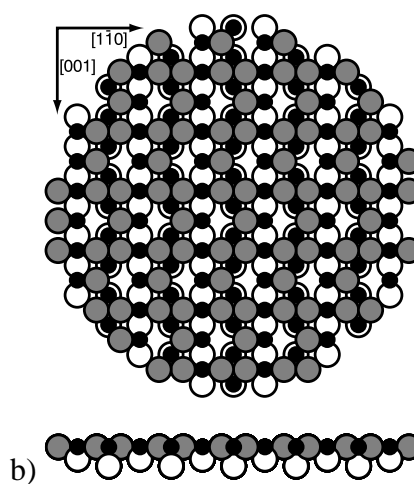
The three most prominent reconstruction symmetries of the $\text{SnO}_2(110)$ surface are the 1×1 , the 4×1 and the 1×2 reconstruction.

The 1×1 symmetry can be observed either on the stoichiometric (oxidized) surface, on a subsequently heated as-prepared surface under loss of surface oxygen or on S&A prepared surfaces as a diffuse pattern at low annealing temperatures and as clear LEED pattern at temperatures beyond the 4×1 reconstruction.

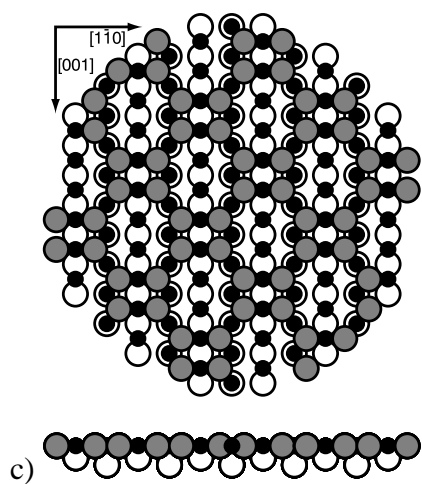
The 4×1 reconstruction has only been observed on S&A treated surfaces so far and several models to interpret this pattern have been proposed. Finally, the 1×2 at the very high temperature end of annealing treatment is considered to have a higher O/Sn ratio on the surface (by ISS) and actually has not been observed in many studies (probably because of restrictions in available heating power). In some publications, it is proposed that this termination may be stabilized by some sort of impurity.



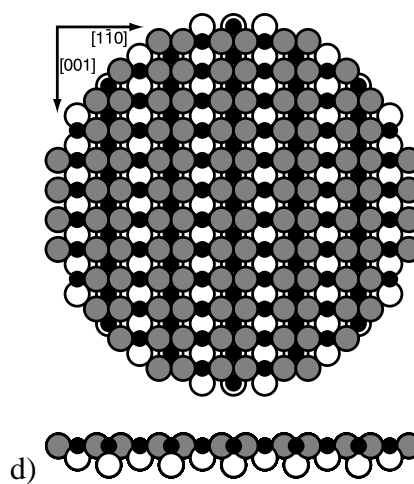
4×1 according to de Frésart et al. [33]. The high oxygen deficiency makes this model very unlikely.



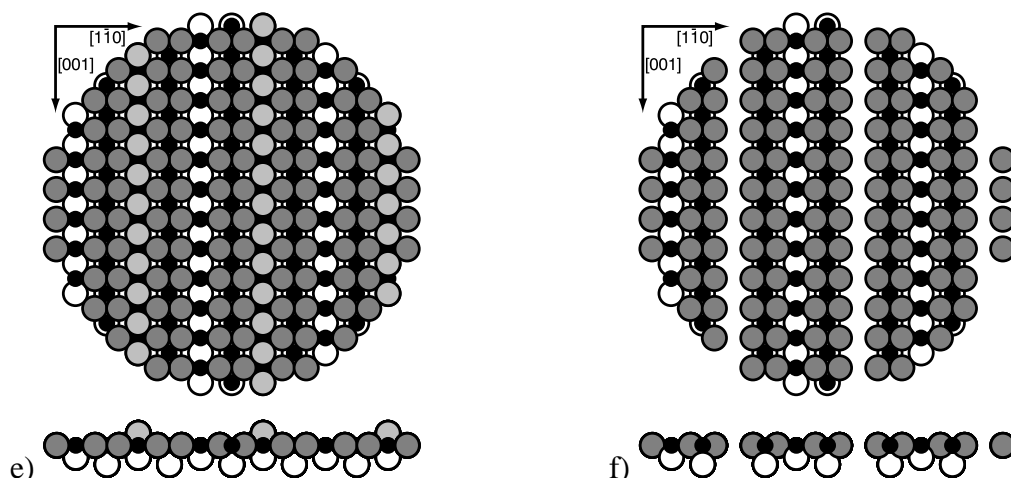
4×1 model that delivers a possible interpretation for STM results by Jones et al. [89] and Thornton [117].



c(4×2) proposed by de Frésart et al. [33].

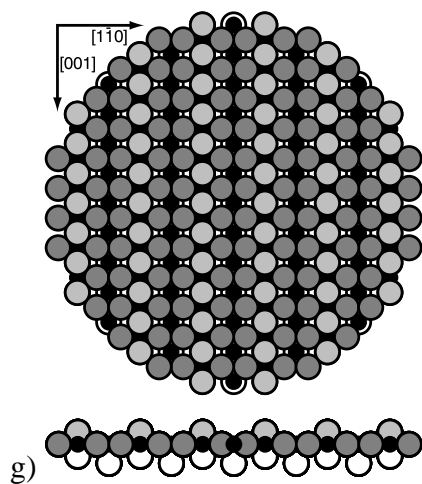


1×1 resulting from either removal of bridging oxygens or of high-temperature annealing a S&A surface [23, 25, 50–52, 147].



1×2 consisting of every second bridging oxygen row left on the surface [147].

Model for the 1×2 proposed by Pang et al. which is consistent with STM and NC-AFM results [117].



Stoichiometric SnO₂ prepared either by high pressure (1 mbar O₂ [25] or 0.1 mbar N₂O [50–52] at 700 K) or plasma oxidation [18].

Table 2.1: Models for SnO₂ reconstructions. Two other models that should be mentioned are a coincidence SnO(101) overlayer leading to a 4×1 and an imperfectly ordered atomic arrangement to explain the diffuse centered spot in the c(2×2) pattern [27].

While the existence of a 1×1 LEED pattern on oxidized surfaces is very straight-forward as well as the resulting 1×1 by removal of the bridging oxygens at moderate temperatures, the freshly sputtered surface shows a much more complicated behavior, especially when regarding O/Sn ratios revealed by ISS and AES (see figure 2.5). Nevertheless, it is assumed that an as-prepared surface would consist of ordered surface areas with a significantly higher in-plane defect density than the 1×1 mentioned above.

For interpreting the 4×1 surface, the first model proposed (see table 2.1 b)) can be ruled out because of newer results which are not consistent with the high oxygen deficiency proposed in this model. It would also contain strongly reduced tin atoms which may lead to metallic states that are not observable in XPS core-level spectroscopy. Another model suggests a coincidence overlayer of SnO(101) which would fit with reasonable stretching of the unit cell in the order of 10% to the SnO₂(110) termination. Such a surface would fulfill the requirements of O/Sn ratio and chemical stability. The latest model proposed is an alternating removal of in-plane oxygens leading to a characteristic pattern which was observed in STM experiments.

For the 1×2 symmetry two possibilities are discussed. On the one hand, the evolution of bridging oxygen rows at every second row by increasing outdiffusion of oxygen from the bulk and on the other hand the complete removal of bridging tin with underlying oxygen in every second row. The latter model is supported by STM and NC-AFM imaging.

2.2.2 Theoretical Approaches to the bare SnO₂(110) Surface

Between 1982 and 1987 Munnix and Schmeits studied the SnO₂(110) surface, point defects and oxygen vacancies on this surface and the resulting electronic structure [107–111] by a scattering-theoretical method. Since computer power has increased rapidly since then, only recent studies are treated in the following.

Relaxations

Relaxations of surface atoms relative to their bulk position were theoretically treated in detail by a periodic [58, 106] and a cluster approach [123–128]. The results of these calculations on the

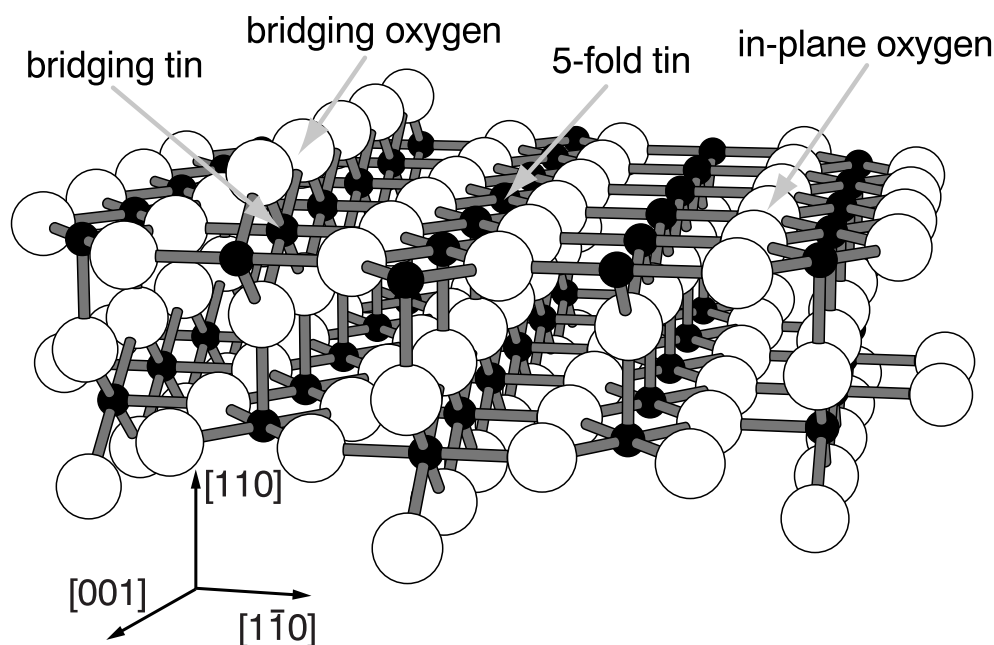


Figure 2.6: Nomenclature for atomic positions (relaxations relative to bulk positions are not considered in this picture).

stoichiometric and reduced $\text{SnO}_2(110)$ surface (see figure 2.6) are shown in table 2.2 and 2.3.

The results correspond well to each other for the stoichiometric surface. But for the reduced surface there are differences of 400–500% for the relaxations of the bridging tins and in-plane oxygens. These calculated relaxations show a significant deviation from the bulk situation. Compared to a tin to tin distance of 3.35 Å in the [110] direction of the bulk material, the deviations range up to 10%.

Electronic Structure

A detailed treatment of the electronic structure is of particular importance for the interpretation of surface spectroscopic results and real-space microscopy with STM and NC-AFM.

There are two theoretical studies on the reduced and stoichiometric $\text{SnO}_2(110)$ surface during the last few years, treating the electronic structure and density of states with methods based on an infinite, periodical approach [56, 106].

One method is based on a tight-binding, total energy approach [56] very similar to the earlier

Atoms	stoichiometric		reduced	
	Δx (Å)	Δy (Å)	Δx (Å)	Δy (Å)
Bridging tin	+0.15	0	+0.23	0
5-fold tin	-0.15	0	-0.18	0
Bridging oxygens	+0.02	0	—	—
In-plane oxygens	+0.07	+0.05	+0.08	+0.07

Table 2.2: Surface relaxations of the reduced and stoichiometric SnO₂(110) surface according to Manassidis et al. [106]. Δx refers to the relaxation in the [110] and Δy to the [1 $\bar{1}$ 1] direction.

Atoms	stoichiometric		reduced	
	Δx (Å)	Δy (Å)	Δx (Å)	Δy (Å)
Bridging tin	+0.08	0	+0.05	0
5-fold tin	-0.07	0	-0.10	0
Bridging oxygens	+0.07	0	—	—
In-plane oxygens	+0.04	+0.02	+0.45	+0.06

Table 2.3: Surface relaxations of the reduced and stoichiometric SnO₂(110) surface according to Rantala et al. [128]. Δx refers to the relaxation in the [110] and Δy to the [1 $\bar{1}$ 0] direction.

calculations of Munnix and Schmeits [107–111], the other one makes use of the DFT (density functional theory) and gives (as stated by the authors) a more detailed inside view of the surface states [106].

This study by Manassidis et al. [106] is also very useful for interpreting STM images [89] since the valence electron density is calculated for the stoichiometric, reduced, and half-reduced (110) surface. It could be shown that the electrons left from the bridging oxygens at the reduced surface are localized just above the bridging tin sites (compare to figure 2.6). With this background, the bright areas in the (4×1) STM images at +1.0 eV BIAS of Jones et al. [89] were interpreted as oxygen vacancies, assuming that the three tin ions surrounding the vacancy

provide an F-center like attractive potential, leading to a state about +1.0 eV above the Fermi level. Such an interpretation is still very speculative, since the calculations were not even based upon a 4×1 terminated surface. Nevertheless, it shows the importance of a theoretical analysis of the surface states for a proper interpretation of STM images. A realistic calculation of the 4×1 structure would be much more challenging because of the surface area which is four times larger, resulting in a higher amount of computer time needed. The latter point is, despite the rapid development of faster and faster computers, still a serious restriction for theoretical studies on complex systems.

2.2.3 Interaction of Metals with $\text{SnO}_2(110)$

Because of its gas-sensing importance the system Pd/ $\text{SnO}_2(110)$ is best investigated [16, 17, 41, 46, 47, 49], but also other metal overlayers like Sn [16, 41] or Cu [103] were studied on the (110)-surface.

There have also been a number of spectroscopic studies published which are dealing with the interaction of polycrystalline thin SnO_2 -films and powders with metallic additives. Metals have been incorporated into the SnO_2 material by evaporation, ion implantation and as a solvent during powder preparation. Metals investigated are for example Cr, Sn, Ag [115], Pd [48, 140], Pt [140], V [39], Bi, Nb [129], Li [135, 144] and Sb [29, 40, 79, 129, 130].

Especially the last dopant mentioned, Sb, enhances the conductivity as a group V element significantly by introducing electrons into the n-type conducting material.

Palladium as Model System for Catalysis

The interconversion of gas-molecules with single crystal palladium surfaces have been studied extensively. The oxidation process of CO to CO_2 , the adsorption properties of CO_2 , but also CO-induced reconstructions are of particular interest [14, 55, 63, 65, 76, 90, 91, 93, 94, 104, 122, 168, 190]. Other gases like NO [66, 76], H_2 [61, 101, 112, 133, 170] or O_2 [114, 185, 186] were studied as well.

Studies that are dealing with Pd-particles on metal oxide supports are of particular importance

since such a model system would be closer to the situation of Pd-doped SnO₂. Studying on such a system regarding its adsorption properties in comparison to single crystal surfaces, could show that adsorption on clustered surfaces shows similarities to step, corner or defect adsorption on single crystal surfaces [173]. Such nanometer sized cluster show a reversible change in their shape under oxidizing and reducing conditions at temperatures around 550°C [62]. The clusters were characterized ex-situ by HRTEM. But also in-situ characterization with identifying the terminations of the side faces by atomically resolved STM has been performed [67]. In Ref. [19] a model for the oxidation process of Pd-clusters based upon a molecular modelling approach and experimental results are given.

Pd on SnO₂(110)

Nevertheless, the situation on Pd doped SnO₂ has to be treated in a different manner since it must be assumed that Pd is almost completely converted to an oxide under common sensor fabrication conditions (sintering at high temperatures in air). Additionally, a diffusion of oxidized Pd into the SnO₂ matrix may happen at sintering temperatures up to 1000°C. Evaporating Pd on well-defined SnO₂(110) surfaces offers the opportunity to study this process from pure metal clusters to a possible diffusion into the bulk.

In a recent study on time-dependent conductance of Pd-dosed SnO₂ [17], plasma and thermally oxidized SnO₂(110) surfaces were compared to each other showing significant differences in the behavior between the thermally oxidized and plasma oxidized surface (the latter one is more oxygen-rich). This behavior was correlated to charged chemisorbed oxygen reacting with the Pd. While a sufficient amount of chemisorbed oxygen was available for all investigated coverages in the case of the plasma-oxidized surface, the thermally oxidized surface showed similar behavior only up to 1 ML palladium and the difference in behavior at higher coverages was explained by reaction of Pd with surface oxygen and by it a reduction of the surface.

These findings are consistent with earlier measurements by Geiger et al. [48, 49] where – on less oxygen-rich surfaces – Pd was oxidized by O₂-treatment with temperatures at or above 670 K. For lower temperatures, only metallic Pd was found (measured by XPS). In another study

oxidized Pd^{2+} -species were only observed for low coverages on the oxygen-treated $\text{SnO}_2(110)$, which is consistent with the results of Cavicchi et al. [17] summarized above. The conductance behavior first showed a significant change at > 0.5 ML as well.

Summarized one can say that for the formation of PdO on $\text{SnO}_2(110)$, reactive oxygen species must be available either as chemisorbed oxygen or in the gas phase at sufficiently high temperature.

Other Metals deposited onto SnO_2

Sn on $\text{SnO}_2(110)$ A comparative study on Sn interaction with thermally and plasma oxidized surfaces show similar behavior with a XPS-shoulder of metallic tin at the Sn_{3d} -Peaks occurring with increasing Sn-coverage. This effect could be observed for the thermally oxidized surface at lower Sn-coverages, which was explained by the chemisorbed reactive oxygen on the plasma-oxidized one [16].

An earlier study showed consistent results with the metallic tin peak arising at about 0.5 ML [41]. In this study the tendency is the same for reduced and stoichiometric surfaces (metallic tin is detectable at slightly higher coverages in the case of the stoichiometric surface).

Cu on $\text{SnO}_2(110)$ SRPES data of Cu-deposition on $\text{SnO}_2(110)$ show metallic tin diffusing through the copper layer. Tin was even visible in the spectra at high coverages of copper. Subsequent oxidation transfers both metals into an oxide [103].

2.2.4 Adsorbate Systems

CO on $\text{SnO}_2(110)$

Carbon monoxide and its oxidation to CO_2 has been and still is a model reaction in UHV studies on many surfaces and is, as a toxic gas, of significant importance in gas sensing applications. SnO_2 gas sensors early proved to be highly sensitive to this reducing gas with detection limits down to the low ppm-range. Therefore a clarification of the CO/ SnO_2 interaction is of particular interest.

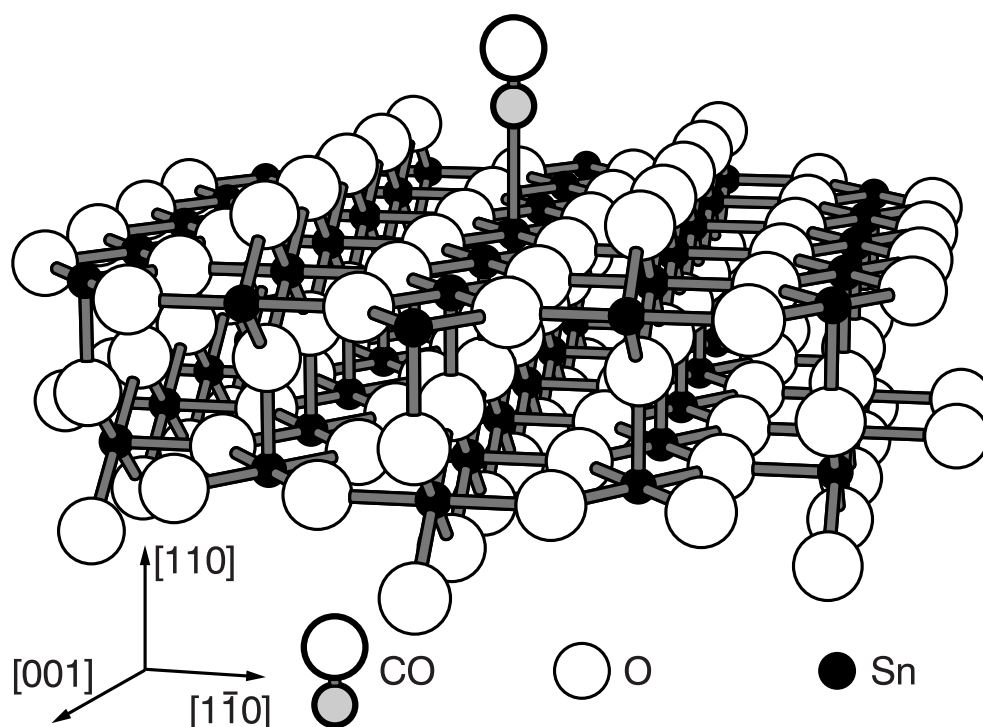


Figure 2.7: SnO₂(110) with adsorbed CO-molecule. The adsorbate position was optimized by using a relatively small Sn₃O₇ cluster (see Ref. [124]).

In spite of this, only few experimental and theoretical studies deal with CO interaction on SnO₂(110) surfaces. In the following, one theoretical study and one experimental study are summarized.

Ab initio theoretical Approach In the calculations of Ref. [124] only the stoichiometric SnO₂ surface with CO and O₂ adsorbed on the five-fold coordinated Sn sites is treated. While this is a restriction for comparing with UHV measurements on the S&A (sputter and annealed) surface, it is convenient for comparing these calculations with ambient air measurements, where the SnO₂ can be assumed to be stoichiometric with the (110) surface as the predominant termination. Figure 2.7 shows the position of the CO molecule on top of the SnO₂(110)-surface which has been optimized by using a Sn₃O₇ + CO cluster while simultaneously minimizing the total energy. The final calculation of the band structure was performed on a much larger – Sn₃₂O₇₁ – cluster.

The calculation on a finite cluster is well suited for studying localized phenomena like chemisorp-

tion, but leads to energy levels in the band gap originating from 'edge atoms' of the cluster. Nevertheless, when taking only states into account that are not related to 'edge atoms', the valence band and conduction band position, with a band gap of 3.6 eV, could quite well be reproduced.

The most interesting energy levels induced by the adsorbates O₂ and CO are 1.2 eV and 0.9 eV below the conduction band minimum respectively. Both adsorbates lead to a band bending by increasing the conduction band edge by 0.3 eV.

Experimental Data In Ref. [165], the conductance response on H₂, O₂ and CO of single crystal SnO₂ thin films doped with Pd were investigated. For CO adsorption only a little conductance increase was observed. In fact, only the samples with the lowest initial conductivity showed a significant effect.

Therefore – in contrast to the interaction with H₂ and O₂ – no model was proposed, but it was assumed that the surface oxygen should play an important role because of the observation that the samples with highest resistivity (most oxidized) showed the biggest effect.

It should be mentioned here, that the palladium coverage was quite high with the SnO₂ surface almost completely covered with Pd-clusters. Therefore, the observed behavior has to be treated carefully when comparing these results to Pd/SnO₂ gas sensors with a relative Pd amount typically below one percent.

H₂O on SnO₂(110)

The interaction of water with the SnO₂(110) surface was studied in a number of publications by the method of choice – TPD – and also by surface sensitive spectroscopy like UPS, AES, and XPS [28, 51, 68, 143, 189]. But additionally there is one theoretical study dealing with different adsorption geometries of H₂O on the stoichiometric SnO₂(110)-surface [57].

First-Principles Calculations on possible Adsorption Geometries Table 2.4 shows three different configurations of adsorbed water. The energetically most favorable geometry is the unsymmetrical dissociative adsorption shown in table 2.4 b), where the OH-groups are placed onto the

five-fold coordinated tin and on the positions of bridging oxygens with a hydrogen bond of 1.81 Å between them.

The calculations were done by an improved LDA (local density approximation), using 'generalized gradient approximations' (GGA). For the calculations, an infinite periodic 'slab' geometry with a cube-size of $R = 7-13$ Å depending on the calculated adsorbate was used.

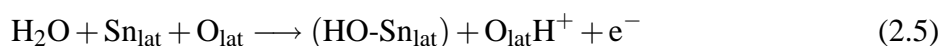
Experimental Results TPD spectra of adsorbed water on SnO₂(110) show three temperature regimes at 200, 300 and 435 K [51]. The first two features are attributed to molecularly adsorbed water and the desorption at the highest temperature to dissociative adsorption of water and recombination after desorption (concluded from UPS difference spectra).

Three different types of surface composition were investigated. The stoichiometric, the reduced (after heating at 950 K) and a defective surface (S&A, 1000 K). The defective surface showed the least adsorption of molecular water, but in the case of all surfaces TPD features at similar temperatures could be observed. Dissociative adsorption seemed to be favored on the defective surface, leading to up to 35% dissociative adsorption in comparison to about 15% on the stoichiometric surface.

Earlier studies by AES, UPS and TPD [24, 143] are consistent with the results summarized above, but are less detailed according to the TPD data.

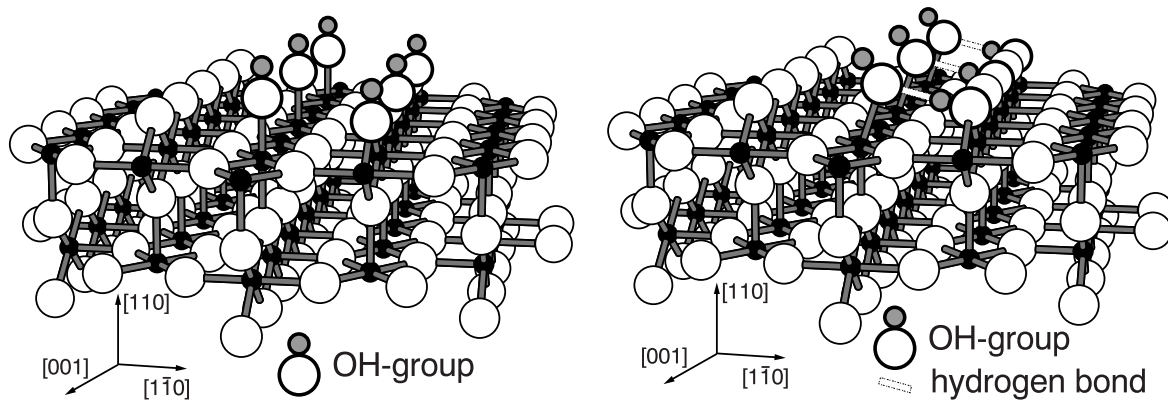
There were also two TPD studies on sintered pellets published [68, 189]. In these experiments (adsorption at room temperature) two TPD features at around 400 K and 700 K were observed which means that it occurred at much higher temperatures than was expected from the TPD-data on SnO₂(110).

The following reactions were postulated for the dissociative interaction of water with SnO₂ [68]:

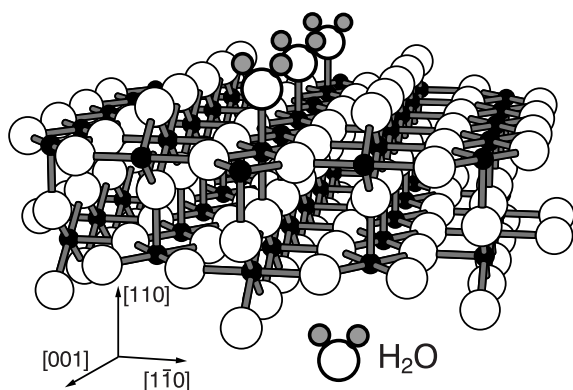


This reaction would be consistent with the adsorption geometries in table 2.4 a) and b). But it might also be possible that the OH-groups are preferably bound to the five-fold coordinated Sn-sites:





- a) $\text{SnO}_2(110)$ with adsorbed OH-molecules and H-atoms. b) $\text{SnO}_2(110)$ with adsorbed OH-molecules, H-atoms and hydrogen bonds between the OH-groups.



- c) $\text{SnO}_2(110)$ with molecularly adsorbed H_2O -molecules.

Table 2.4: Possible adsorption geometries of water on stoichiometric $\text{SnO}_2(110)$ [57].

Hydrocarbons on $\text{SnO}_2(110)$

For a more detailed understanding of the chemical activity of single crystalline SnO_2 surfaces, the interaction of well-defined tin dioxide surfaces with more complex molecules like methane, methanol, formic and acetic acid is important. By experimental as well as by theoretical approaches such systems were studied in the past.

On the one hand, it is of interest to study the geometrical conformation of adsorbed molecules in order to get an idea about possible reaction mechanisms and reactive sites on the surface. Such results are available as theoretical calculations for methane [187], methanol [12] and ethanol [1] which are either interacting with the reduced or with the stoichiometric $\text{SnO}_2(110)$ surface.

On the other hand, it is of great interest to study the reaction products after a heterogeneous catalytic reaction on the SnO_2 surface. This for example can be done by adsorbing high doses of gas at low temperature and then recording TPD spectra of possible reaction products. Under such conditions ethanol decomposes on $\text{SnO}_2(110)$ to ethylene, water, and acetaldehyde [82] and methanol to formaldehyde and water [52].

More detailed studies on the interconversion of formic acid with $\text{SnO}_2(110)$ on differently prepared surfaces show a significant dependency of the experimental results on the initial surface preparation [50, 81] and point out the need for a well-defined and well-prepared model system.

The various reaction products of acetic acid were also determined by TPD after adsorption at room-temperature [162]. By reactive scattering of acetic acid with the tin dioxide surface, the dynamical reaction of this gas was monitored by dosing the gas in periodic cycles [95].

2.3 Polycrystalline SnO_2

Gas sensors based upon doped and undoped SnO_2 material consist of a transducer, for example an interdigitated electrode, and a semiconducting tin dioxide layer. Such layers may be produced by PVD [137], CVD [11], reactive sputtering [30, 145], laser evaporation [99, 171] or sol-gel techniques [70, 87, 164]. Comparisons between sensors based upon different fabrication processes can be found in the literature [138, 139].

In the present study, photoelectron spectroscopy was applied to reveal information about the valence band structure of SnO₂ materials. This is the reason for summarizing photoemission studies on polycrystalline SnO₂ surfaces in the following.

2.3.1 XPS Studies

An investigation of the chemical state of surface tin is complicated by almost negligible Sn 3*d* core-level shifts between Sn²⁺ and Sn⁴⁺ on tin dioxide surfaces. Only little shifts around 0.1 eV were reported which result mainly in some peak broadening and also may be correlated to band bending effects [20, 37, 77, 118]. Only metallic tin can easily be distinguished by a core-level shift in the Sn 3*d* region of about 1.9 eV towards lower binding energy [38].

On the contrary, there are significant core-level shifts reported on SnO surfaces which are – under ambient air conditions – covered by a tin dioxide layer. Sn 3*d*_{5/2} core-levels were recorded by varying the sputtering time and fitting the Sn 3*d*_{5/2} peak to three different contributions to the photoemission signal. In this way, a peak-shift between Sn²⁺ and Sn⁴⁺ of 0.73 eV and between Sn⁰ and Sn⁴⁺ of 2.5 eV could be revealed [158].

Since the situation in core-level spectroscopy of SnO and SnO₂ is quite complicated and controversially discussed, main emphasis was put on studying the valence band by XPS. Despite the low intensities of the valence band at X-ray photon energies, there is the advantage of relatively high tin subshell photoionization cross sections when compared to the corresponding oxygen cross sections (see table 3.2). This is especially useful when investigating tin-derived structures in the valence band region. A discrimination between SnO and SnO₂ can easily be done by this approach and corresponds very well to theoretical predictions [96, 100, 113, 134, 148, 188].

2.3.2 Synchrotron Radiation Studies

Synchrotron radiation sources offer tunable light sources with which it is possible to take advantage from resonance and/or cross-section effects. By resonant photoemission in a photon energy range of 22-50 eV, the Sn 5*s* origin of the band gap states could be supported for reduced single crystal surfaces (see Ref. [160] and section 3.1.1). Two other studies were dealing with the

examination of the O 2*s* core-level which is situated at little lower binding energy than the very strong Sn 4*d* core-levels (see figure 8.1). By adjusting the photon energy to the Cooper minimum of the Sn 4*d* cross-section, the intensities of the O 2*s* and the Sn 4*d* core-levels can be adjusted so that the O 2*s* level becomes accessible for curve fitting and further data evaluation [116, 159].

2.3.3 Electronic Structure of Stannous Oxide

In a recent resonant photoemission study on SnO, the valence band contributions due to Sn 5*s*, Sn 5*p* and O 2*p* levels were investigated and correlated to calculated DOS curves [86]. For interpreting photoemission results of reduced SnO₂ surfaces, such information is of particular interest. Especially the nature of band gap states often observed on doped SnO₂ surfaces may be related to SnO by comparing them with these measurements (compare section 8.1.2 and figure 8.7).

Chapter 3

Measurement Techniques

3.1 Chemical Composition of a Surface

In the following, surface analytical techniques that were used to determine the chemical composition or electronic structure of a surface are described. Mainly photoelectron spectroscopy was applied in this study, since it combines high sensitivity, chemical information and comparatively easy interpretation of the spectra. Auger Electron Spectroscopy (AES) was only used for preparation control and Secondary Ion Mass Spectroscopy (SIMS) for trace element analysis of the sensor's impurities with limits of detection down to ppm concentrations.

3.1.1 Photoelectron Spectroscopy (XPS / UPS / SRPES)

The analysis of photoelectrons emitted from a surface provides not only information about the chemical composition of the surface, but also about the chemical state of the elements present. It also offers the possibility to record spectra of the valence band region (XPS valence band spectroscopy, UPS), giving insight in the density of filled states at and near the surface, reflecting the electrical and chemical properties of a material.

In general the abbreviation 'UPS' is used for photoelectron spectroscopy at photon energies below 100 eV. Above 100 eV the abbreviation 'XPS' or 'ESCA' is common. In the case of laboratory sources, He I and He II radiation at 21.22 eV and 40.81 eV is used for UPS and the Al-

	He I	He II	Mg K_{α}	Al K_{α}
photon energy [eV]	21.22	40.81	1253.6	1486.6
line width [eV]	0.03	0.03	0.7	0.85
satellite lines	23.09 eV ($\approx 2\%$)	48.37 eV (< 1%)	1262 eV (9.2%)	1496.2 eV (7.8%)
	23.74 eV ($\approx 0.5\%$)	51.02 eV (< 1%)	1263.6 eV (5.1%)	1498.1 eV (3.3%)

Table 3.1: Laboratory light sources.

K_{α} and Mg- K_{α} characteristic X-ray lines for XPS ($h\nu = 1253.6$ eV and 1486.6 eV respectively). Since the photoemission process is well understood (see figure 3.1) and sensitivity factors are available, a quantitative analysis of the elements is easily accessible in the XPS photon energy range. These common light sources for laboratory XPS and UPS are summarized in table 3.1 together with their natural line widths and satellite lines.

In the following text, effects which can influence the shape of a spectrum are discussed. These effects are due to different photon energies used for photoelectron excitation. On the one hand, this may have a direct effect on the photoionization process, i.e. the photoionization cross section, or on the other hand on the kinetic energy of excited electrons.

Resonance effects can appear when the photon energy crosses the threshold of an electronic transition or when quantummechanical effects appear. An example is the momentum and symmetry conservation during photoexcitation: Whereas the symmetry conservation is independent of photon energy, the momentum conservation is not [43].

Principle of Photoelectron Spectroscopy

When a photon interacts with a surface, a variety of effects may appear. One of them, the photo effect, leads to the emission of electrons with a well-defined energy (see figure 3.1). This kinetic energy is related to the photon energy and the former energetic level of this emitted electron in the atom. The relation $E_{\text{kin}} = h\nu - E_B$ is valid when the difference between the energy of the

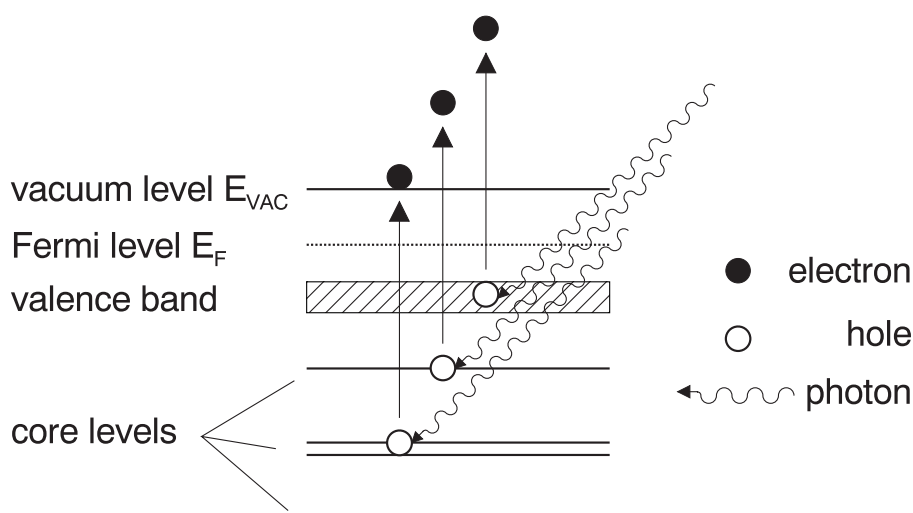


Figure 3.1: Scheme of the photoionization process.

initial state and the final state of the system is negligible ($E_i \approx E_f$) and indeed, this relation holds in a good approximation in most cases.

Figure 3.2 shows a typical survey spectrum of a $\text{SnO}_2(110)$ single crystal with some spectral contribution of the platinum holder. One can see that the spectrum is dominated by the core-level peaks of tin and oxygen. But also Auger electrons contribute to such a spectrum (see section 3.1.2). The typical stepped shape is due to inelastic scattering of emitted photoelectrons and leads to a tail to lower binding energies at every photoelectron peak. The features labeled 'satellites' and 'ghosts' result from the non-monochromatic X-ray source. Satellite peaks are excited by $\text{Mg-K}\alpha_{3,4}$ X-ray lines (see table 3.1) and the ghost peaks originate from $\text{Al-K}\alpha$ radiation which is generated by electrons from hitting either the thin aluminium window between sample and anode or the Al anode of the twin-anode X-ray source. On the one hand, the window in front of the anode is necessary to prevent electrons hitting the sample or getting into the analyzer and on the other hand, reduces the bremsstrahlung background.

More information about spectral interpretation and practical application of ESCA can be found for example in Ref. [9].

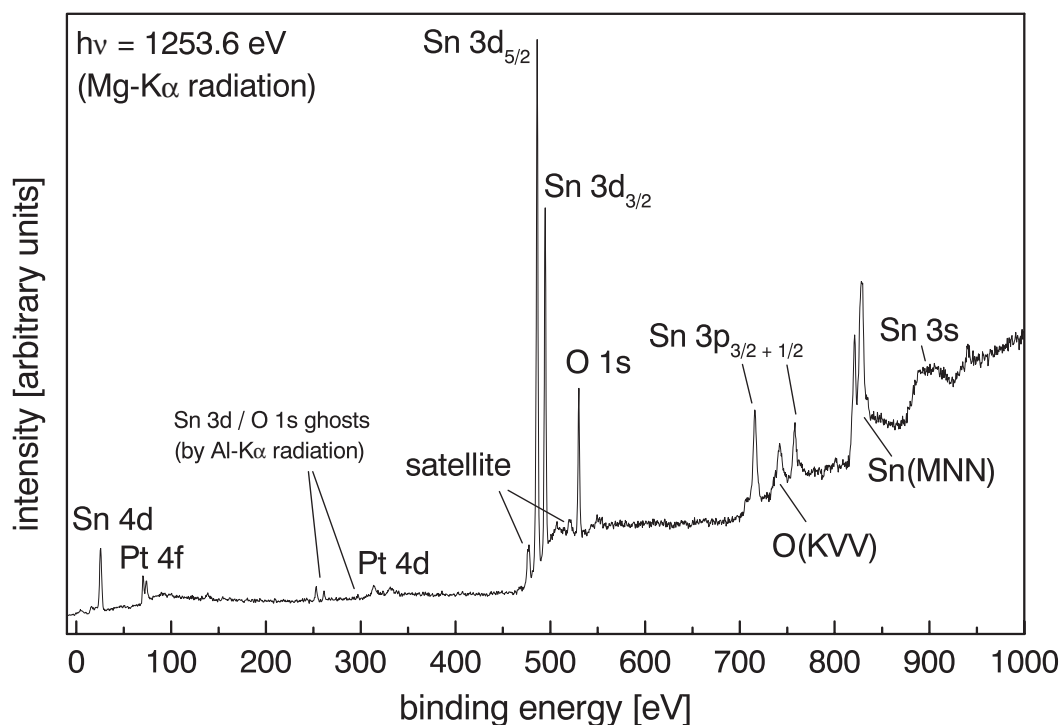


Figure 3.2: Typical XPS survey spectrum of $\text{SnO}_2(110)$ with some platinum signal from the sample holder. Most prominent photoelectron and Auger peaks are labeled. Satellites due to $K\alpha_3$ and $K\alpha_4$ radiation are marked at the Sn $3d$ and O $1s$ core-levels.

Mean free Path of Electrons

A comprehensive compilation of experimental data of the Inelastic Mean Free Path (IMFP) of electrons in elements, adsorbed gases, organic and inorganic compounds is provided by Seah and Dench [142]. When looking at figure 3.3 one can easily see that the information depth of photoelectron spectroscopy with laboratory sources can differ up to almost one order of magnitude. This can lead to differences in photoemission spectra when the bulk stoichiometry is different from the stoichiometry of the surface, or when surface states appear in the valence band spectra. Valence band electrons emitted by a Mg or Al X-ray source would have an IMFP of around 2 nm which means only little surface contribution has to be expected for such a spectrum. In contrast, valence band electrons excited by UV-light lead to a very surface sensitive measurement due to their IMFP of 0.4 to 0.6 nm.

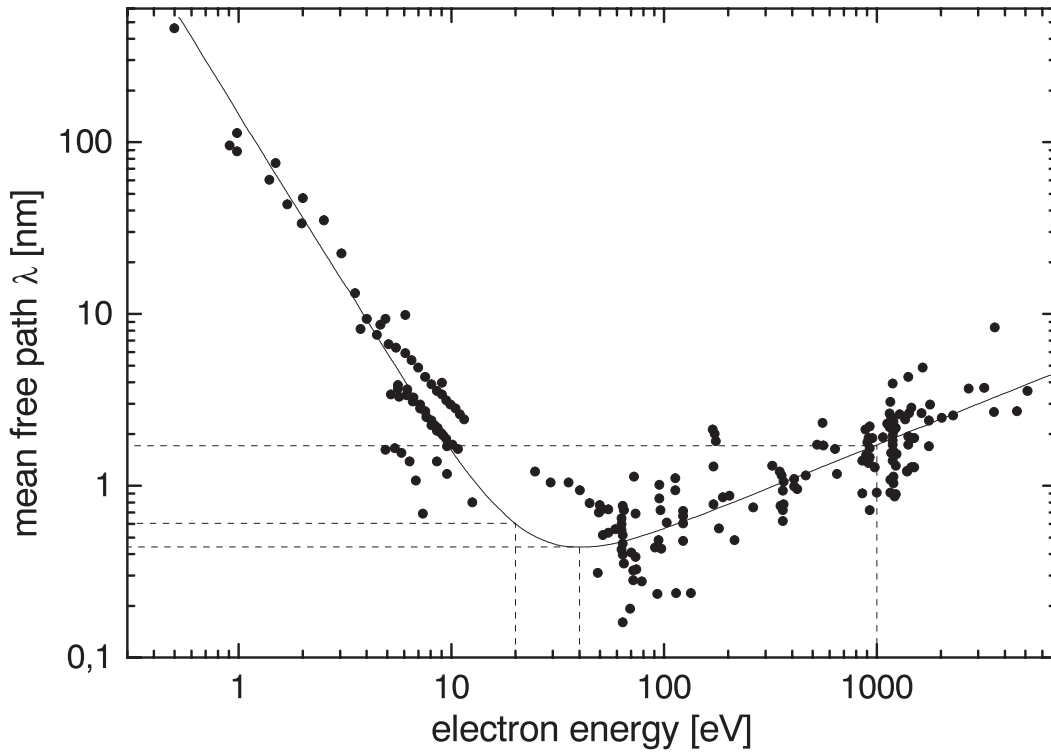


Figure 3.3: Mean free path of electrons in metals and compounds as a function of their energy. See Ref. [43, 142, 175] for details and Ref. [121] for a theoretical treatment. Mean free paths λ for $h\nu = 20$ eV, 40 eV and 1000 eV are marked by dashed lines.

One way to overcome this problem is to vary the angle φ between sample and analyzer, since the distance an electron has to travel through the sample is dependent on this angle:

$$\lambda = \sin \varphi \cdot \lambda_{90^\circ}$$

with λ as the IMFP at angle φ between sample and analyzer and λ_{90° the IMFP at $\varphi = 90^\circ$.

This method also offers the opportunity to record non-destructive depth-profiles of a sample, but the extraction of the depth distribution of each element from such data is a non-trivial problem and will not be treated further here (see for example Ref. [169]).

Photoionization Cross-Sections

The photoionization cross sections are highly dependent on the photon energy used for excitation. In Ref. [141], cross sections for all elements with respect to Mg- and Al- K_α -sources were

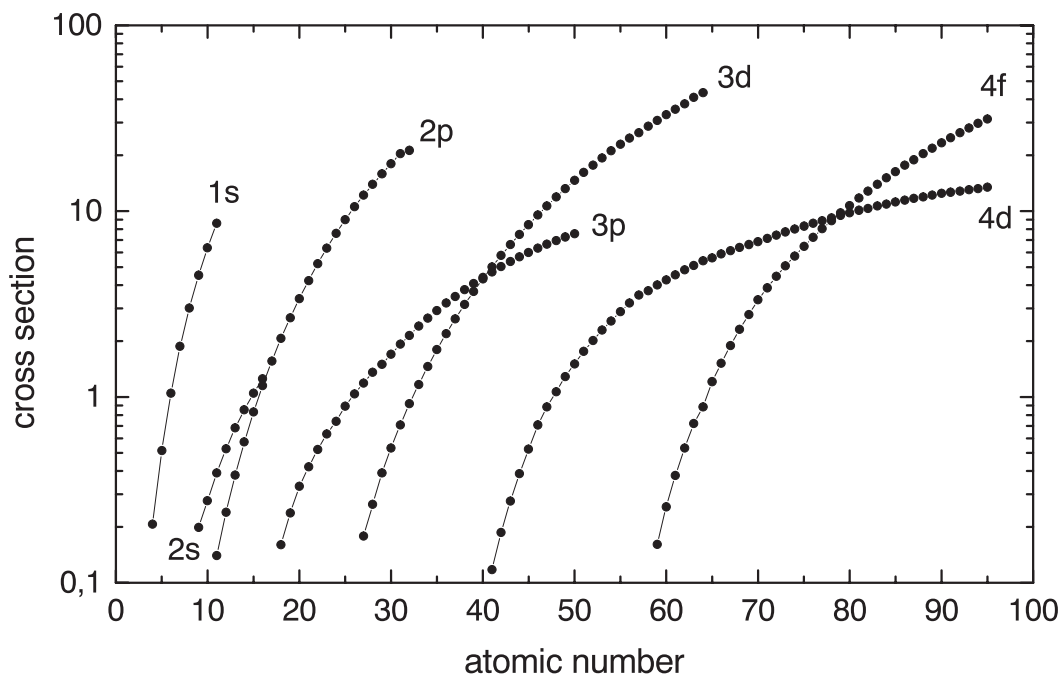


Figure 3.4: Photoionization cross sections of Mg-K α (1253.6 eV) X-ray-sources [141]. Cross sections are referenced to $\sigma_{C1s} = 1.000$. p , d and f cross sections refer to the 3/2, 5/2 and 7/2 level respectively. See Ref. [43] for a similar diagram of Al-K α cross sections.

calculated. Values are normalized to the cross section of the C1s core level ($\sigma_{C1s} = 1.000$). Figure 3.4 shows the cross sections at 1253.6 eV photon energy of the elements as a function of their atomic number. The photoionization cross sections are varying more than two orders of magnitude and therefore have to be seriously taken into account when interpreting a spectrum. These values were obtained by using a single atom approximation. Nevertheless, this approximation often holds even for valence band spectra. There are for example numerous XPS valence-band studies existing where spectra were taken from SnO₂ samples [97, 100, 148, 158]. In the latest publication experimental (XPS) and theoretical data (X α cluster calculations) were compared to each other by taking these cross-sections into account. This normalization to the XPS cross section results in a very good agreement of XPS valence-band spectra and theoretical calculations.

But the photoionization cross section is not constant for the subshells of an element when changing the photon energy. Synchrotron radiation offers the opportunity to adjust the photon

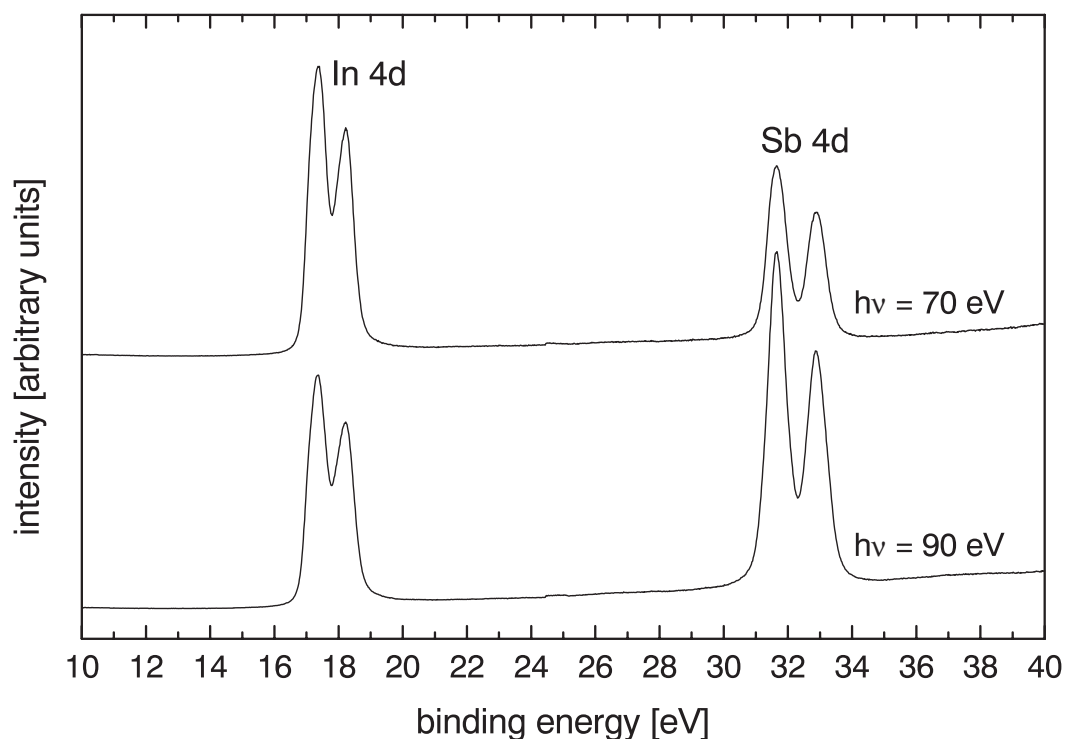


Figure 3.5: InSb measured at two different photon energies. The difference in the photoionization cross sections at $h\nu = 70 \text{ eV}$ and 90 eV of these two elements leads to an inversion of the intensity ratio.

energy, with its continuous light, for example to the highest cross section of a certain orbital to increase sensitivity. This variation in cross section can also be used to distinguish contributions from different elements to the valence band by taking Energy Distribution Curves (EDC) by varying the photon energy or directly Constant Initial State (CIS) spectra by simultaneously changing photon energy and detected kinetic energy of the electrons (i.e. keeping the detected binding energy of electrons constant).

Figure 3.5 for example shows the effect of changing the photon energy from 70 eV to 90 eV on the $4d$ core-levels of InSb. This small change in photon energy leads to an inversion of the intensity ratio of these two elements. Such effects are indeed very strong on SnO_2 . For this reason the photoionization cross sections of oxygen and tin are plotted over a photon energy range of $0\text{-}1500 \text{ eV}$ in figure 3.6 and in table 3.2 the interesting cross section ratios of valence band orbitals

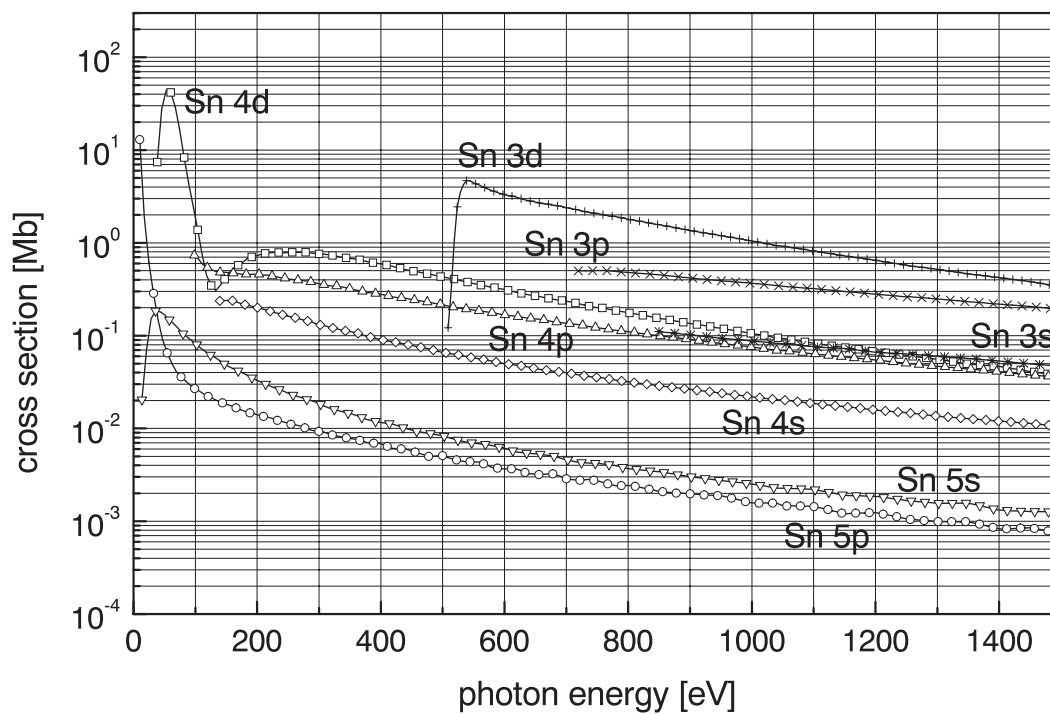
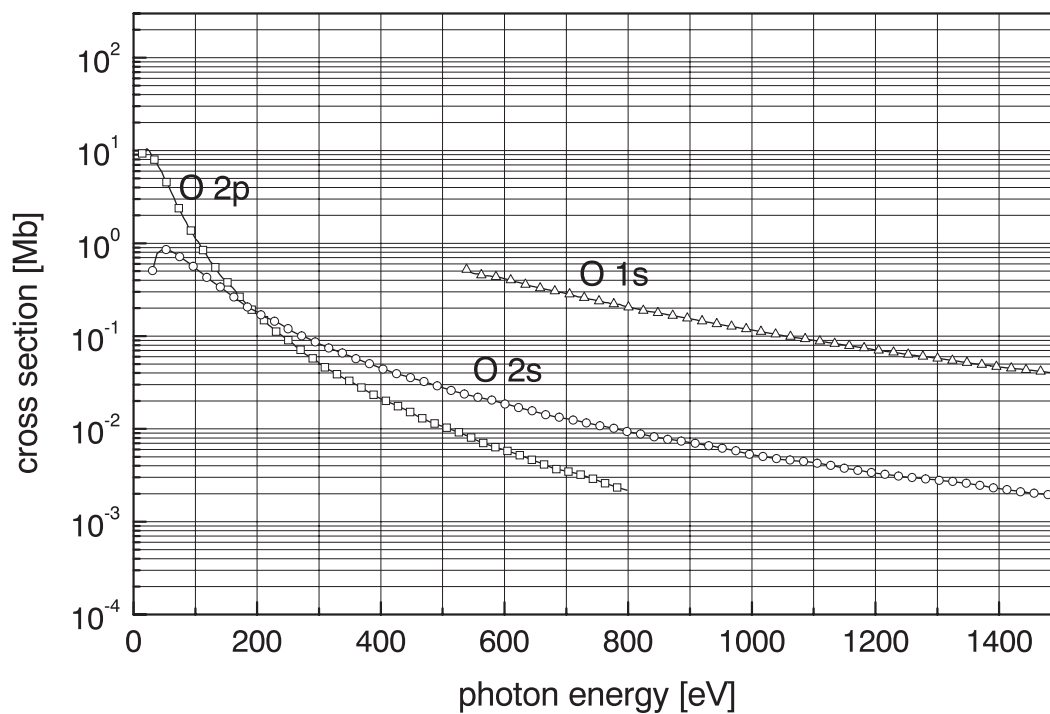


Figure 3.6: Scheme of oxygen and tin photoionization cross sections. Yeh and Lindau [191] calculated the subshell photoionization cross sections for all elements with $1 \leq Z \leq 103$.

are calculated for the UPS and XPS photon energy range. Even between the behavior of the two tin orbitals there is a significant difference.

ratio	photon energy [eV]					
	21.22	40.81	200	600	1253.6	1487
Sn 5s / O 2p	$6.1 \cdot 10^{-3}$	$2.7 \cdot 10^{-2}$	0.17	1.0	3.2	5.0
Sn 5p / O 2p	0.11	$2.1 \cdot 10^{-2}$	$7.6 \cdot 10^{-2}$	0.61	2.0	3.2

Table 3.2: Ratio of Sn 5s and 5p photoionization cross sections with respect to the cross section of the O 2p orbital [191].

Effects of Photon Momentum

Considering initial states (i) and final states (f), momentum conservation has to be fulfilled upon photoexcitation:

$$E_f(\mathbf{k}_f) - E_i(\mathbf{k}_i) = h\nu \quad (3.1)$$

and

$$\mathbf{k}_f - \mathbf{k}_i = \mathbf{k}_{h\nu}$$

For $h\nu < 100$ eV, $\mathbf{k}_{h\nu}$ can be neglected. That means due to momentum conservation only direct (or vertical) transitions are allowed. A more detailed quantum mechanical treatment using *Fermi's Golden Rule* under introducing a periodic potential leads to the following expression (see for example [43] or [120]):

$$\mathbf{k}_f = \mathbf{k}_i + \mathbf{G}_B \quad (3.2)$$

\mathbf{k}_i and \mathbf{k}_f are the momentum or wavevector of the electron in the initial and final state, $\mathbf{k}_{h\nu}$ is the momentum of the photon and \mathbf{G}_B a reciprocal lattice vector of the bulk. The latter expression can further be simplified by incorporating the \mathbf{G}_B symmetry, as in a periodic potential all points that can be connected with a vector of the reciprocal lattice are equivalent. Such a representation is called the reduced zone-scheme and in such a diagram only vertical transitions, i.e. $\mathbf{k}_f = \mathbf{k}_i$, are allowed.

The effect of momentum conservation on photoelectron spectra can be best observed when collecting the photoelectrons angularly resolved. In angle-integrated spectra the photoelectrons are collected over a broad range of \mathbf{k} vectors and only at very low photon energies (≤ 10 eV) an effect can be observed [175]. On the other hand it is possible to select only a small angle of photoelectrons leaving the sample. This so-called Angle Resolved UPS (ARUPS) gained wide attention in investigating the band structure of surfaces (see for example Ref. [43] and [175]).

Resonance Effects due to Electronic Transitions (Fano-type Resonance)

In 1961, Fano developed a theory to describe the configuration interaction of a discrete state with a continuum [44] due to photoabsorption. The main emphasis of his calculation was to explain the typical line shapes of rare gas photoabsorption spectra. But actually, this work gained wide attention for interpreting resonant photoemission spectra. Johansson et al. [88] could reproduce the typical Fano line shape in a very good approximation on oxidized Yb surfaces. By oxidizing a metallic Yb surface, the resonance was turned on by changing the electronic configuration of Yb from $4f^{14}$ to $4f^{13}$ by oxidation. The emptied electronic level now enables the resonance and the typical Fano line shape can be reproduced by calculating the ratio between CIS curves taken at the resonant binding energy of clean (without resonance) and oxidized (resonating) Yb.

A summary of Fano's study from the experimentalist's point of view is given in Ref. [2]. Since the emphasis of the original work was on photoabsorption and not on photoemission, the theory was extended to the influence on photoelectron spectra by Yafet [183, 184]. Of course, the interaction of only one discrete state with only one continuum is a crude approximation for most resonances observed in experiment. Therefore, Davis and Feldkamp extended Fano's theory to the interaction of many discrete states with many continua [31, 32].

Despite its restrictions and the extensions by other authors, the typical line shape, based upon the simplified model of Fano, has often been observed in a more or less good approximation and for this reason is outlined in the following.

Fano-type Resonance Let us consider an atom with ground state Φ_G . When absorbing a photon of suitable energy, there is a certain transition probability to the unperturbed continuum of

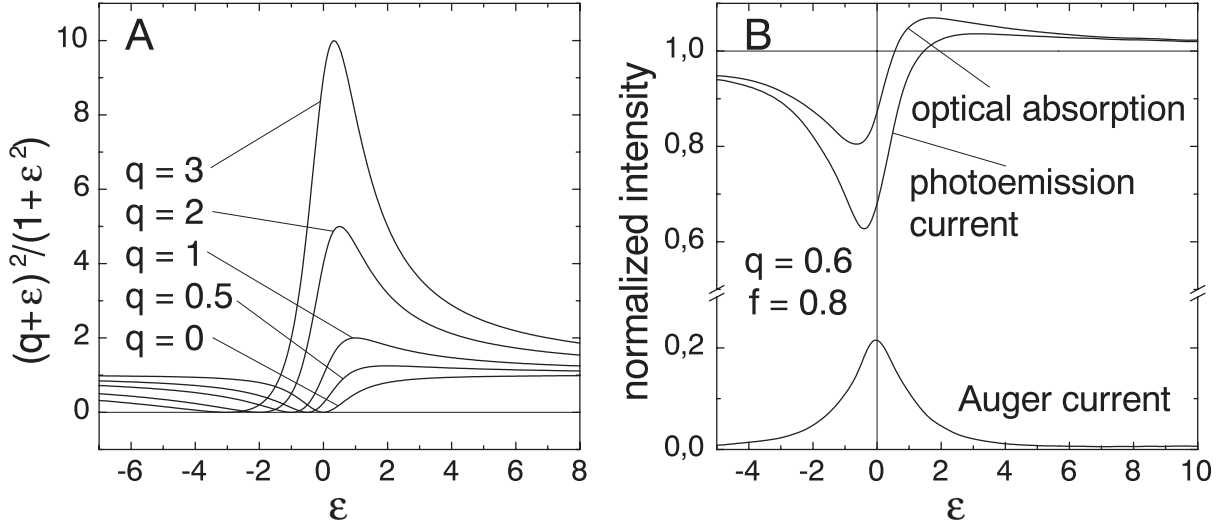


Figure 3.7: Curve profiles for different line shape factors q of Fano resonance curves are shown in figure A [44]. Figure B denotes optical absorption, photoemission and Auger currents calculated by Yafet [183] for a system with an additional electronic state added to the Fano system. This additional state enables relaxation of the system by emitting an Auger electron.

states $\psi_{E'}$ which is in the case of photoemission experiments determined by the kinetic energy of the emitted electrons. By adding an additional state ϕ to this system, 'configuration interaction' may occur giving rise to the characteristic Fano line-shape. This state ϕ is in resonant photoemission the intermediate state with a core-hole excited in the first step of the process.

When starting from a system consisting of one sharp state ϕ with energy E_ϕ and a continuum of states $\psi_{E'}$ with energy E' , the exact eigenfunctions Ψ_E can be written as a linear superposition of these states:

$$\Psi_E = a_E \phi + \int dE' b_{EE'} \psi_{E'} \quad (3.3)$$

An explicit calculation of the coefficients a_E and $b_{EE'}$ is given by Fano [44].

The transition probability from the initial ground state Φ_G to Ψ_E can be described by the matrix element:

$$\langle \Psi_E | T | \Phi_G \rangle = a_E^* \langle \phi | T | \Phi_G \rangle + \int dE' b_{EE'}^* \langle \psi_{E'} | T | \Phi_G \rangle \quad (3.4)$$

By calculating the ratio between the transition probability $|\langle \Psi_E | T | \Phi_G \rangle|^2$ and the transition probability to the unperturbed continuum $|\langle \psi_{E'} | T | \Phi_G \rangle|^2$ (i.e. without the additional discrete state

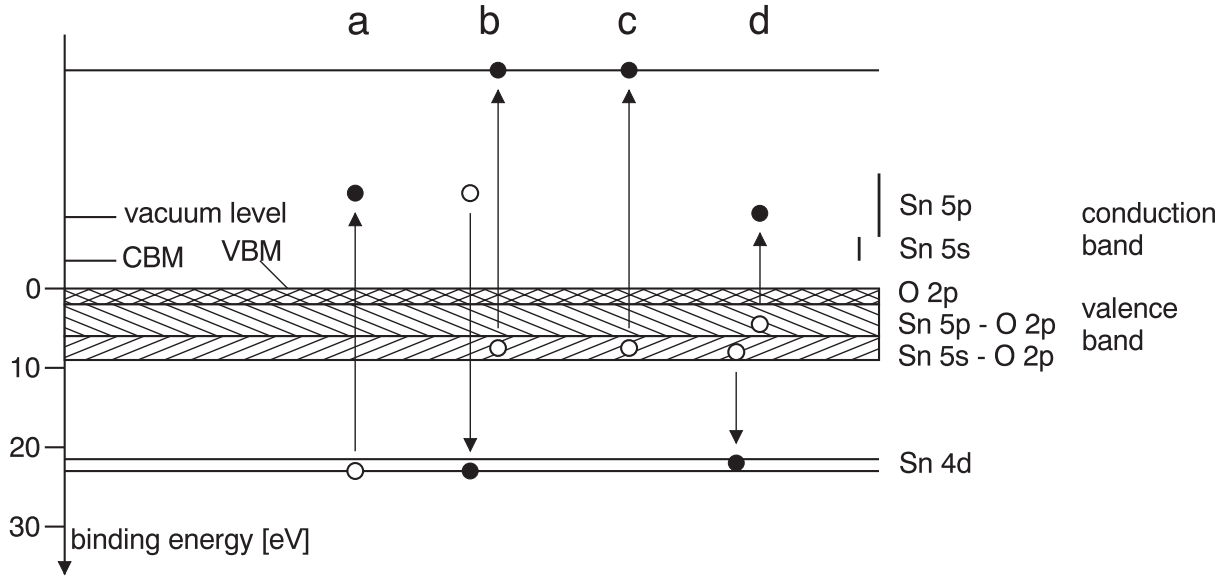


Figure 3.8: Scheme for explaining the resonance effect at $h\nu = 35$ eV on sputtered SnO₂(110) [160]. The binding energies are referenced to the valence band maximum of SnO₂ in contrast to the valence band spectra in chapter 8 which are referenced to the Fermi level. Letter 'a' marks absorption by the dipole-allowed transition Sn 4d \rightarrow 5p, 'b' subsequent recombination by ejecting – for example – a 5s electron. 'c' is direct photoemission (resulting in an electron with the same kinetic energy as in case 'b') and 'd' describes recombination by Auger decay.

ϕ), the expression for the Fano resonance line shape can be found:

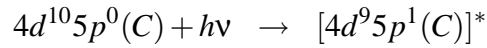
$$f(\epsilon) = \frac{(q + \epsilon)^2}{1 + \epsilon^2} = 1 + \frac{q^2 - 1 + 2q\epsilon}{1 + \epsilon^2} \quad (3.5)$$

The reduced energy variable ϵ corresponds to the photon energy in photoabsorption or photoemission experiments and q is the line-shape parameter, defined by the system [44]. Figure 3.7 A shows Fano-curves for $q = 0, 0.5, 1, 2, 3$. In the right hand figure, results of Yafet's calculations are shown.

Example: Sputtered SnO₂(110) The resonance at the Sn 4d \rightarrow Sn 5p absorption threshold of sputtered SnO₂(110), observed and discussed by Themlin et al. [160], is shown in figure 3.8. They could observe a resonance at $h\nu = 35$ eV on sputtered SnO₂(110). This effect was explained by an interference of the photoemission process ('c' in figure 3.8) with direct recombination

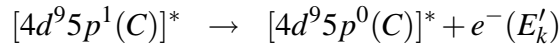
('b') leading to an oscillating photoelectron intensity when sweeping through the Sn $4d \rightarrow$ Sn $5p$ absorption threshold.

Since this interpretation is the starting point for a discussion of the resonant photoemission results presented in section 8.1.2, it will be outlined in the following. Letters C and V denote states in the conduction band and in the valence band, respectively. E_k is the kinetic energy of the electron after emission. Starting with photoabsorption:

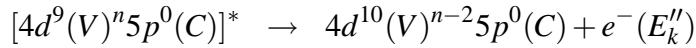


possible decay mechanisms are :

1. Autoionization

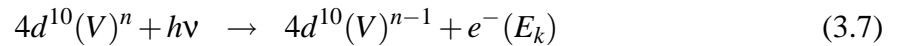
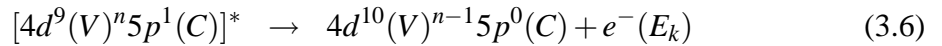


followed by an Auger decay to fill the core-hole ('d' in figure 3.8).



leaving the valence band in a double ionized state.

2. The second non-radiative mechanism, direct recombination (3.6) ('b' in figure 3.8), leads to the same final state and to the same kinetic energy of the emitted electron as direct photoemission (3.7):



The latter two processes, i.e. direct recombination and photoemission interfere, leading to an oscillation in photoelectron intensity when sweeping through the Sn $4d \rightarrow$ Sn $5p$ threshold. By recording valence band spectra in a photon energy range of 22 eV-50 eV and calculating CIS curves of these data, they found that the band gap states of sputtered SnO₂(110) are tin derived. Further considerations of the reduced character of surface tin leads to the tentative conclusion of attributing the band gap states to Sn $5s$ orbitals.

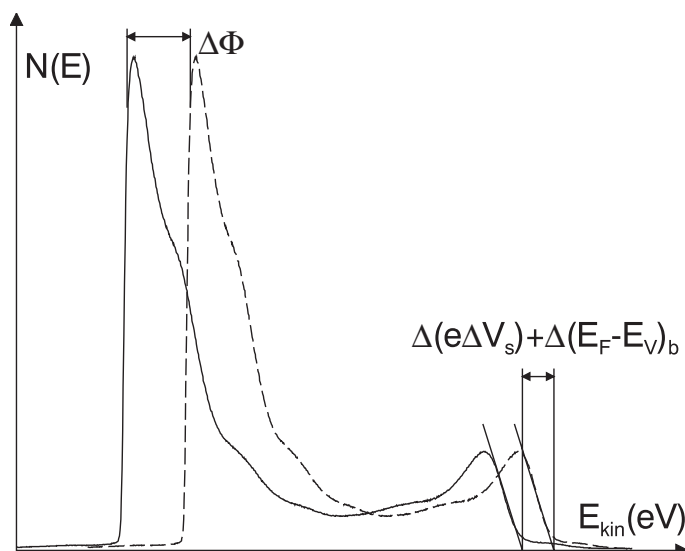


Figure 3.9: Deriving the components of the work function change $\Delta\Phi$ from an UPS spectrum.

Phenomenological Quantities revealed by UPS Spectra

There are various methods with which the work function of a surface compared to another one can be revealed, either directly or indirectly. Direct methods, giving absolute values are for example the onsets of photoemission spectra. That means the first electrons that are capable to overcome the surface barrier. The work function of a surface can be divided into:

$$\Phi = \chi + (E_C - E_F)_b - e\Delta V_s \quad (3.8)$$

with χ as the electron affinity of the surface, $(E_C - E_F)_b$ as the bulk contribution and $e\Delta V_s$ as the surface band bending. Changes in these properties can even occur on adsorbate-free surfaces when changing the surface configuration (for example by sputtering or annealing).

When adsorbing gases on surfaces, only the difference between the work function before and after adsorption often is of interest. Then (3.8) can be written as follows:

$$\Delta\Phi = \Delta\chi + \Delta(E_F - E_V)_b + \Delta(e\Delta V_s) \quad (3.9)$$

How these quantities can be obtained from an UPS-spectrum can be seen in figure 3.9. The overall work function change $\Delta\Phi$ is defined by the shift in the onset of the two spectra. The

bulk and surface band bending can be taken from the shift in the highest occupied state and the electron affinity $\Delta\chi$ simply by subtracting one from another.

3.1.2 Auger Electron Spectroscopy (AES)

This method is based upon the radiationless 'Auger-process' where an electron is emitted with an energy, that is determined by the energy difference of two core levels of an ionized atom and the binding energy of the emitted electron. The energy of an Auger-electron resulting from the ionization of a K-shell and an Auger-process from an L- to a K-shell under emitting an L-electron would be:

$$E_{\text{Auger}}^{KLILII} = E_b^K - E_b^{L_I} - E_b^{L_{II}} \quad (3.10)$$

That means that the kinetic energy of such an electron is independent of the primary energy of an electron beam or of X-ray radiation. This fact can be used – for example – to distinguish the photoelectron signals from Auger electrons by varying the X-ray energy in XPS.

The surface sensitivity of AES is comparable to the surface sensitivity of photoelectron spectroscopy, as the information depth is determined by the escape depth of the excited Auger electrons and not by the range of the primary electrons in the sample.

3.1.3 Instrumentation for Electron Spectroscopy

For discriminating electrons towards their kinetic energy in photoelectron and Auger electron spectroscopy, either electric or magnetic fields are applied. Magnetic fields only work with sufficiently fast electrons and are therefore not suitable to photoelectron spectroscopy of low-energetic electrons (\rightarrow UPS) and are therefore generally not applied. In the field of electrostatic electron energy analyzers two concepts proved to yield optimum performance. On the one hand Hemispherical Analyzers (HMA) mainly applied in photoelectron spectroscopy and on the other hand Cylindrical Mirror Analyzers (CMA) used for Auger electron spectroscopy.

In combination with LEED systems retarding field analyzers (RFA) are also used to record Auger electron spectra. But since an analyzer system of this type has only weak resolving power and little transmission, it is seldomly used in stand-alone AES spectrometers.

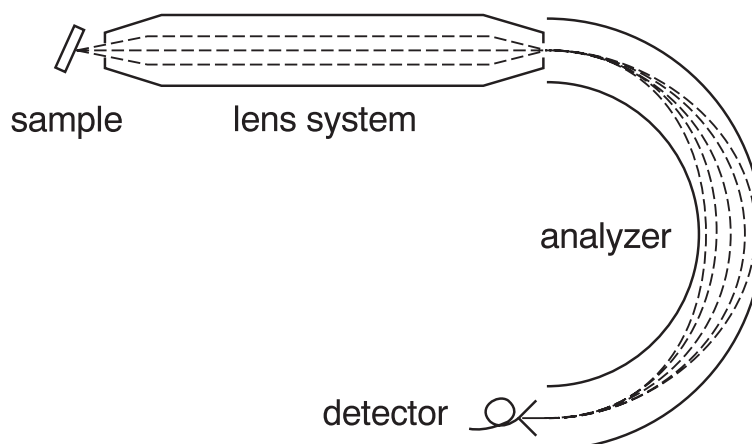


Figure 3.10: Scheme of a HMA used for photoelectron spectroscopy.

Hemispherical Analyzer (HMA)

In photoelectron spectroscopy, hemispherical analyzers are widely in use. Their main advantages are the high resolving power and the possibility to add a fine-focusing lens system in order to minimize the sampling area. Such a lens system can also be used to shorten the accepted angle of collected photoelectrons which is a prerequisite for ARUPS.

For obtaining energy resolved electron spectra, the sample is usually grounded, but in special cases – for example to record the onset of UPS spectra – a fixed BIAS voltage is applied to the sample.

Cylindrical Mirror Analyzer (CMA)

In the set-up shown in figure 3.11 two cylindrical mirror analyzers are mounted one after another to improve resolving power. In such a standard set-up for AES, the electron gun is mounted inside the CMAs. The electron beam of about 3 keV energy is directed to the sample and the emitted electrons are discriminated according to their kinetic energy when passing the two cylindrical mirror analyzers. In order to get best discrimination between the Auger signal and the background of secondary electrons, the signal is generally differentiated by a lock-in amplifier.

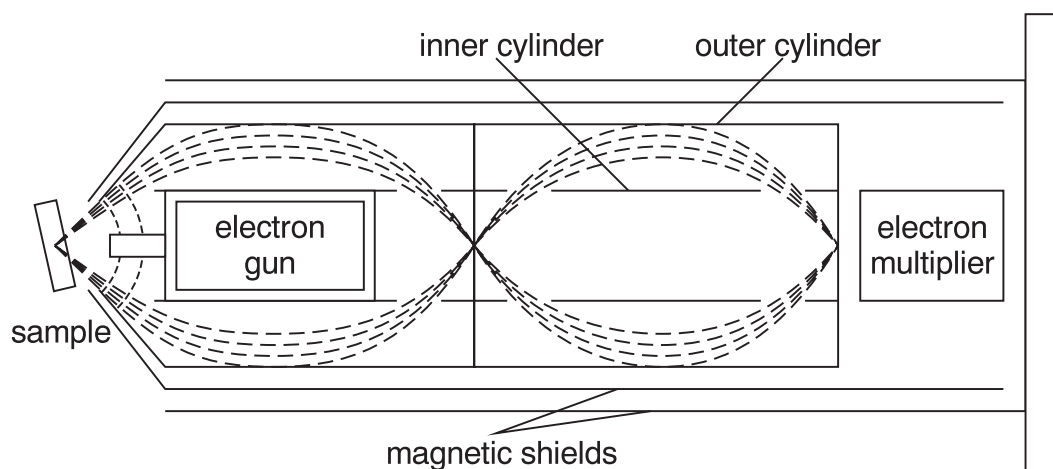


Figure 3.11: Set-up for an Auger electron spectrometer with two CMAs as energy analyzer.

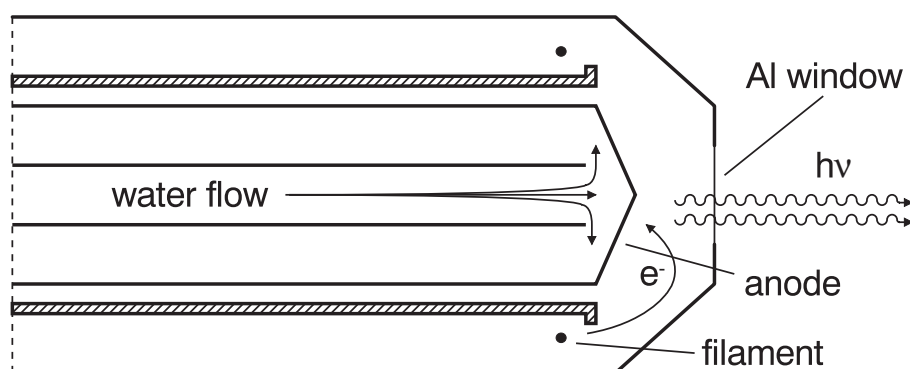


Figure 3.12: Scheme of a water-cooled twin-anode X-ray source.

Light Sources for Photoelectron Spectroscopy

In order to excite photoelectrons light of sufficient energy is needed. This condition is fulfilled by ultraviolet and X-ray photons. In the case of laboratory light sources, on the one hand standard X-ray anode sources are used and on the other hand the resonance discharge lamps in the ultraviolet region.

X-ray sources For producing X-rays, electrons are accelerated towards an anode where characteristic X-ray lines and the continuous background of the bremsstrahlung are excited. Only monochromatic or at least almost monochromatic light is of interest in XPS. Since the line-width

of the dominating characteristic X-rays is also important, two anode materials, Mg and Al, are commonly in use. Often both materials are combined to a twin-anode system.

In figure 3.12 a scheme of such an X-ray source is shown. The anodes are cooled by a continuous flow of cooling water to transport the heat (at operating powers around 200 W) away from the anode material. The thin aluminium window between anode and sample has two reasons. One reason is to protect the sample from electrons and desorbing material and the other reason is the filtering effect of Al which has a adsorption edge just before the interesting X-ray lines and therefore reduces the Bremsstrahlung background.

Resonance discharge lamps Since there are no windows available for photon energies used in UPS (10-50 eV), a special design is necessary to avoid a pressure increase in the main chamber when using resonance discharge lamps. The helium is inserted into the discharge region by a dosing valve and the glass capillary, which is open to the main chamber, is pumped in two steps to avoid helium entering the main chamber. The pressure in the discharge region is around 1 mbar for He I radiation and is reduced to 0.1-0.2 mbar for He II radiation. The pressure increase in the main chamber can be controlled in this way to be not higher than 10^{-8} - 10^{-9} mbar.

Synchrotron radiation In particle physics, the loss of energy by radiation from charged particles in the synchrotron rings is a significant problem. This is due to the fact that an accelerated charged particle emits light and therefore loses energy. When the particles approach light speed, the radiation is more and more directed in its motion and concentrated within a very narrow angle of space. Since there are only few bunches of particles (often only one) in the ring, the radiation is pulsed – resulting in a broad frequency spectrum. These almost ideal light sources offer continuous, focused and polarized high intensity light.

In the last decade more and more synchrotrons were built that were specially designed to deliver optimum photon intensity. For this reason strong bending magnets, wigglers and undulators were developed and added to these rings which bend the beam with strong magnetic fields leading to higher and higher photon fluxes. For examples and details see Ref. [15].

3.1.4 Secondary Ion Mass Spectrometry (SIMS)

A primary ion beam (for example Ar^+ , O_2^+ , Cs^+) in an energy range of 1-15 keV is directed to the sample causing a sputter cascade through which atoms, electrons, and ions are emitted from the sample. These ions are analyzed by a mass spectrometer (quadrupol-, magnetic sector- or time-of-flight- spectrometers), leading to a secondary ion mass spectrum of the sample's surface. With its very low detection limits down to the ppb range (depending on the element), this method is extremely useful to get fast information about the chemical composition of the sample. Although qualitative analysis is fast and especially metals are easy to distinguish in the mass spectra, there is a lack of quantitative information since the process of secondary ion production is not yet fully understood.

In the present work this method has only been used for ex-situ characterization of the sensor samples to give an overview about the impurities. The SIMS system is described elsewhere in detail [149] and will not be further treated here.

This method yields – dependent on the primary ion beam voltage and current – high surface sensitivity, but has the main drawback of eroding the sample during measurement. Only at very low primary ion currents and thus lower sensitivity, it can be assumed that the sample is not significantly changed during measurement (SSIMS: Static SIMS). At higher primary ion fluxes, it is possible to record a depth profile of the sample (dynamic SIMS). Imaging can be done either by using a lens system, sector field and finally channelplates as detector, or by focusing the primary ion beam to a small spot and scanning it across the sample (similar to the SEM). For further information see for instance Ref. [5, 10, 166].

3.2 Geometrical Information

Two methods to reveal the geometrical configuration of single crystalline $\text{SnO}_2(110)$ surfaces, Scanning Tunneling Microscopy (STM) and Low Energy Electron Diffraction (LEED), are discussed in the following. STM as a real space technique offers the opportunity to image directly a surface in atomic resolution, while LEED is best suited for fast preparation control by integrating

over comparatively large surface areas around 1 mm^2 . In contrast to the STM, subsurface layers contribute to the LEED pattern because of the considerable mean free path of electrons in solids (see figure 3.3).

3.2.1 Scanning Tunneling Microscopy (STM)

The STM offers the ability of atomically resolved imaging by moving a tip over a surface and adjusting the tunneling current between sample and surface by using a feed-back-loop. This technique takes advantage of the exponential dependency between tunneling current and distance, i.e. with increasing distance d , the current decreases exponentially.

$$I \propto e^{-2\kappa d} \quad (3.11)$$

with $\kappa^2 = \frac{2m}{\hbar^2}(V_B - E)$ and $V_B - E = \Phi$, i.e. the work function of the surface. By assuming a work function of 4-5 eV, κ can be calculated to be approximately 1 \AA^{-1} , resulting in a decrease in the tunneling current of about one order of magnitude for each Ångström in distance (see (3.11)) [8].

This technique was developed by Binnig and Rohrer (Nobel Prize in Physics, 1986) who also performed first experiments in the early 80s on Au reconstructions. Their most spectacular results during the beginnings of this technique was the clarification of the 7×7 reconstruction on the Si(111) surface [7]. Up to now this technique has given access to a much more detailed view into materials' surfaces than ever before. Although the interpretation of STM images is not easy and controversially discussed, especially for binary and ternary compounds like for example metal oxide surfaces this technique has become one of the predominant methods to study clean surfaces. Together with theoretical calculations of the local density of states on single crystal surfaces, reasonable interpretation is possible.

STM: Principle of Operation

Figure 3.13 shows a typical set-up of a STM. The tip is moved across the sample by x-, y- and z-piezo-drives and the distance between tip and sample is kept constant by keeping the tunneling current between tip and sample constant by adjusting the z-piezo. The voltage applied to the z-piezo delivers the height information. Although this mode of operation – called constant current

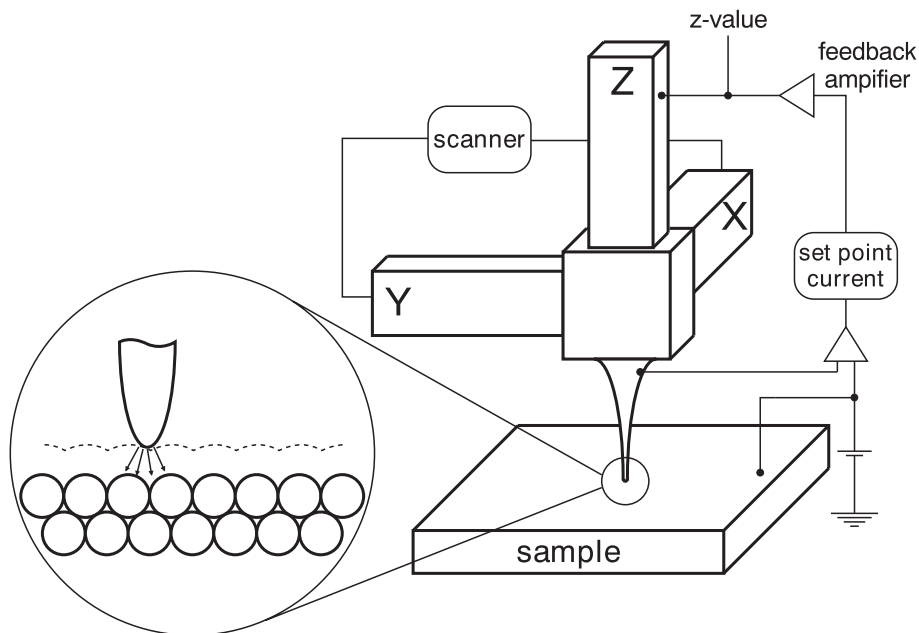


Figure 3.13: Scheme of a STM.

mode – delivers some kind of height information, the resulting data has to be carefully treated. Not only topological structures, but also electronic structures like vacancies or changes in the work function can lead to a variation in the tunneling current and therefore to a variation in the $I(z)$ behavior (3.11).

3.2.2 Low Energy Electron Diffraction (LEED)

This method – as a diffraction technique – can only be used to characterize periodic surface structures. Despite recently developed atomically resolved real-space techniques, like STM and AFM, it is still widely in use and important to control the preparation of clean and well-ordered single crystal surfaces. It is not only possible to reveal the kind of surface ordering and the size of the surface unit cell, but also to get an idea about the surface roughness and the mean terrace width by considering the broadness of the diffraction spots. For these investigations, SPALEED (Spot Profile Analysis LEED) was developed, but lost importance after the development of the STM.

The diffraction of electrons on periodic structures is well-known and the wavelength of an

electron of momentum p can be described by the De Broglie relation $\lambda = \frac{h}{p}$. In this way it is easily possible to estimate the wavelength of electrons of a certain energy which should be in the Ångström regime for studying a surface in atomic dimensions. For typical electron energies in LEED of $E_{kin} = 100$ eV, the wavelength can be calculated to be around 1.2 \AA , i.e. in a suitable range.

Diffraction by a two-dimensional Lattice

In the following, it shall be presupposed that the scattered intensity of a given charge distribution $\rho(\mathbf{r})$ can be described as the Fourier transform $F(\mathbf{r}^*)$ with \mathbf{r}^* denoting a reciprocal lattice vector:

$$F(\mathbf{r}^*) = \int_A \rho(\mathbf{r}) e^{2\pi i \mathbf{r}^* \cdot \mathbf{r}} d\mathbf{r} = T[\rho(\mathbf{r})] \quad (3.12)$$

An excellent derivation of this relation based upon Bragg's law is given in Ref. [54]. The further description of diffraction by a crystal given in this reference is modified for a two-dimensional lattice in the following.

The lattice function of a two-dimensional lattice is given by:

$$L(\mathbf{r}) = \sum_{u,v=-\infty}^{+\infty} \delta(\mathbf{r} - \mathbf{r}_{u,v}) \quad (3.13)$$

with δ as the Dirac function and $\mathbf{r}_{u,v} = u\mathbf{a} + v\mathbf{b}$. The electron density function for the infinite lattice $\rho_\infty(\mathbf{r})$ can be calculated by the convolution between the lattice function $L(\mathbf{r})$ and the electron density distribution within a surface unit cell $\rho_M(\mathbf{r})$:

$$\rho_\infty(\mathbf{r}) = \rho_M(\mathbf{r}) * L(\mathbf{r}) \quad (3.14)$$

which is – in the reciprocal space – simply a multiplication between the two Fourier transforms:

$$F_\infty(\mathbf{r}^*) = T[\rho_\infty(\mathbf{r})] = T[\rho_M(\mathbf{r})] \cdot T[L(\mathbf{r})] \quad (3.15)$$

$$= F_M(\mathbf{r}^*) \cdot \frac{1}{A} \sum_{h,k=-\infty}^{+\infty} \delta(\mathbf{r}^* - \mathbf{r}_{\mathbf{H}^*}) \quad (3.16)$$

where A is the area of the surface unit cell ($\frac{1}{A}$ results from the integration in (3.12)) and $\mathbf{r}_{\mathbf{H}^*} = h\mathbf{a}^* + k\mathbf{b}^*$ a reciprocal lattice vector of the surface. It can be easily seen in (3.16) that there is

only intensity in certain directions, i.e. $\mathbf{r}^* = \mathbf{r}_{\mathbf{H}}^*$ must be fulfilled. This restriction leads to the diffraction pattern which is modulated by the Fourier transform of the electron density distribution $F_M(\mathbf{r}^*)$.

One implication which results from experimental restrictions is the so-called 'phase-problem' in crystallography. It is only possible to record diffracted intensities $|F_M(\mathbf{r}_{\mathbf{H}}^*)|$ at a certain reciprocal lattice vector $\mathbf{r}_{\mathbf{H}}^*$ under losing the phase $\phi_{\mathbf{r}_{\mathbf{H}}^*}$. Since the translational information is coded in the phase of the scattered wave package, it is not possible to reveal the positions of certain atoms on the surface just by a Fourier transform of the diffraction pattern [54].

Description of Overlayer Structures

The most general approach to describe a certain reconstruction was proposed by Park and Maden (see Ref. [175]). Starting from the primitive translation vectors \mathbf{a} and \mathbf{b} of the substrate, i.e. the bulk periodicity, the translation vectors of a surface reconstruction \mathbf{a}' and \mathbf{b}' can be described by a two-dimensional transformation, represented by the matrix G_{ij} :

$$\mathbf{a}' = G_{11}\mathbf{a} + G_{12}\mathbf{b} \quad (3.17)$$

$$\mathbf{b}' = G_{21}\mathbf{a} + G_{22}\mathbf{b} \quad (3.18)$$

A much more convenient, but not that versatile nomenclature was proposed by Wood [174] and is commonly used today. It is based on the substrate lattice vectors and describes the reconstruction of a surface as multiples of the bulk lattice vectors and – if necessary – with an additional angle. A surface representing the bulk periodicity would be named $p(1 \times 1)$ or more easy 1×1 , i.e. a primitive lattice with the same lattice vectors than the bulk termination. Centered structures are denoted for example $c(2 \times 2)$ and rotated surface structures for example $\sqrt{3} \times \sqrt{3}/R30^\circ$ (see figure 3.14 a) and b)).

LEED: Principle of Operation

A monochromatic electron beam with typical energies around 0–300 eV is directed to the surface. The reflected electrons are discriminated by their energy and only the electrons without any energy loss are selected and imaged on a fluorescent screen (see figure 3.15).

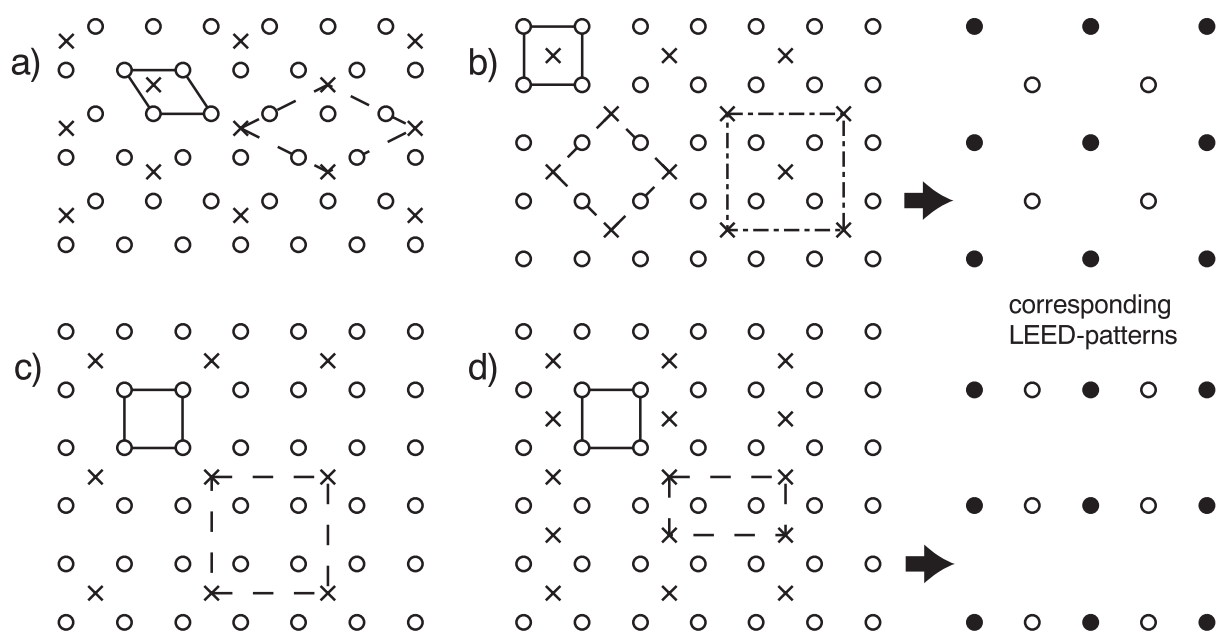


Figure 3.14: Overlayer structures on hexagonal and square substrate lattices. a) shows a $(\sqrt{3} \times \sqrt{3})/R30^\circ$ reconstruction on a hexagonal substrate, b) a $c(2 \times 2)$ or $(\sqrt{2} \times \sqrt{2})/R45^\circ$ structure with the corresponding LEED pattern, c) a 2×2 and d) a 2×1 reconstruction with LEED pattern. b), c) and d) refer to a square substrate lattice. In the real space images, the lattice points of the substrate are marked by 'o' and the overlayer structure by 'x'. The 'o' in the LEED pattern schemes denote diffraction spots of the substrate and the intermediate spots 'o' diffraction spots caused by the overlayer (see Ref. [175]).

The first grid is on the same potential as the sample and the opening of the electron gun, that means the backscattered electrons can travel in a field free space. The second (and in this case also the third grid) are on negative potential, selecting only elastically scattered electrons. The third (in this case fourth grid) is again on the same potential with the sample and is there to shield the high positive voltage of the fluorescent screen on which the electrons are accelerated.

The shown four-grid optics is only needed for high energetic resolution, when using the system as a retarding field analyzer to collect Auger electrons. In LEED mode the two inner meshes are on the same potential. Also the third grid is not really needed, but results in a somewhat higher image quality. Actually the LEED system in the spectrometer described in

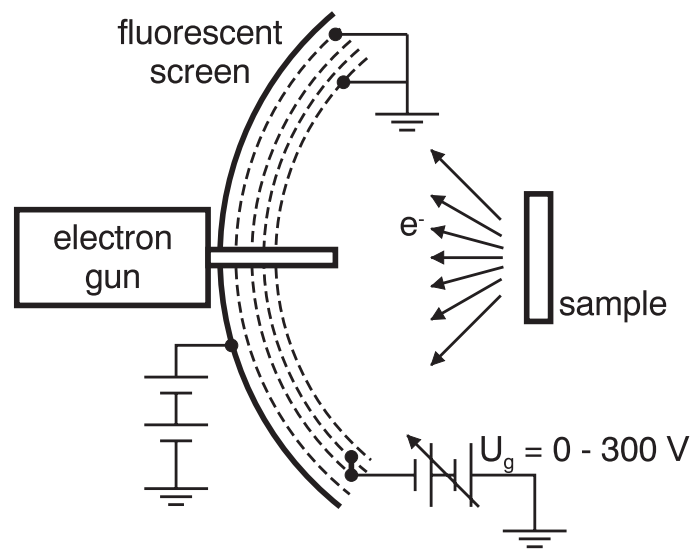


Figure 3.15: Operation principle of a four-grid LEED system

section 5.1 has only two grids and yields similar performance than three grid optics.

Part II

Experimental

Table of Contents

4	Sample Preparation	73
4.1	Sample Preparation of Single Crystalline SnO ₂	73
4.2	Thick Film Sensors	76
4.2.1	Production of SnO ₂ Nanocrystals by a Sol-Gel Method	76
4.2.2	Sensor Fabrication	78
	Gas Test Measurements	78
5	Spectrometers	81
5.1	XPS / UPS / LEED	81
5.2	STM / LEED	82
5.3	MAXlab, Beamline I311	83
6	Data Evaluation	85
6.1	Factor Analysis	85
6.2	Peak Fitting	86

Chapter 4

Sample Preparation

4.1 Sample Preparation of Single Crystalline SnO₂

SnO₂ single crystals grown by the Helbig method (see section 2.1.2) were oriented by Laue diffraction in the (110) direction within $\pm 5^\circ$ (see figure 4.1), cut to a size of $3 \times 4 \text{ mm}^2$ and polished.

The main implication when preparing SnO₂(110) by sputtering and annealing (S&A) is the high temperature needed for annealing (up to 1200 K). Two different methods turned out to be most efficient. One method is heating by electron bombardment of the sample plate and the other is mounting the sample on a platinum foil that is only connected by two platinum wires ($\text{\O} = 0.5 \text{ mm}$) to the sample holder. Heating is performed by passing a current of up to more than 10 A through the wires.

The heating by electron bombardment was applied to the tantalum sample plates used for STM measurements. In this case mechanical stability is a prerequisite and mounting just on two wires is not advisable. Resistive heating was applied for preparation in photoemission and LEED investigations.

Both methods have the main advantage that the heating power around 10 W is concentrated on the sample plate which therefore is, except for the filament in electron bombardment heating and the platinum wires for resistive heating, the hottest part during annealing. In this way, outgassing

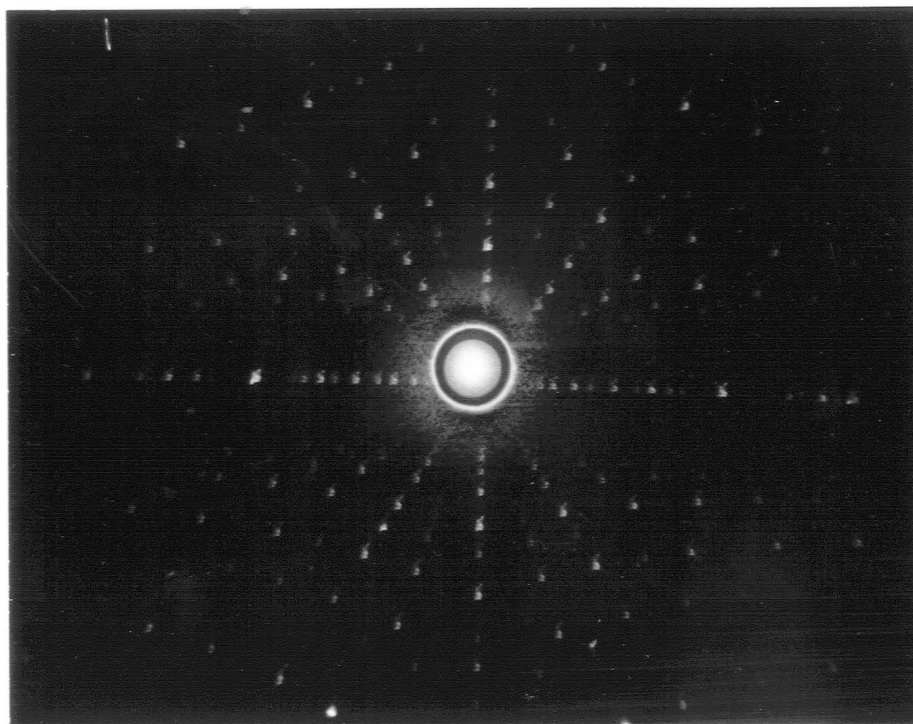


Figure 4.1: Laue diffraction pattern of a (110) oriented SnO_2 single crystal sample.

from the sample holder and from the sample rod can be avoided. After sufficient annealing times the pressure can be maintained below 10^{-9} mbar even at temperatures around 1000 K at the sample plate.

For sputter cleaning of the sample, argon ion guns were used. The kinetic energy of the ion beam was around 500-1000 eV and the current density around $1 \mu\text{A}/\text{cm}^2$. The latter value is difficult to estimate but reflects the typical performance of standard sputter guns. It turned out to be essential not to sputter perpendicular to the sample surface. Such a sputter treatment lead to highly disordered crystals with characteristic centered LEED spots (see figure 7.2 F). Sputter angles between 20° - 45° to the surface resulted in low damage and sufficient cleanliness. For the influence of the sputter angle on the surface topography and for the possibility of ion-beam polishing by glancing incidence irradiation see Ref. [80, 172].

The reconstruction process of oxygen-deficient, freshly sputtered $\text{SnO}_2(110)$ as described in

the literature is summarized in section 2.2.1. Since the revision and extension of the current picture of the reconstruction process of sputtered and annealed SnO₂(110) is one main part of this thesis, it is described in detail in section 7.1.

4.2 Thick Film Sensors

4.2.1 Production of SnO₂ Nanocrystals by a Sol-Gel Method

Starting from an aqueous solution of SnCl₄, Sn(OH)₄ is precipitated by adding NH₃ and cooling down the solution to 0°C.

After some washing steps with bi-distilled water, the so-called 'sol' is obtained that is transformed after some days into the so-called 'gel'. After drying, the gel is heated to temperatures

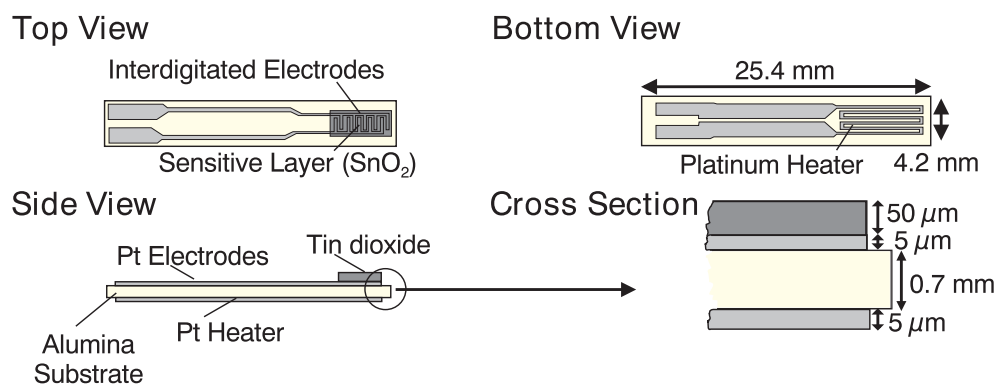


Figure 4.2: Layout of the sensor substrates.

between 300°C and 1000°C (calcination) in an oven. The resulting SnO₂ powder is milled afterwards in order to get as smooth as possible grain surfaces.

Dopants are introduced either directly into the gel before calcination ('gel-impregnation') or after obtaining the calcined powder ('impregnation') by adding metal chlorides (e.g. PdCl₂, H₂[PtCl₆]) to the material. For the latter doping, an additional heating step is needed to reduce the chloride.

In figure 4.3 the preparation steps and the obtained grain size distributions are shown. As-obtained powders have so far been characterized by XPS, Raman spectroscopy and TEM [36, 92]. For the photoemission measurements presented in this thesis, only gas sensors based upon gel-impregnated powder were used (see section 8.2).

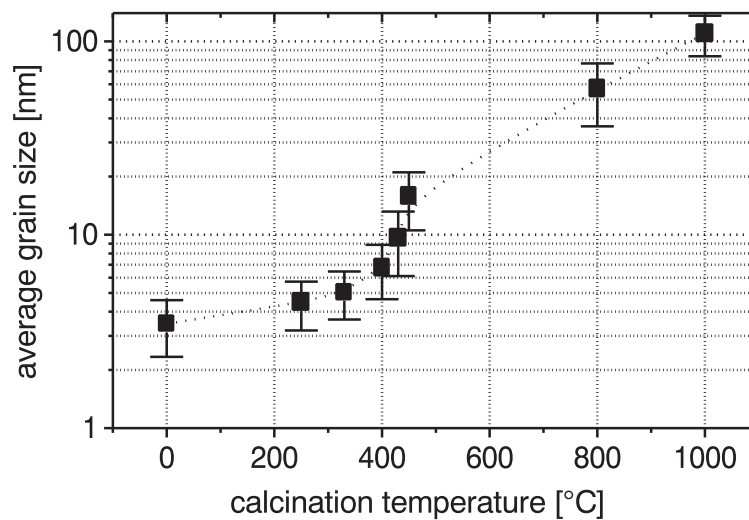
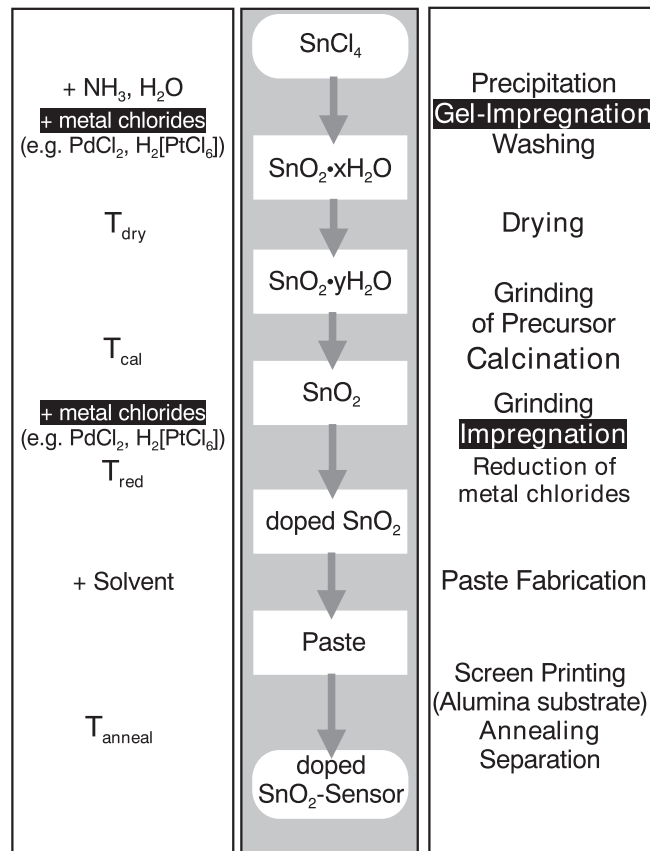


Figure 4.3: Preparation scheme for producing nanocrystalline SnO₂ powder and mean grain size distribution dependent on the calcination temperature.

4.2.2 Sensor Fabrication

The nanocrystalline powder is suspended in an organic solvent and screenprinted onto the substrate. Subsequent heating in air removes the solvent from the sensor.

In figure 4.2 the substrate used in this study is shown. An interdigitated electrode is mounted on top an alumina ceramics and a resistive platinum heater is mounted on the back side. The sensitive layer is printed directly on the interdigitated structure with which the resistance of this layer can be determined.

Gas Test Measurements

As-prepared sensors have been extensively tested by gas test measurements under ambient air conditions towards their conductance and work function response on changes in the gas atmosphere [140].

A setup for measuring simultaneously the work function difference $\Delta\Phi$ between sensor and kelvin probe and the conductance of the sensing layer, together with a typical set of sensor responses to changes in the CO concentration is shown in figure 4.4. By simultaneously recording $\Delta\Phi$ and resistance, the selectivity to distinct gases can be significantly enhanced [69].

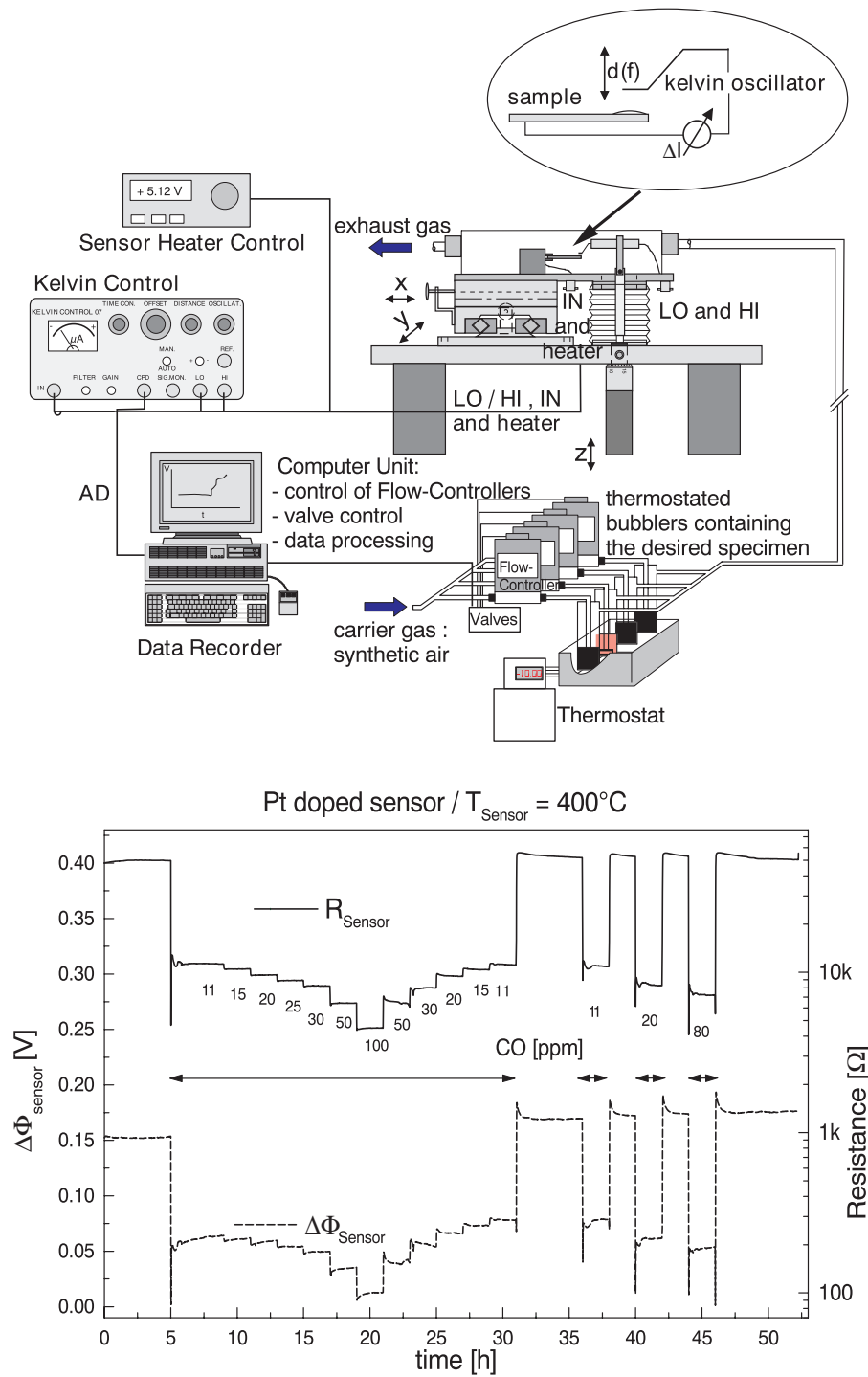


Figure 4.4: Sensor test setup for computer controlled acquisition of conductance and work function difference under a variable gas ambient with typical sensor response curves to a change in the CO concentration.

Chapter 5

Spectrometers

The XPS/UPS/LEED spectrometer described in section 5.1 has been used for monitoring the reconstruction process of SnO₂(110) by XPS and LEED and for UPS He I and He II measurements on sensors as well. With the STM described in section 5.2 the high resolution STM images on SnO₂(110)-4×1 and 2×1 could be obtained. Resonant photoemission spectra were recorded at Beamline I311 at MAXlab, see section 5.3. The SIMS system that has only been used to check the impurities of the sensor samples after performing the resonant photoemission experiments, has been described in detail elsewhere [149].

5.1 XPS / UPS / LEED

Photoemission experiments with laboratory light sources were performed at a combined XPS/UPS/LEED system with separate preparation chamber for sputtering, outgassing and annealing and a load-lock system for fast sample transfer within less than one hour. All analytical techniques are available in one chamber without transferring the sample in between. The manipulator allows translations in all directions and can be rotated around the z-axis. Cooling can be applied through a hollow rod close to the sample holder by liquid nitrogen. Resistive heaters are mounted directly on the sample holders that are equipped with two contacts allowing currents up to 20 A. The base pressure is in the 10⁻¹⁰ mbar range in both, the main and the preparation chamber.

A hemispherical analyzer (Omicron EA125HR [178]) is used to discriminate photoelectrons excited either by a twin-anode X-ray source [182] operated at 200 W or by a home-built Helium resonance discharge lamp to be operated either to deliver He I or He II radiation, dependent on the He partial pressure in the discharge region. In order to check the surface periodicity, a two-grid retractable rear-view LEED optics [181] is attached to this chamber. The pressure during measurement was $1 - 2 \times 10^{-9}$ mbar in XPS mode, $2 - 8 \times 10^{-9}$ mbar for UPS and below 10^{-9} mbar for LEED operation.

Binding energies of the UPS spectra were calibrated by the Fermi level of a freshly sputtered platinum foil in electrical contact with the sample. The energy resolution was determined by the shape of the Pt Fermi level to a value around $\text{FWHM} = 130$ meV. The pass energy of the analyzer was set to 5 eV and the sample was biased to a voltage of -10 eV.

XPS spectra were recorded with the sample shortened to ground and at a pass energy of 20 eV for small region scans ($\text{FWHM} = 0.9$ eV at Ag $3d_{5/2}$) and a pass energy of 50 eV for survey scans ($\text{FWHM} = 1.6$ eV at Ag $3d_{5/2}$). The energy scale was calibrated by Ag and Pt core-levels.

5.2 STM / LEED

STM measurements were performed on an Omicron STM 1 system (located at Materials Physics, KTH Stockholm [176]). Preparation control is possible with a rear-view LEED system and samples were prepared by S&A treatment. Samples were inserted via a bakeable load lock. The base pressure was better 5×10^{-10} mbar in the whole system and was not significantly increased when applying the measurement techniques.

All presented STM images were recorded at a positive sample BIAS of $+1.5$ V which implies tunneling into the surface, i.e. imaging of unoccupied surface states. The sample current was adjusted to 1 nA and only for the measurements on the Pd/SnO₂(110)-4x1 surface reduced to 0.1 nA (see section 7.2.3 for an explanation). A variation of the tunneling current towards lower or even negative sample BIAS resulted in unstable tunneling behavior. The tip consisted of a tungsten needle that was sharpened by rapidly scanning at high tunneling current (up to 10 nA) across a Si(111) single crystal surface.

5.3 MAXlab, Beamline I311

Beamline I311 is an undulator based soft X-ray beamline for high resolution XPS and X-ray Absorption Spectroscopy (XAS). The energy range is 30-1500 eV with an energy resolution of $E/dE = 5 \times 10^3 - 2 \times 10^4$. The system consists of separate analyzer and preparation chambers accessible via a long-travel manipulator. The preparation chamber includes the usual equipment for preparation and characterization of surfaces (ion sputtering gun, LEED optics, heating and cooling facility). A hemispherical electron energy analyzer (SCIENTA SES200 [179]) is used for discriminating photoelectrons according to their kinetic energy.

The spectra were calibrated to the Fermi level of a metal in electrical contact with the sample and the instrumental resolution was tuned to FWHM = 30 meV for the valence band spectra up to a photon energy of $h\nu = 130$ eV and to FWHM = 100 meV for the core-level spectra of SnO₂ at a photon energy of $h\nu = 630$ eV. The samples were shortened to ground for all measurements.

Chapter 6

Data Evaluation

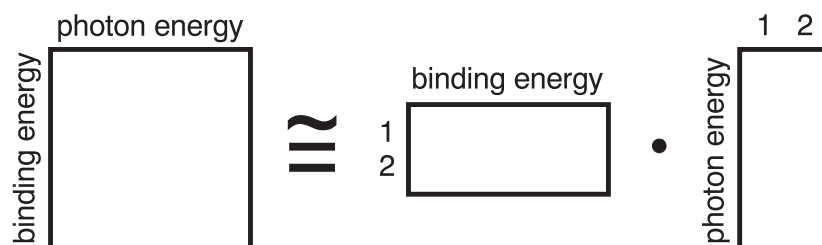
6.1 Factor Analysis

The final goal of factor analysis is the determination of factors with which a given dataset can be completely described. In our case, we have a set of z valence band spectra with N values in each spectrum. Every spectrum is represented by a column-vector in the Matrix $[\mathbf{D}]$. By factor analysis it is possible to decompose this matrix into a product of two matrices [78]:

$$\begin{aligned} [\mathbf{D}] &= [\bar{\mathbf{R}}] \cdot [\bar{\mathbf{C}}] \\ (N, z) &= (N, K) \quad (K, z) \end{aligned} \tag{6.1}$$

That means $[\bar{\mathbf{R}}]$ contains K factors (or components) with $K \leq z$. $[\bar{\mathbf{C}}]$ contains the fractions of each component with which $[\mathbf{D}]$ can be described by linear superposition. Of course, equation (6.1) is usually not fulfilled in an exact manner. This equation would better be written as $[\mathbf{D}] \approx [\bar{\mathbf{R}}] \cdot [\bar{\mathbf{C}}]$. Now, the main task is to find the relevant factors with which the original dataset can be best reproduced.

This method can be explained clearer when writing the actual measurement parameters and data into the matrices. This would result in the following scheme:



When we compare this scheme with equation (6.1), N denotes the binding energy, z the photon energy and K the factors which are in this case factor 1 and 2.

Actually a number of methods exists with which these factors can be extracted from a given dataset, for example the maximum likelihood method, Principal Components Analysis (PCA) and others. In this study, PCA was applied to extract the factors. The data analysis was performed with the STATISTICA software package by using the 'Factor Analysis Module' [151].

6.2 Peak Fitting

There are several aspects involved in the broadening of core-level signals in photoelectron spectroscopy. On the one hand, there is the instrumental aspect which is not longer relevant at today's high-resolution photoemission beamlines like the one described in section 5.3. Such broadening which results from the natural line width of X-ray sources (see table 3.1), the resolution of the monochromator and the transmission function of the electron energy analyzer, result mainly in a Gaussian broadening of the core-level peaks.

On the other hand, there are lifetime effects (Lorentzian shape [64]), phonon broadening (Gaussian shape [21, 22]) and relaxation effects after photoemission (asymmetric tail, but often also additional lifetime broadening [9, 43]). The latter effect is best visible on metals with high density of states at the Fermi level, like for example Pt.

In the present case, when considering the SRPES core-level spectra, instrumental broadening is negligible and only lifetime and phonon broadening is of relevance. The Voigt profile leads to very good fitting results by adjusting the amount of Lorentzian or Gaussian portion to the curve

form. SnO_2 shows only little Lorentzian width in the Voigt curve of the Sn $4d$ and Sn $3d$ core-levels (≈ 0.3 eV at the Sn $3d_{5/2}$ core-level) but significant Gaussian broadening (≈ 1.1 eV at the Sn $3d_{5/2}$ core-level). It has been shown that phonon broadening is the dominating broadening mechanism in full valence compounds like MgO or Al_2O_3 [2] and it is obviously dominating in SnO_2 as well.

Background subtraction was applied by adjusting a polynomial or logistic background to the spectrum which resulted in very good agreement between experimental data and curve fitting.

Part III

Results and discussion

Table of Contents

7	Geometric Structure	93
7.1	Reconstruction Process	94
7.1.1	Monitoring the Reconstruction Process by XPS and LEED	97
	Data Treatment	97
	Results	99
7.2	STM Imaging	100
7.2.1	Atomically resolved Imaging on SnO ₂ (110)-4×1	101
	Large Area Scans	102
	Terrace Steps	102
7.2.2	STM on highly defective SnO ₂ (110)	105
	STM Images of 2×1 Structures	106
7.2.3	Pd-Clusters on SnO ₂ (110)-4×1 imaged by STM	109
7.3	Discussion	110
8	Electronic Structure and Chemical Composition	113
8.1	SnO ₂ (110)	114
8.1.1	SRPES Core-Level Spectroscopy	114
8.1.2	ResPES on SnO ₂ (110)-4×1 and Sputtered SnO ₂ (110)	116
	Results and Data Evaluation	120
	Discussion of the Results	121
	Discussion of the observed Resonances	123
8.2	Nanocrystalline SnO ₂	126
8.2.1	Laboratory Source UPS Results	128
8.2.2	ResPES on doped and undoped Gas Sensors	129
	SRPES Raw Data	130
	Difference Spectra	130
	CIS Curves	133

	Factor Analysis Results	133
	SIMS Spectra	136
8.3	CO Exposure monitored by UPS	140
9	Conclusions and Outlook	143

Chapter 7

Geometric Structure

For the measurements presented in the following it was essential to control the UHV preparation by LEED. Since the reconstruction process of sputtered and annealed $\text{SnO}_2(110)$ is not only dependent on annealing temperature but also highly dependent on the history of the sample, for instance on the applied sputter treatment, LEED has to be used continuously to ensure a reproducible preparation procedure. STM, as a real-space technique, offers not only the direct determination of the surface structure, but is also useful to estimate the degree of surface ordering from large area scans which are, with for example $100 \times 100 \text{ nm}^2$, still orders of magnitude smaller than the integration area of LEED (around 1 mm^2). Since STM measurements are very time consuming, previous control of the surface periodicity by LEED is of great importance before trying STM imaging.

In contrast to the results published by other authors up to now, it will be shown that the evolution of a 4×1 reconstruction can not only be observed on a freshly sputtered surface after annealing to subsequently higher temperature, but also on already high temperature annealed surfaces which initially exhibit a 1×1 periodicity by annealing again at lower temperature for several hours (see figure 7.1 and section 7.1). The observation of increasing defect density when annealing the 4×1 to a 1×1 structure gives reason for a modified model of the reconstruction process of oxygen-deficient $\text{SnO}_2(110)-4 \times 1$ (see section 7.3). Another interesting observation is a localized zigzag structure in STM images of highly defective terraces which can be explained

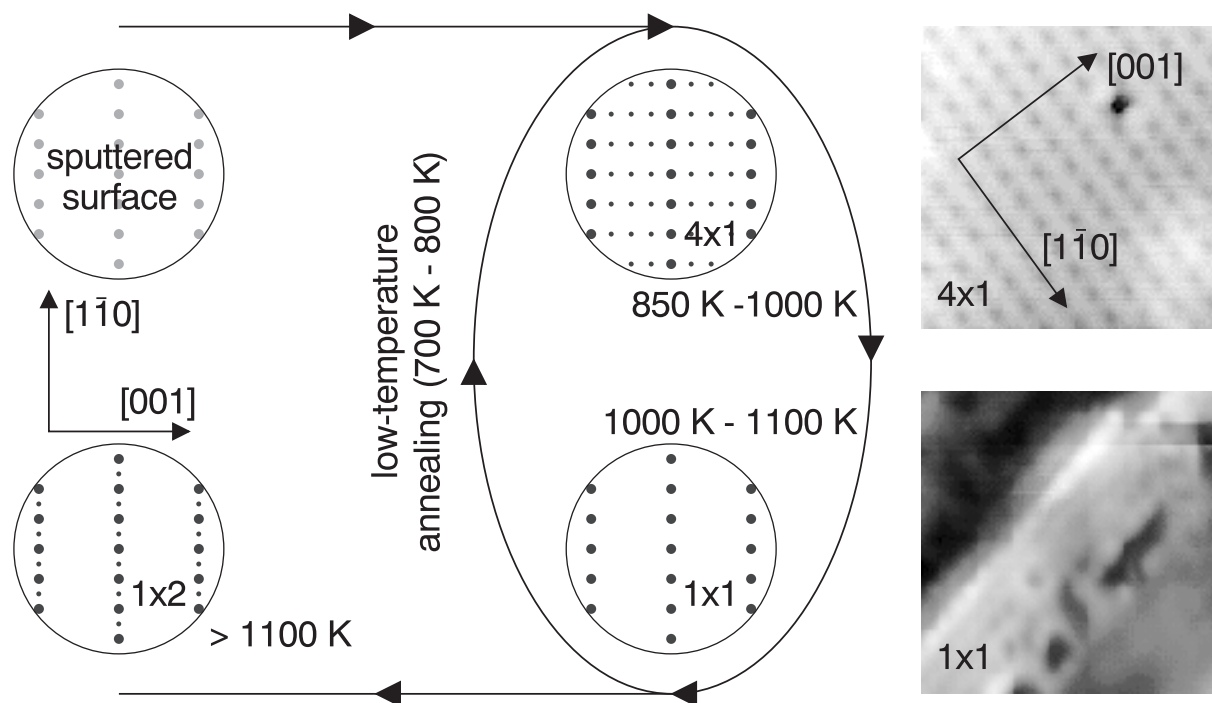


Figure 7.1: Scheme of the reconstruction process of oxygen-deficient SnO₂(110). The STM images show scans of $75 \times 75 \text{ \AA}^2$.

by a 2×1 structure shaped by oxygen vacancies in the surface oxygen rows (see section 7.2.2).

In order to get information about the stoichiometry of the surface during the reconstruction process the XPS O $1s$ to Sn $3d$ intensity ratio was acquired when subsequently annealing the surface to higher temperatures and checking the surface reconstruction by LEED. Another parameter easily accessible when evaluating these spectra is the position of the core-levels delivering information about the band bending at the surface.

7.1 Reconstruction Process

As already described in many studies, sputtered and therefore disordered and oxygen deficient SnO₂(110) shows a sophisticated evolution of LEED-patterns under annealing to subsequently higher temperature (see section 2.2.1 for a detailed literature survey). In agreement with these results, a more or less diffuse 1×1 structure after ion-bombardment, followed by a 4×1 , a 1×1

(with very diffuse and broad 2×1 intensity) and finally a 1×2 reconstruction could be observed. Additionally, after annealing a high-temperature annealed 1×1 reconstructed surface at lower temperature for 12 - 48 h resulting in a very weak 4×1 reconstruction, the same evolution of LEED patterns could be observed again. A 4×1 pattern followed by a 1×1 and finally a 1×2 pattern. The quality of as-obtained reconstructed surfaces could be much increased by initially annealing up to several days. When comparing both preparation methods, it can be stated that the patterns appear on systematically lower annealing temperature for the long-time annealed surface compared to the freshly sputtered surface, indicating the higher initial ordering on the long-time annealed surface.

Figure 7.1 shows a scheme of the above described evolution of LEED-patterns. The temperatures given can differ up to ± 100 K from sample to sample, depending on its history. The 4×1 pattern, observed after annealing a 1×1 or 1×2 reconstructed surface again at lower temperature, appears at lower annealing temperature than the typical annealing temperature for the 4×1 pattern initially observed after sputtering. It can often be improved by raising the temperature again to the 4×1 temperature which is needed when starting from a sputtered surface.

To cut it short, the preparation procedure for the long-time annealed surface was:

- sputtering a well-ordered high-temperature annealed 1×2 reconstructed surface until only a (weak) 1×1 LEED pattern is left,
- several hours annealing to a 4×1 reconstructed surface,
- further annealing at higher temperature to the high-temperature 1×1 surface
- and annealing back to subsequently lower temperatures down to around 700 K, at which the sample stays for at least 48 h.

The sputtered surface was just prepared by sputtering a well-defined 1×2 (after annealing at more than 1100 K overnight) reconstructed surface for about 10 min with Ar^+ ions at 500 eV kinetic energy and a current density around $1 \mu\text{A}/\text{cm}^2$.

The observed LEED patterns, fully reconstructed surfaces as well as intermediate patterns, are shown in figure 7.2. All LEED images were recorded at an electron energy of 58 eV. The im-

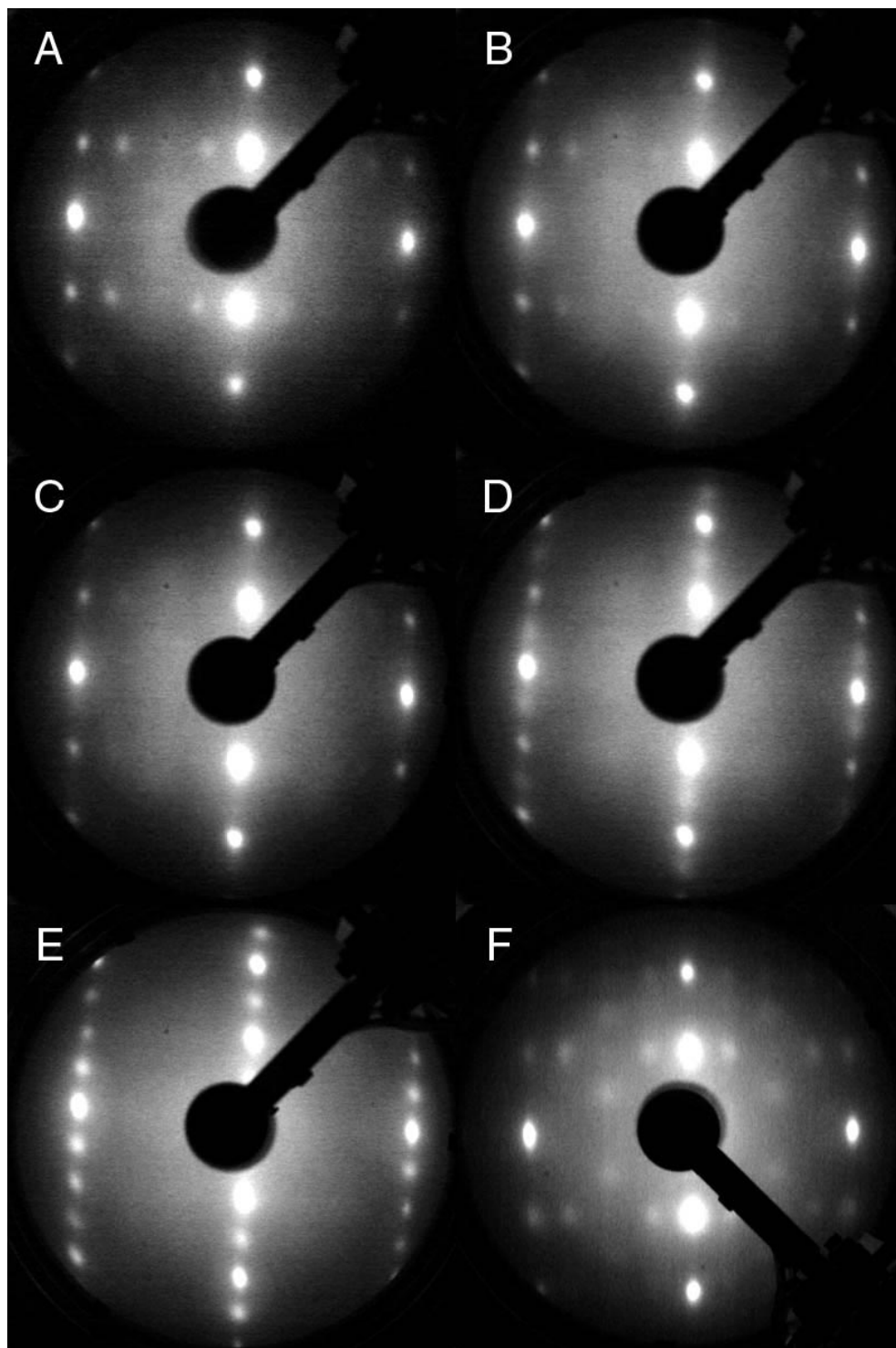


Figure 7.2: Typical LEED patterns ($E_{kin} = 58$ eV) observed during annealing oxygen-deficient $\text{SnO}_2(110)$.

ages A - D were recorded when annealing a low-temperature annealed surface to subsequently higher temperature in steps of around 50 K and annealing time of 30 min at each temperature. Figure 7.2 E shows a well-ordered 1×2 reconstruction after 16 h annealing at 1200 K and Figure 7.2 F is a photograph taken from another crystal which has been treated with heavy ion-bombardment (perpendicular to the surface) before annealing. This heavy ion-bombardment results in centered spots in the LEED pattern at low annealing temperature which were, in this case, still present when annealing the surface to the 4×1 reconstruction.

7.1.1 Monitoring the Reconstruction Process by XPS and LEED

The reconstruction process of oxygen-deficient $\text{SnO}_2(110)$ was monitored by the O/Sn ratio and the core-level shifts obtained from XPS spectra, the LEED pattern and the annealing temperature. The annealing to subsequently higher temperature was performed in 50 K steps with an annealing period of 30 min at each temperature. This period is a compromise between allowing the surface to reach its equilibrium and the necessary measuring time to record the data. Actually, 30 minutes are not sufficient in all cases in order to reach the equilibrium. This can be seen by comparing the temperature necessary to reach a certain reconstruction on the long-time annealed and sputtered surface respectively (see figure 7.3). The surface reconstruction was checked by LEED after each annealing period and the temperature of the platinum sample plate was revealed by a K-type thermocouple spotwelded onto the sample plate during annealing.

Data Treatment

For both surface preparation procedures, for the long-time annealed as well as for the freshly sputtered surface, two complete sets of XPS data were recorded. In order to avoid satellite contributions when revealing the O/Sn ratio and the core-level shifts, the Sn $3d_{3/2}$ and O $1s$ core-levels were evaluated according to their intensity and energetic position. The Sn $3d_{3/2}$ is preferable because the Mg-K $\alpha_{3,4}$ satellites interfere with the Sn $3d_{5/2}$ peak.

For an estimation of statistical errors involved in the data acquisition, three XPS spectra were taken, fitted and evaluated after each annealing step. The corresponding standard deviation from

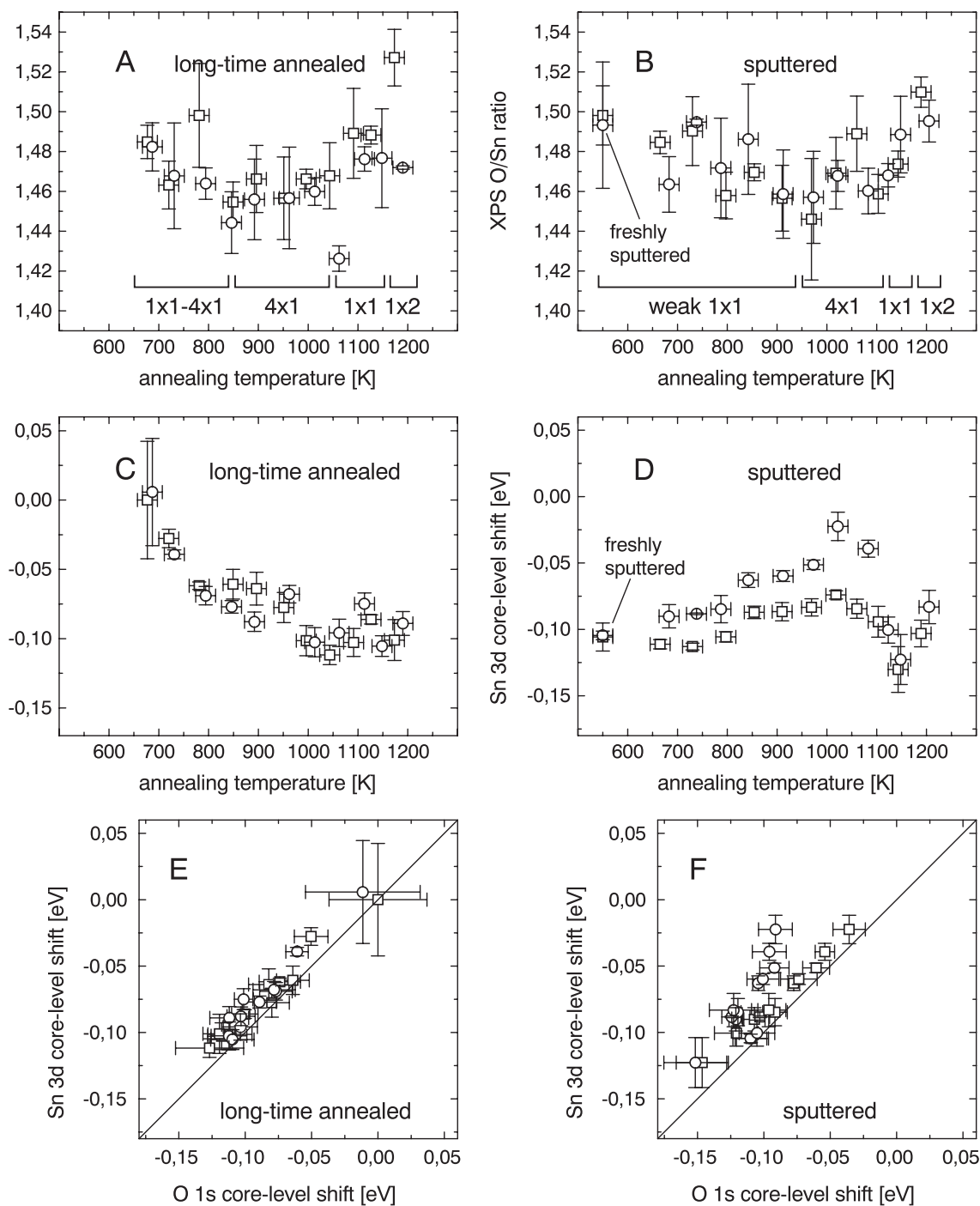


Figure 7.3: O/Sn ratios and core-level shifts of oxygen and tin revealed from XPS spectra during annealing a long-time low-temperature annealed surface and a freshly sputtered surface. For each surface preparation two complete data-sets were recorded which are denoted with a square for the first and a circle for the second run. See text for further details.

the mean value is plotted as an error bar at each measurement point in figure 7.3. The error bar of temperature measurement was estimated to be in the order of 20 K and is plotted as well. The O/Sn ratio is normalized to the corresponding photoionization cross section of the O 1s and Sn $3d_{3/2}$ core-levels at the photon energy of Mg-K α radiation ($h\nu = 1253.6$ eV) [141]. The position of the Sn $3d_{3/2}$ core-level in figures 7.3 C and D is plotted relative to the binding energy of the tin core-level of the first set of spectra in the first series.

For comparing the core-level shifts of oxygen and tin, the relative position of the Sn $3d_{3/2}$ core-level is plotted as a function of the relative position of the O 1s core-level in figures 7.3 E and F for each surface preparation.

Results

The O/Sn ratios in figure 7.3 A and B show surprisingly no significant deviation within the error bars when comparing the two surface preparations to each other. Neither according to the trend of the data points nor to its absolute value. The main difference is due to the appearance of the various LEED patterns as a function of annealing temperature which is shifted towards little higher temperature for the sputtered surface as a result of the sputter damage.

The influence of sputter treatment is most obvious in the core-level shifts of tin and oxygen which correspond very well to each other for each surface termination (see figure 7.3 E and F), but show significant difference at annealing temperature lower 900 K between the two applied surface preparations in figure 7.3 C and D. At high annealing temperature the core-level shifts of both surface preparations come closer to each other. Another observation is the very good reproducibility of the core-level shifts for the long-time annealed surface. In contrast, there is a little different development of the core-level shifts for the two sputtered surfaces as a result of an apparently different sputter damage.

The core-level shifts on the long-time annealed surface are almost the same for oxygen and tin which can most likely be explained by a band bending at the surface. The slight offset in figure 7.3 E may arise from the data treatment. In contrast, there is not only an offset but also a difference in the slope for the sputtered surface in the order of some meV which may be due

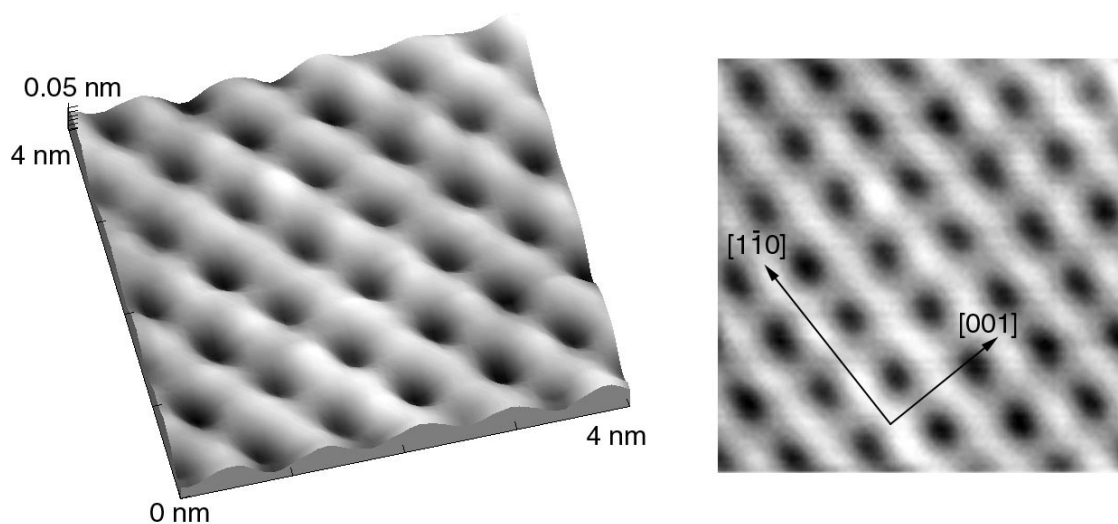


Figure 7.4: $40 \times 40 \text{ \AA}^2$ image of the 4×1 structure. The image is aligned to the 4×1 unit cell size and smoothed by FFT filtering.

to a true chemical shift arising from the strong disorder in the near-surface lattice induced by sputtering (compare Ref. [37, 158]).

7.2 STM Imaging

As a real-space technique, STM offers the ability to image directly the density of electronic states on a surface with even atomic resolution. This density of electronic states is not only dependent on the position of atoms, but also on the binding state of surface atoms, subsurface defects and influences by adsorbates that might be transparent at the chosen BIAS voltage. That means that an interpretation according to only this information is critical. But a detailed comparison of observed structures with a geometric model of the surface can give insight in the nature of the observed features. Nevertheless, only theoretical calculations best based on the actually observed geometry of reconstruction, can lead to an unequivocal statement which features can be assigned to a certain surface atom.

Figure 7.4 shows the typical pattern that could be observed on 4×1 terraces. In the following, an interpretation of the observed contrast is given by comparison of this pattern with the reduced

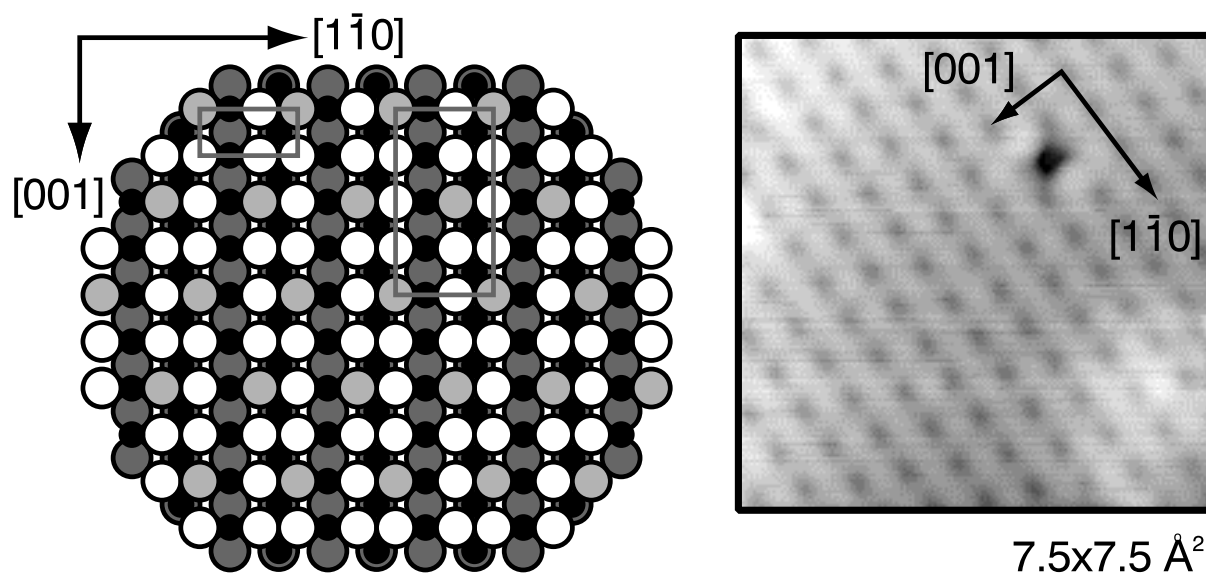


Figure 7.5: Model for the 4×1 reconstructed surface and STM image taken at +1.5 V BIAS, 1.0 nA. The rectangles in the left part of this figure show the 1×1 and the 4×1 unit cell with a size of $3.2 \times 6.8 \text{ \AA}^2$ and $12.8 \times 6.8 \text{ \AA}^2$ respectively. In-plane oxygen vacancies are shaded light grey.

$\text{SnO}_2(110)$ surface and with characteristic terrace terminations that could be observed as well. In section 7.2.2, STM images of highly defective surfaces with a 1×1 pattern in LEED are shown and some features are interpreted.

7.2.1 Atomically resolved Imaging on $\text{SnO}_2(110)-4 \times 1$

Best tunnelling was achieved at a sample BIAS of +1.5 V and a tunnelling current of 1.0 nA. A variation of the sample BIAS down to +1.2 V was possible but results in less image quality. Further reduction of the sample BIAS or the application of a negative voltage lead to an unstable tunnelling. The tunnelling current of 1.0 nA is a good compromise between closely approaching the surface, but not picking up to much adsorbates which finally lead to unstable imaging.

Atomically resolved images of the 4×1 reconstruction could be taken under conditions that imply imaging of unoccupied surface states (+1.5 V BIAS, 1.0 nA). The interpretation of an earlier STM study by Jones et al. is that only oxygen states are visible under these conditions.

This interpretation is supported by comparing the STM images with theoretical calculations [106] on the reduced surface and also taking STM images at different BIAS into account.

But it is also possible to argue just by geometrical reasons. When looking at figure 7.5, it is obvious that the dark area slightly shifted from the middle of the unit cell can only be explained with in-plane oxygen vacancies. That means surface oxygen is imaged under the chosen conditions, resulting in a dark contrast for in-plane oxygen vacancies. It is not possible to model a centered spot shifted in the $[1\bar{1}0]$ direction only with tin atoms as they are all equally spaced to each other.

Large Area Scans

Large area scans show terraces preferably oriented along the $[001]$ direction with often only small width along the $[1\bar{1}0]$ direction. This observation is in agreement with the observed shape of the LEED-spots.

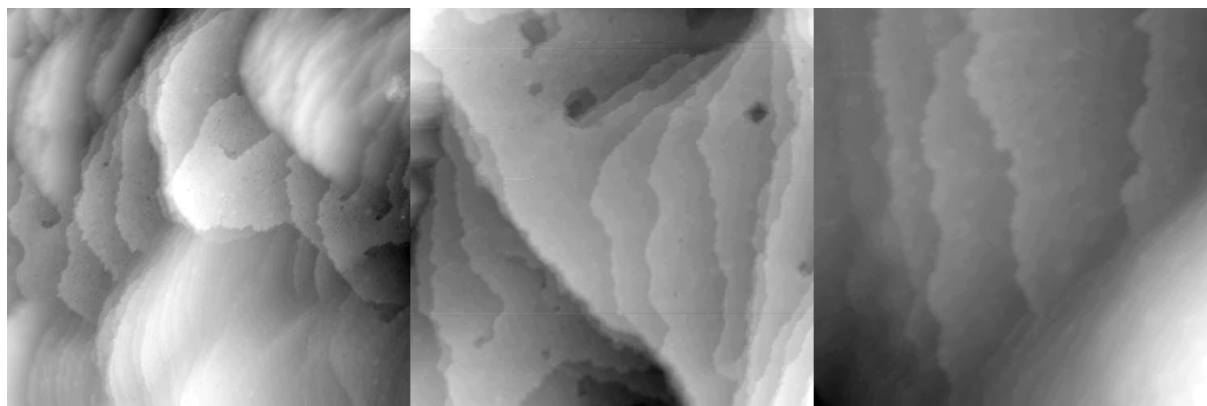


Figure 7.6: Large area scans of $\text{SnO}_2(110)\text{-}4\times 1$ surfaces ($200 \times 200 \text{ nm}^2$, $150 \times 150 \text{ nm}^2$ and $100 \times 100 \text{ nm}^2$ from left to right).

Terrace Steps

The height of terrace steps observed on well-ordered 4×1 surfaces with only little defect density can be explained by half and full unit cell steps of the $\text{SnO}_2(110)$ surface unit cell. Figure 7.7 shows the height of a half unit cell step in the case of a reduced surface termination that is

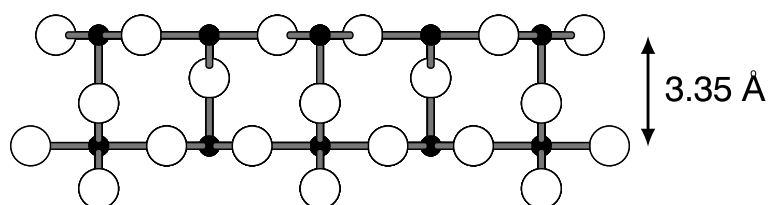


Figure 7.7: Step height expected for a half unit-cell step on SnO₂(110) surfaces.

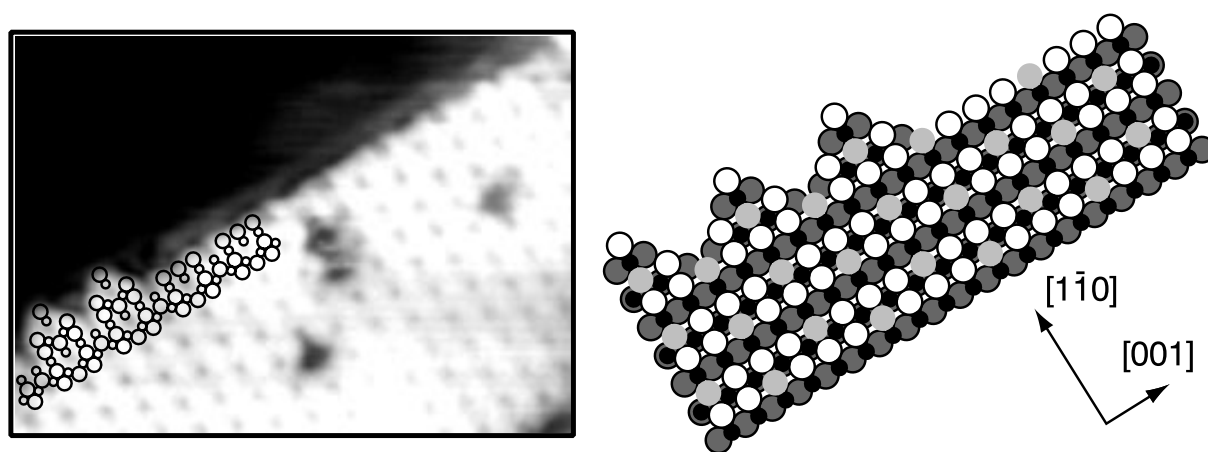


Figure 7.8: Atomistic model for the termination of SnO₂(110) terraces. In-plane oxygen vacancies are shaded light grey.

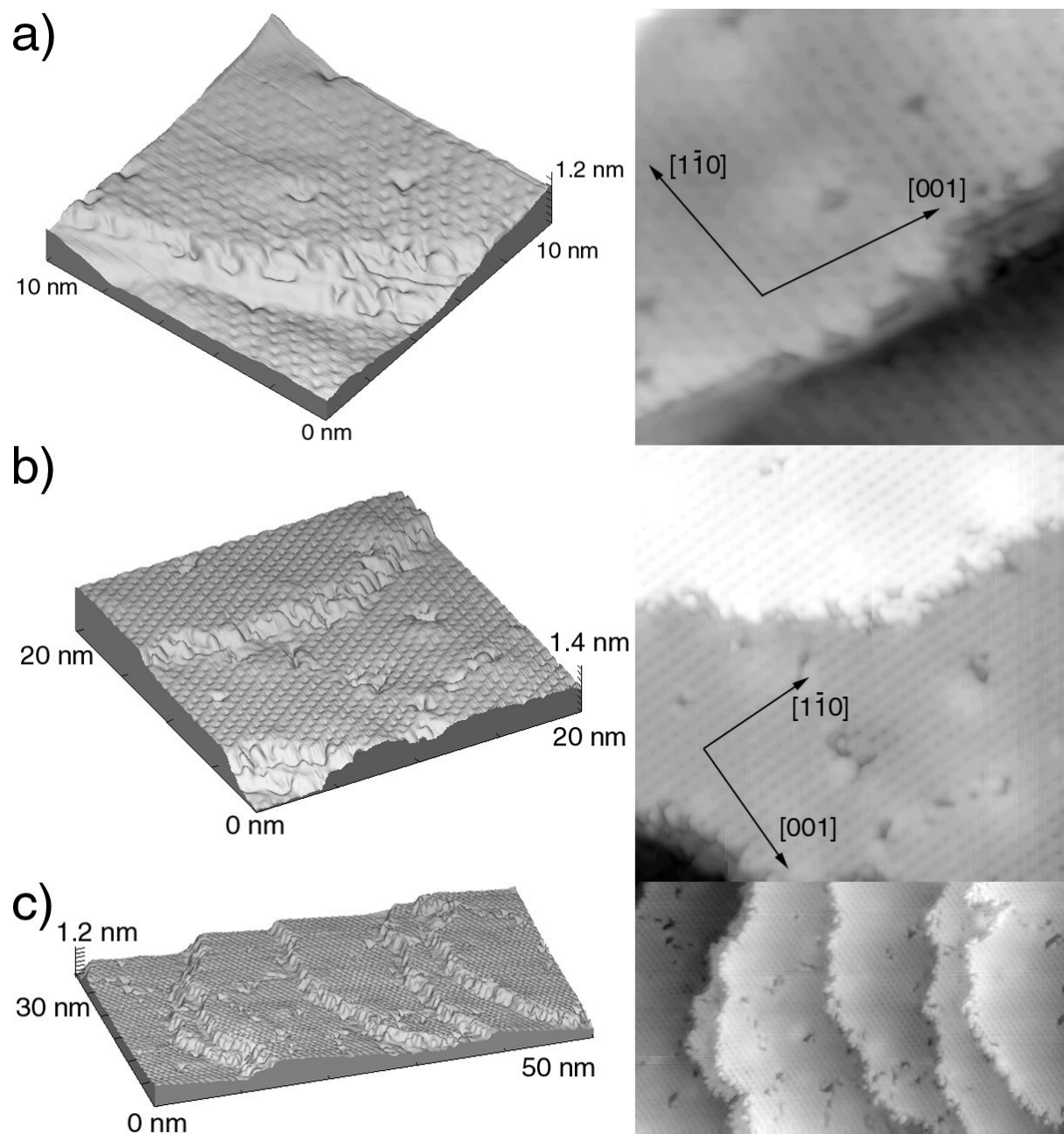


Figure 7.9: STM on step edges of the $\text{SnO}_2(110)\text{-}4\times 1$ surface.

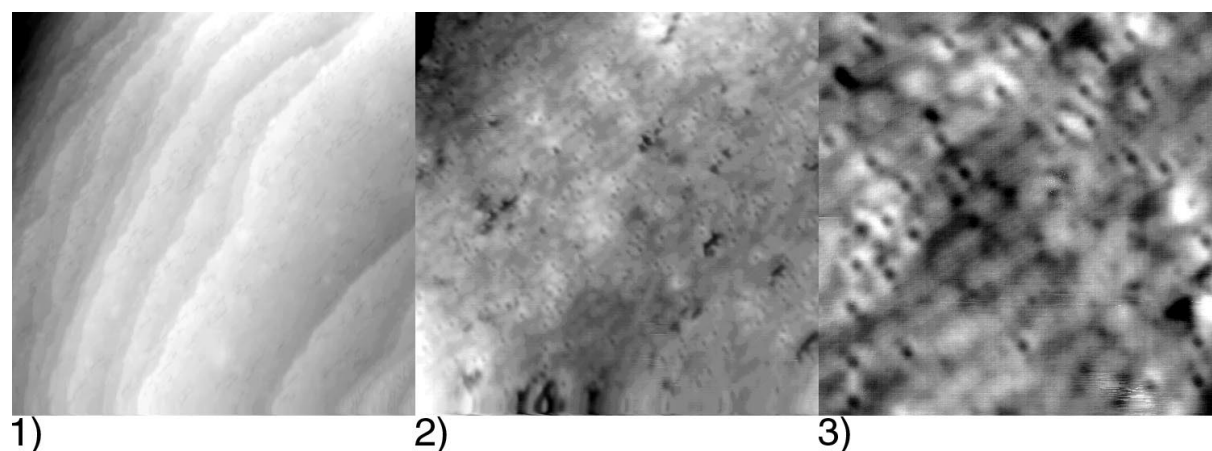


Figure 7.10: Images of highly defective $\text{SnO}_2(110)$ with actually a 1×1 pattern in LEED. Image 1) is a $100 \times 100 \text{ nm}^2$, image 2) a $50 \times 50 \text{ nm}^2$ and image 3) a $20 \times 20 \text{ nm}^2$ scan.

true for S&A treated samples. Not only half unit cell steps but also full unit cell steps, which often show a characteristic 'triangle' termination could be observed. This is explainable by an oxygen vacancy surrounded by three surface oxygens. Figure 7.8 shows such a termination with the proposed model as an overlayer on a STM image. Since tin cations are supposed not to be imaged under the chosen conditions on the 4×1 surface, their positions are arbitrarily chosen. The model coincides very well with the real-space STM images and is a further evidence for the validity of the model proposed by Jones et al. [89].

7.2.2 STM on highly defective $\text{SnO}_2(110)$

After annealing 4×1 surfaces to subsequently higher temperature, the LEED pattern changes to a 1×1 pattern with little 2×1 character that can be observed at low kinetic energies and is visible in the LEED patterns of figure 7.2 B and C as a very weak and broad intensity.

Surprisingly no surface with a regular 1×1 periodicity according to the model of a more or less defective reduced $\text{SnO}_2(110)$ surface could be observed. This leads to the assumption that the observed 1×1 LEED pattern is not due to surface ordering but to the subsurface contribution of a highly disordered and extremely defective surface layer.

Figure 7.10 shows three STM scans with subsequently higher magnification of terraces present

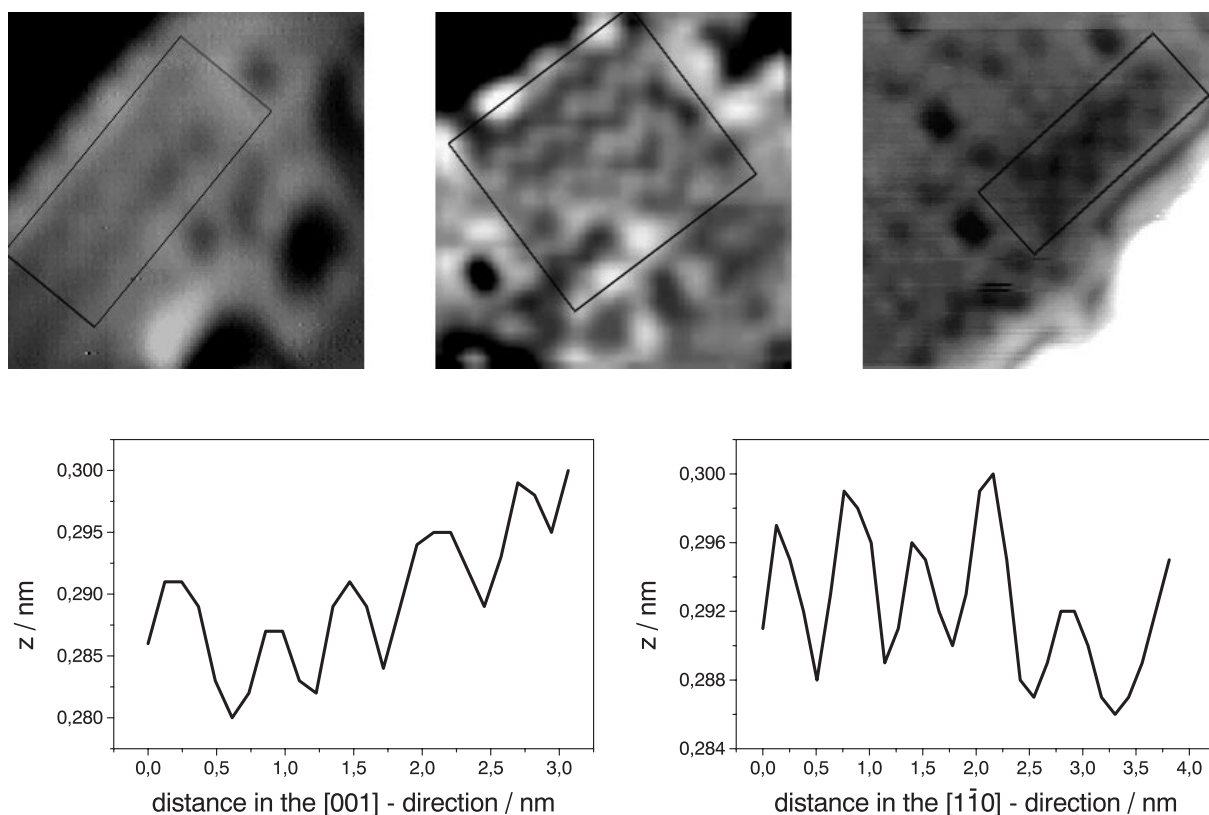


Figure 7.11: $50 \times 50 \text{ \AA}^2$ areas at three different positions. The 2×1 structure is highlighted by a rectangle, respectively. In the lower figure, lineprofiles in the $[001]$ and $[1\bar{1}0]$ direction are shown, each taken on the STM image in the middle of the upper figure.

on 1×1 reconstructed surfaces, as judged by LEED. These images give an impression of the high defect density that could be observed on as prepared surfaces, which is very impressive when comparing them to the STM images of the 4×1 reconstructed surface which has been prepared by annealing at lower temperature (compare figure 7.9). The broad 2×1 LEED feature that appears in the high-temperature 1×1 LEED patterns (see figure 7.2 C) is consistent with very small areas that could be imaged by STM (see figure 7.11).

STM Images of 2×1 Structures

Indeed, ordered structures on terraces of as-prepared surfaces turned out to exhibit not a 1×1 surface unit cell but a cell size consistent with a 2×1 reconstruction ($6.4 \times 6.8 \text{ \AA}^2$). The line

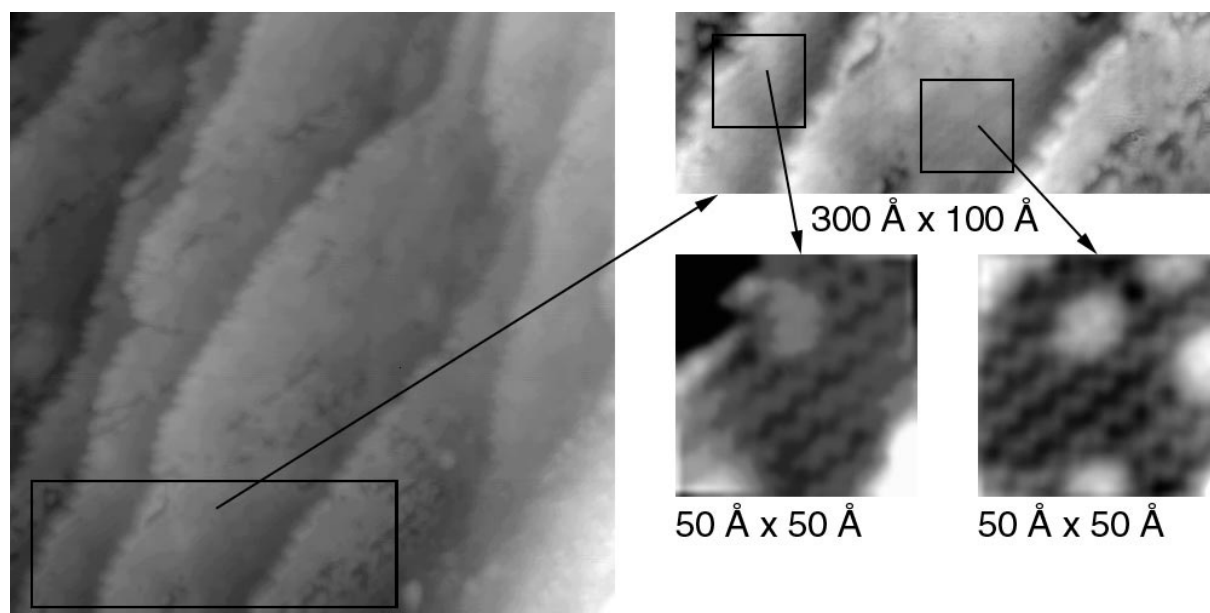


Figure 7.12: $50 \times 50 \text{ nm}^2$ scan, with magnifications shown on the right hand side of this figure.

profiles shown in figure 7.11 show a periodic variation in the $[001]$ and $[1\bar{1}0]$ which indicates such a surface unit cell of $6.4 \times 6.8 \text{ \AA}^2$. This structure can be easily explained by zigzag rows of surface oxygens in the $[001]$ -direction instead of the double rows that should be expected on reduced 1×1 reconstructed $\text{SnO}_2(110)$ surfaces. The model proposed is shown, in comparison to the model for the 4×1 reconstruction, in figure 7.13.

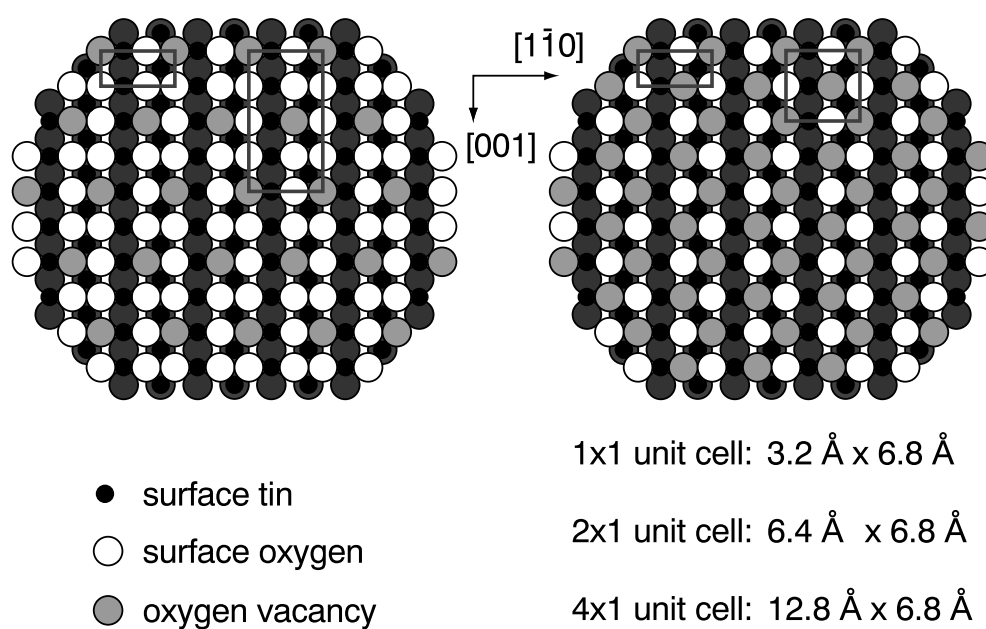


Figure 7.13: Comparison between the proposed models for a 4×1 and 2×1 reconstructed $\text{SnO}_2(110)$ surface.

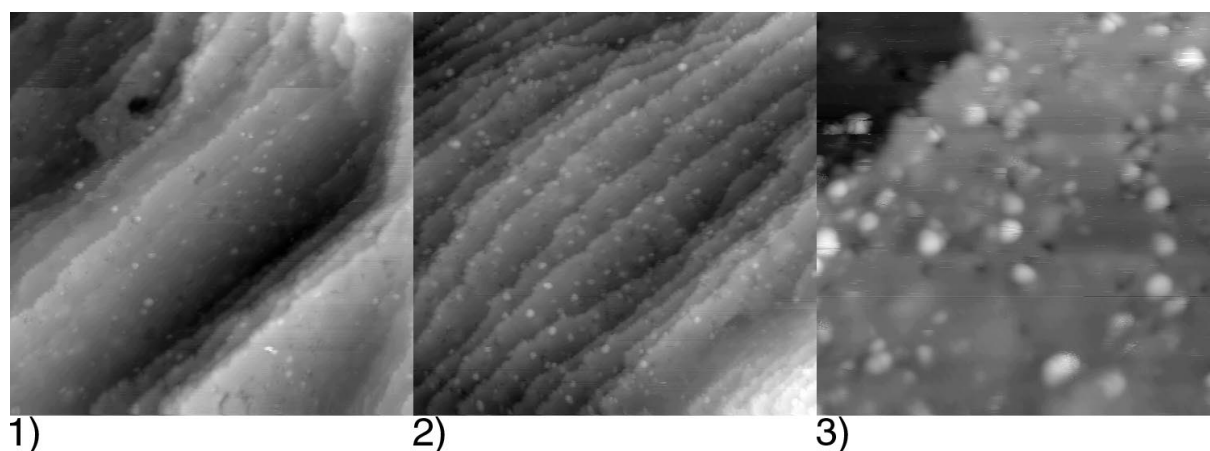


Figure 7.14: 4×1 surface after deposition of Pd for 1s (image 1) and 4s (image 2) both images $100 \times 100 \text{ nm}^2$. The right picture shows a $20 \times 20 \text{ nm}^2$ area with clusters between 1 and 3 nm in diameter

7.2.3 Pd-Clusters on $\text{SnO}_2(110)-4 \times 1$ imaged by STM

Pd was deposited from a Pd-loaded evaporator on highly ordered 4×1 reconstructed $\text{SnO}_2(110)$ -surfaces. The very low coverages were obtained by opening the shutter for only 4 s.

Figure 7.14 shows small Pd-clusters of up to 3 nm in diameter randomly spread all over the terraces. After short annealing for 10min to 600°C , i.e. to a temperature at which the 4×1 reconstruction is still stable, the Pd was converted to larger clusters up to 9 nm (see 7.15) decorating the step edges.

The clusters only stick weakly to the surface and could be moved by adjusting the tip closer to the sample. The images in figure 7.15 display a sequence of three images taken one after another in the same region with two large clusters moved by the tip at highest tunneling current.

The observation of weakly sticking clusters indicate that there has no reaction taken place between the $\text{SnO}_2(110)$ surface and the evaporated palladium. Furthermore, the clusters are mobile enough on the surface to form larger clusters when annealing the surface to 600°C . As on stoichiometric, i.e. oxidized surfaces an oxidation at much lower temperature could be observed, the weak interaction between surface and palladium may be attributed to the reduced and therefore less reactive surface.

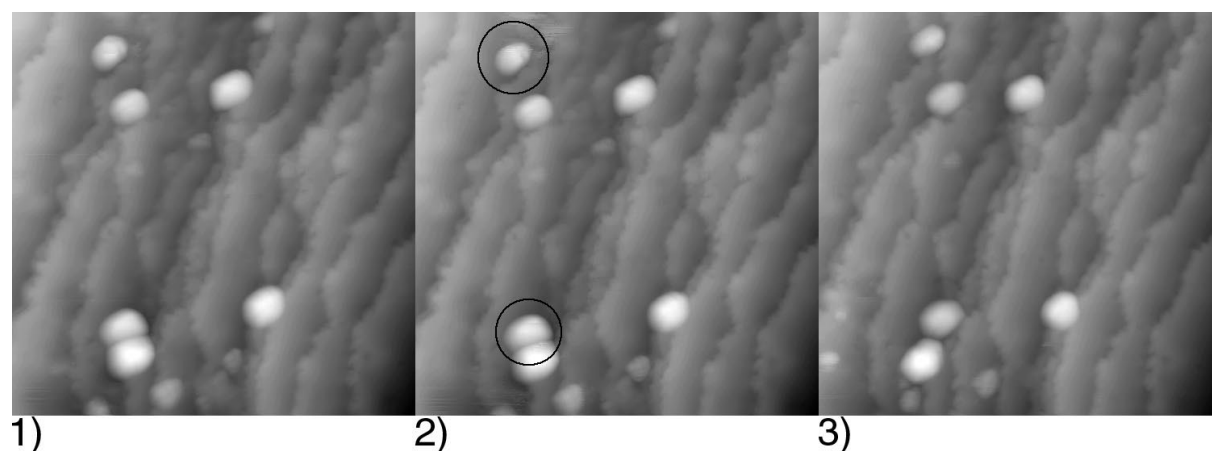


Figure 7.15: $50 \times 50 \text{ nm}^2$ scans of the same area taken one after another. In image 1) and 2) a tunneling current of 0.1 nA in image 3) of 1.0 nA was applied. The moved clusters are marked in image 2).

7.3 Discussion

The first point for discussion is the nature of the high-temperature 1×1 reconstructed surface, since it is the essential starting point for further discussion of the reconstruction process. So far it has been generally assumed that this LEED pattern results from truly 1×1 reconstructed reduced surfaces, without remaining bridging oxygen rows and with a defect density of in-plane oxygen vacancies on the 1×1 terraces dependent on annealing temperature.

In contrast to this assumption, real-space microscopy indicates a very high defect density without any evidence for larger areas of 1×1 ordered surface structures (see figure 7.10). The only ordered surface structure that could be identified are zigzag rows of in-plane oxygen (see figures 7.11-7.12) which are present on the terraces only locally. When examining the corresponding LEED pattern, there is indeed only some very diffuse intensity visible around the 2×1 position in figure 7.2 C and D. This is an indication that this structure is not stable in a way which implies ordering on complete terraces, but in very localized regions within them. There is indeed no contradiction to the dominating 1×1 LEED pattern since such a pattern can be easily explained by the contribution of underlying atomic layers which are well-ordered at this annealing temperature and accessible to the method because of its information depth of several Ångströms.

Accordingly, the high-temperature 1×1 reconstruction is not likely to be a stable surface termination but an intermediate state, open to be either annealed to the 1×2 reconstruction at higher annealing temperature or back to a 4×1 reconstructed surface by lowering the annealing temperature. In fact, a similar attempt to remove the 1×2 LEED pattern just by subsequently annealing to lower temperatures over a period of several days failed, giving additional evidence for the intermediate character of the 1×1 reconstruction in contrast to the 4×1 and 1×2 reconstruction.

When comparing the results of STM and XPS measurements to each other, a new mechanism for the reconstruction process can be proposed. Another observation in this context is that it was not possible to reduce the $\text{SnO}_2(110)$ crystals just by heating at temperatures around 1200 K in UHV in order to increase their conductivity, as it is for example possible for TiO_2 . That means it can be assumed that oxygen outdiffusion is not the dominating process during the reconstruction of the surface, especially at relatively low temperature below 1000 K. Together with the observation by STM of increasing defect density on the terraces at the conversion temperature from the 4×1 to the 1×1 reconstruction and the fact that to our knowledge in no publication metallic tin could be found on as-prepared surfaces, a reconstruction model based upon desorption of surface species is most likely. That means that the reconstruction process at least at temperatures around the $4 \times 1/1 \times 1$ conversion temperature is not driven by out-diffusion of oxygen or tin from the bulk but by desorption of surface oxygen and subsequent desorption of reduced tin.

This is also supported by the observation that XPS O/Sn ratios are very similar to each other for both investigated surface treatments, which leads to the assumption that gently sputtered surfaces (with still a 1×1 reconstruction left) are comparable to a high-temperature annealed 1×1 reconstructed surface when regarding the stoichiometry. The strong deviation in the core-level shifts may be due to a two-dimensional disorder in the lattice induced by sputtering.

Nevertheless, this model does not hold when trying to explain the 1×2 reconstruction with its increased oxygen amount which was observed by Cox et al. [27] as an increase in the ISS (Ion Surface Scattering) O/Sn ratio at very high temperature and by Pang et al. [117] with real space STM and NC-AFM imaging. A possible explanation would be that the surface is stabilized at very high annealing temperature of 1100-1200 K by an increased out-diffusion of oxygen.

Chapter 8

Electronic Structure and Chemical Composition

The electronic and chemical properties of SnO₂ surfaces were mainly revealed by photoelectron spectroscopy. For a fast characterization of the impurity level of the gas sensors, SIMS was applied in Static SIMS mode and AES was only used for preparation control, preceding the STM experiments presented in the previous chapter.

Since the chemical properties of a given material are determined by their valence electrons, it is of essential importance to get information about the valence band structure and about the atomic levels which are contributing to it. Resonant photoemission proved to be a well-suited method to investigate the valence band density of states and to discriminate the contributions of different elements by taking advantage of resonance effects. These resonance effects can have various origins. Resonant enhancement of the photoemission signal can occur for example when the atomic subshell photoionization cross-section of a certain element is maximized [191], or when states in the conduction band are filled by electronic transitions (see section 3.1.1). The resonance occurring when an atomic level is interacting with a continuum has been described by Fano [44] and can be described with the famous Fano line-shape which actually has often been observed in ResPES experiments. This type of resonance has been of particular use in the study of the electronic structure of rare-earth and transition metal compounds [2, 3] (see section 3.1.1).

For evaluating resonance photoemission spectra a number of methods have been developed. On the data presented in this thesis, CIS curves, which show the dependency of the density of states at a given binding energy on the photon energy, difference spectra between resonance and off-resonance valence band spectra and factor analysis were applied. The latter method is a data reduction method, able to automatically sort out main independent contributions to the valence band density of states which are affected by changing the photon energy (see section 6.1).

The data evaluation mentioned above was applied on the resonant photoemission data of SnO₂(110) and of gas sensors based upon nanocrystalline SnO₂ which is presented in the following. Difference spectra were only calculated for the same type of samples, i.e. there were no difference spectra calculated between single crystal spectra and sensor spectra. The reason is that the initial preparation, on the one hand well-defined and reduced surfaces in the case of SnO₂(110) and on the other hand untreated and therefore contaminated surfaces in the case of the sensors, is very different and would therefore lead to strong deviations just because of the sample history.

8.1 SnO₂(110)

In the following, measurements on the bare SnO₂(110) surface are discussed. Clean surfaces were prepared by sputtering and annealing under UHV conditions resulting in oxygen-deficient surfaces.

Laboratory source measurements were performed on the equipment described in section 5.1. Synchrotron radiation photoelectron spectra were recorded at Beamline I311 at MAXlab, Lund (see section 5.3 and Ref. [177]).

8.1.1 SRPES Core-Level Spectroscopy

Because of its short life-time but mainly because of phonon interaction, core-level photoemission signals of SnO₂ are broadened so that it is not possible to take advantage of the high resolution photoemission capability of today's third generation synchrotron radiation sources. Figure 8.1

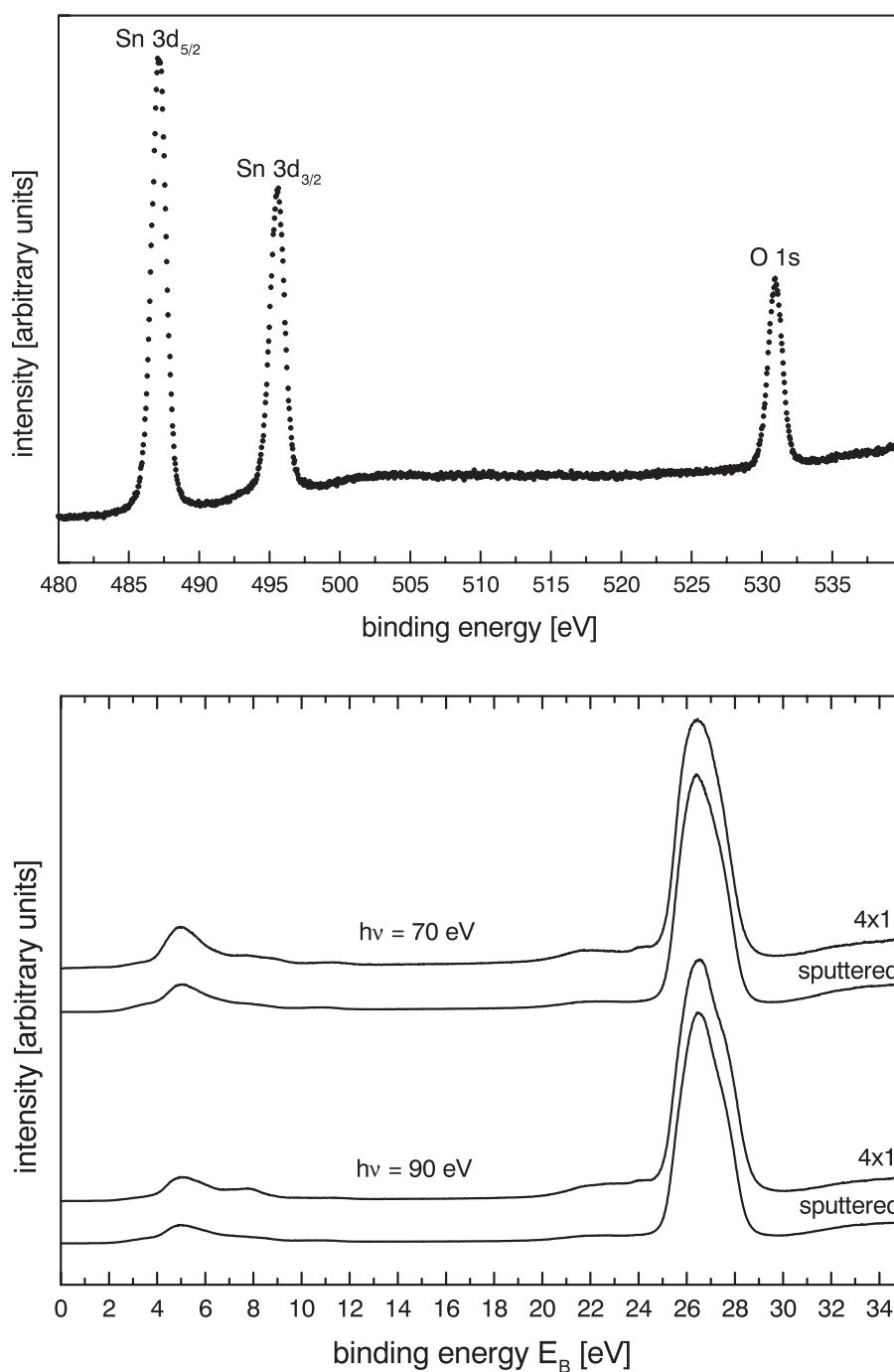


Figure 8.1: Upper figure: EDC of the Sn 3d and O 1s core-levels of the freshly sputtered SnO₂(110) surface recorded at a photon energy of $h\nu = 630$ eV. Lower figure: EDCs of the Sn 4d and valence band region of 4×1 reconstructed and sputtered SnO₂(110) at two different photon energies.

shows the Sn 3*d* and O 1*s* core-levels recorded at an actual instrumental resolution around 0.1 eV. The broadness of ≈ 1.1 eV is therefore due to the broadening of the electronic states and not restricted by the experimental conditions (see section 6.2).

This is also the case for the Sn 4*d* core-levels shown in the lower figure. This very poorly resolved doublet can be fitted to Voigt peaks with a width around 1.4 eV. The shape differs between sputtered and ordered surfaces and also a variation in peak shape is visible when changing the photon energy. The peak shape for both surfaces is better defined at $h\nu = 90$ eV resulting from the deeper sampling depth at this photon energy. The undefined shape at $h\nu = 70$ eV reflects the stronger contribution of the surface states which are not fittable by a single doublet anymore, but seem to have a significant contribution from a second doublet probably due to Sn²⁺ present on the surface.

8.1.2 ResPES on SnO₂(110)-4×1 and Sputtered SnO₂(110)

The 4×1 reconstructed and the freshly sputtered surface of SnO₂(110) were investigated by resonant photoemission. Valence band spectra of the 4×1 reconstructed and freshly sputtered surface were recorded in a photon energy range between 60 eV and 130 eV in steps of 5 eV, leading to a high discrimination between these two surface terminations. For discussing these resonances, CIS curves, difference spectra and principal factors were extracted from the spectra and are discussed in the following according to the band structure of the material and the core-level positions of tin.

Resonant photoemission spectra in a photon energy range between 30 eV and 50 eV in steps of 2.5 eV were recorded on the 4×1 reconstructed surface to get comparative data to the ResPES study of Themlin et al. [160] in which only the sputtered surface was treated. The reason for this restriction was the emphasis of this study on the band gap states, which are strongest in the case of freshly sputtered SnO₂(110). Unfortunately, there was no time at the Beamline to repeat the measurements of Themlin et al. on the sputtered surface. The corresponding raw spectra recorded on the 4×1 reconstructed surface are shown in figure 8.2 and the CIS-curves in figure 8.3. In contrast to the results of Themlin et al. there is no resonance at 35 eV visible in the

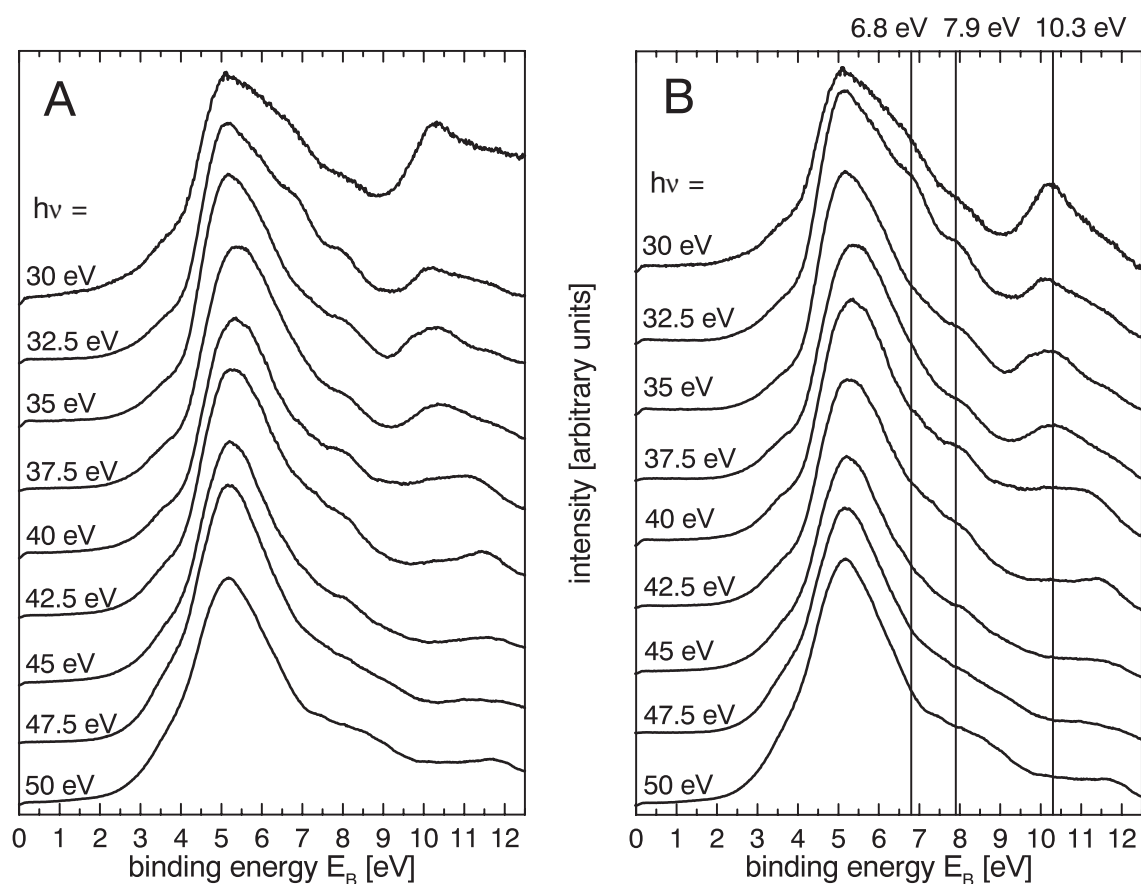


Figure 8.2: Resonant photoemission spectra of the valence band region of SnO₂(110)-4×1 taken every 2.5 eV for photon energies of 30 eV-50 eV. Figure A shows the raw data and figure B background subtracted data. For background subtraction an exponential decay of the secondary electron background, most evident at lower photon energy, was assumed. All spectra were taken in normal emission mode with the sample grounded.

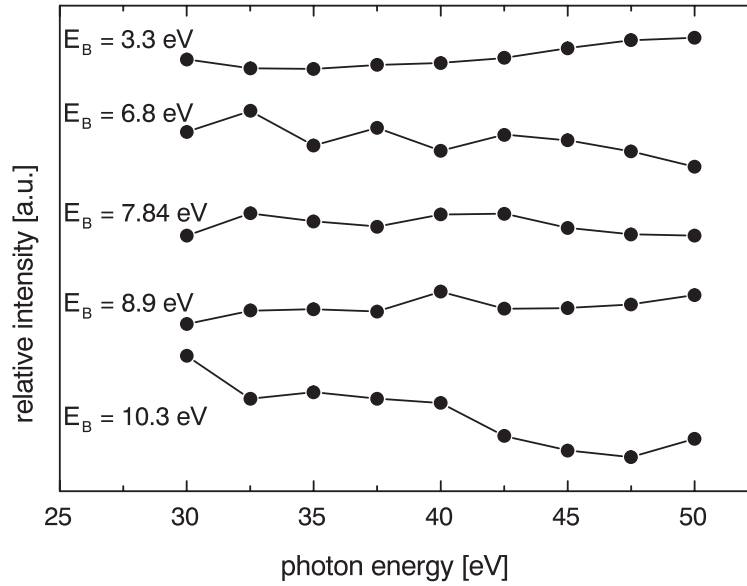


Figure 8.3: Constant initial state (CIS) curves extracted from figure 8.2. The tracked electron binding energies are either energies of significant dispersion or relevant for a comparative discussion with the ResPES data for photon energies of 60-130 eV shown in figure 8.4 and 8.5. The plotted intensity is arbitrary, but vertically the same for all curves.

CIS-curves of the band gap states at $E_B = 3.3$ eV which is most probably due to the much lower density of states in the band gap on the 4×1 reconstructed surface compared to the sputtered one.

The 4×1 surface was prepared by annealing a 1×1 high-temperature surface at lower temperature, as already described in section 7.1. The annealing time of 36 h should have been sufficiently long to end up with an almost perfect surface termination. The ResPES data for the 4×1 reconstructed and the freshly sputtered surfaces are shown in figures 8.4 A and B respectively. The spectra are referenced to the Fermi level, which was accessible either by a metal in electrical contact with the sample or by the Fermi level of the SnO_2 sample itself.

The features of the valence band structure from which CIS curves are generated, see figure 8.5, are marked by letters. 'A' is related to the band gap states ($E_B = 3.3$ eV) which are typical for reduced SnO_2 . Characters 'B', 'C' and 'D' (at 7.84, 8.2 and 8.9 eV binding energy respectively) mark features in the Sn $5p/O$ $2s$ part of the valence band, which are strongly dispersing. The intensity of the CIS curves is normalized to the integral intensity over the valence band region

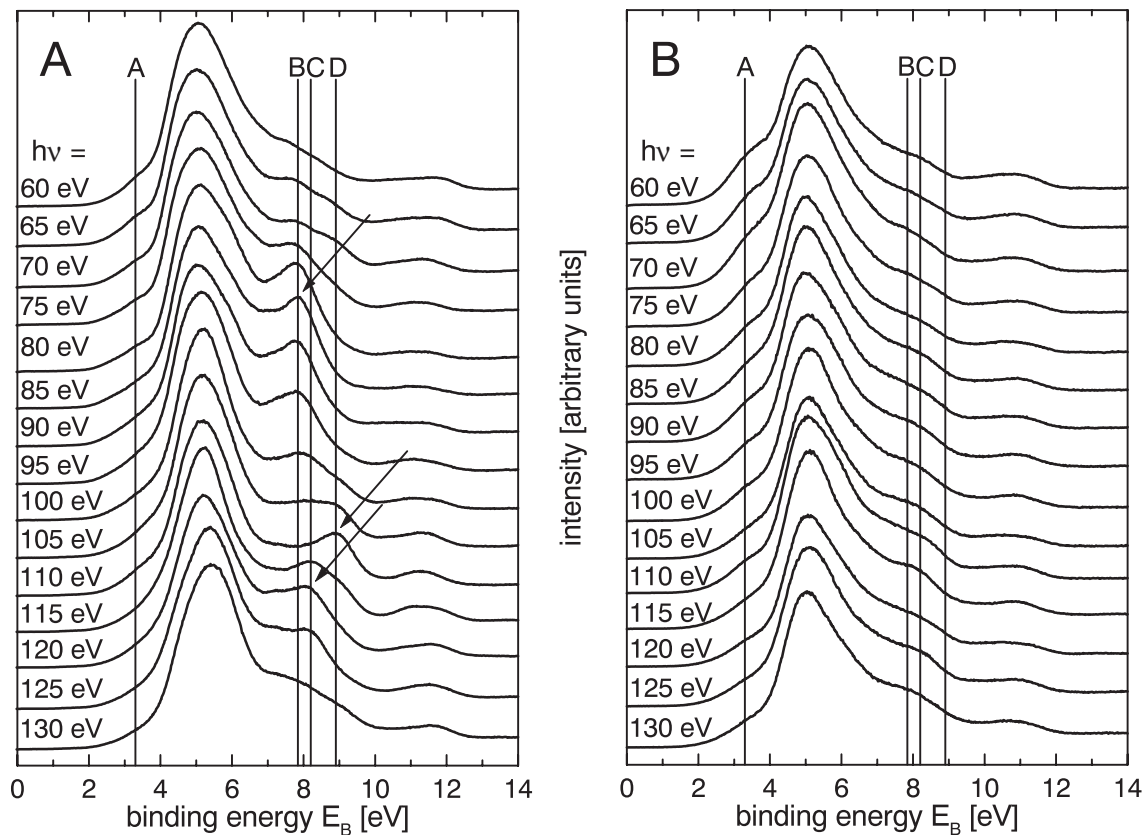


Figure 8.4: Valence band spectra of SnO₂(110)-4×1 (figure A) and freshly sputtered SnO₂(110) (figure B) taken every 5 eV for photon energies of 60-130 eV. Features discussed in the text are marked with characters. Spectra were taken in normal emission mode with the sample grounded.

($0 \text{ eV} \leq E_B \leq 14 \text{ eV}$) at each photon energy. For an interpretation of the spectra, a more detailed view into the band structure and the core-level positions of SnO₂ is necessary. For this reason figure 8.8 summarizes the contribution of the atomic levels to the valence band density of states and the energetic positions of Sn 4*s*, 4*p* and 4*d* core-levels which are accessible in the discussed photon energy range [110, 160]. Furthermore, factor analysis (FA) (see section 6.1) and the calculation of difference spectra were applied to identify structures in the valence band which are affected by changes in the photon energy. The results of this factor analysis are presented, together with difference spectra between resonance and off-resonance valence band spectra, in figure 8.6.

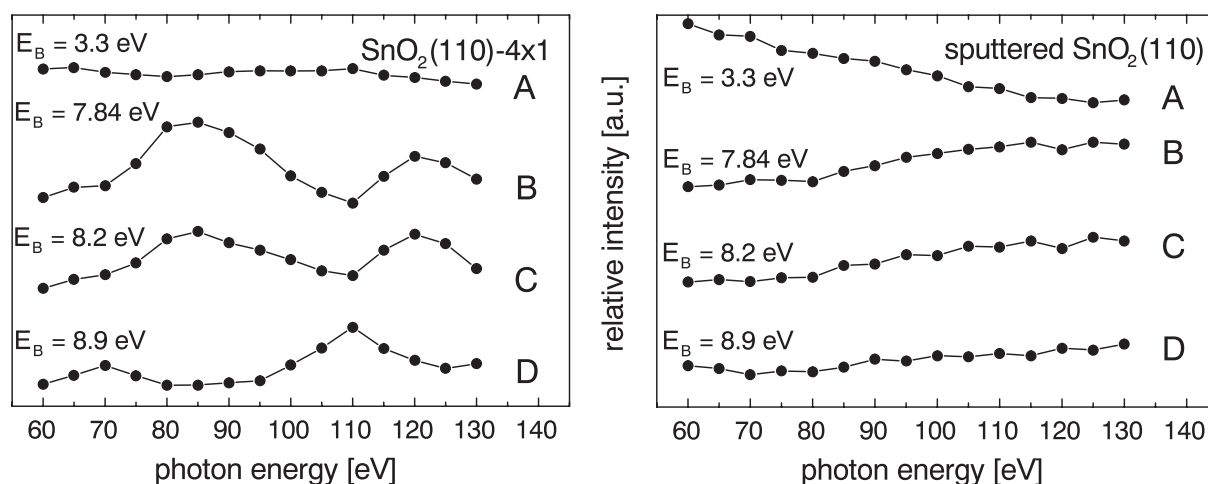


Figure 8.5: Constant initial state (CIS) curves extracted from figure 8.4 A and B. The tracked features are marked by the same letter as in figure 8.4 and the intensities are related to the integral intensity of the valence band region for each spectrum. The vertical intensity is arbitrary but the same for all plotted CIS curves in each figure.

Results and Data Evaluation

For both surface treatments the signal from the band gap states, marked by the letter 'A' in figures 8.4 and 8.5, decays slightly when the photon energy is increased. This decay of the photoemission signal at higher photon energy is consistent with the decay of the photoionization cross-sections of all possibly involved oxygen and tin levels – Sn 5s, Sn 5p, O 2p – and can therefore not be used for a discrimination of the oxygen and tin contributions to the valence band density of states (see section 3.1.1). There are three strong features in the valence band spectra of the 4×1 reconstructed surface, marked by the letters 'B', 'C' and 'D', which show an enhancement at 85 eV, 120 eV and 110 eV respectively. This observation results in two main questions to be answered. First, the structure – or possibly the structures – which show a dependency towards the photon energy have to be identified and second, the discrepancy between the behavior of the ordered, 4×1 reconstructed, and the disordered, sputtered surface has to be explained.

A standard method for data reduction and structure determination of a given dataset, factor

analysis (FA) has been applied to isolate characteristic structures from both sets of valence band spectra. The factors extracted from both sets of spectra are on the one hand a factor reflecting more or less the shape of the valence band itself and on the other hand a factor characteristic for the dispersing behavior. The factor values, that means the two datasets determined by FA with which each valence band spectrum could be reconstructed in a very good approximation, are plotted together with the difference spectra in figures 8.6 A and B. In figures 8.6 C and D the factor loadings, i.e. the value with which every factor has to be multiplied to compose the corresponding valence band spectra, are plotted with the related factor in the background.

The difference spectra were generated by first normalizing the spectra to be subtracted to equal intensity in the valence band maximum and then directly subtracting them from each other. Shifts in the valence band maximum when varying the photon energy correlate to a variation in shape depending on the photon energy and are therefore probably due to changes in the cross-section. Since in all cases only spectra recorded on the same surface are subtracted, shifts are not likely to be due to a band bending. Figure 8.6 A shows spectra generated by subtracting a spectrum recorded at $h\nu = 100$ eV on the 4×1 reconstructed surface from spectra at the resonance photon energies 85 eV, 110 eV and 120 eV. Figure 8.6 B shows difference spectra obtained by the same procedure on the sputtered surface.

Discussion of the Results

The factor analysis applied on both surface terminations, the 4×1 reconstructed and the sputtered surface, only results in two significant factors for each termination. The first factor models the shape of the valence band, whereas the second factor is due to a systematic modulation of the valence band shape as a function of the photon energy.

There are striking similarities when comparing – for the 4×1 reconstructed surface – the CIS-curves and difference spectra on the one hand and the results of the factor analysis on the other hand. The factor loadings of figure 8.6 C correspond very well to the CIS curves of the 4×1 reconstructed surface in figure 8.5. The shape of the CIS-curves 'B' and 'C' are qualitatively identical with the factor loadings plot of the second factor in figure 8.6 C. But also the CIS-

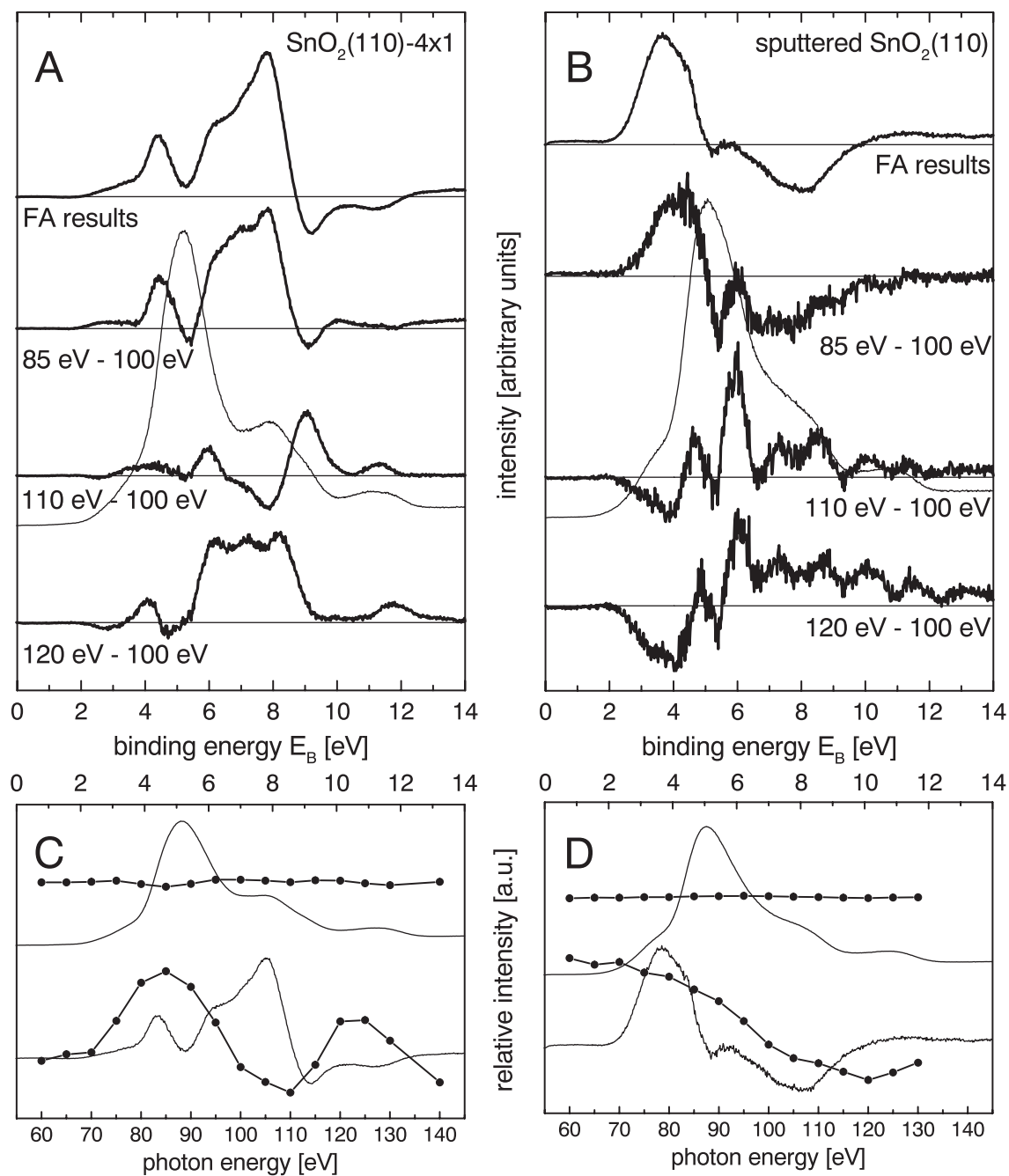


Figure 8.6: Difference spectra and principal factors extracted from the valence band spectra (see 8.4) of $\text{SnO}_2(110)-4 \times 1$ and sputtered SnO_2 (figures A and B, respectively). The factor loadings, together with the corresponding factor plotted in the background, are shown in figures C and D.

curve 'D' can be explained by comparing it to the inverse factor loadings plot of the same factor. The remaining CIS-curve 'A' of the band gap states at 3.3 eV can just be explained by the monotonous decrease of the atomic subshell photoionization cross section of Sn 5s and 5p levels in the related photon energy range and is, because of its much lower intensity, not considered by the factor analysis.

The results of the sputtered surface can be discussed in a very similar way. Since no strong resonances occur in this set of spectra, the factor analysis sorts out the monotonous decrease of the band gap states as the second factor. This decrease in the factor loadings of the second factor is consistent with the decrease in the atomic subshell photoionization cross sections of any involved state, i.e. the Sn 5s, 5p and O 2p electronic levels, and therefore offers no possibility for a discrimination between them.

The difference spectra of figure 8.6 A and B and the factor values of the second factor, as determined by factor analysis for each surface termination, show a compatible trend. The difference spectra of the 4×1 reconstructed surface in figure 8.6 A can be modelled just by relating the factor values of the second factor in figure 8.6 A to the corresponding factor loadings in 8.6 C at 85 eV, 110 eV and 120 eV. The difference spectra and FA results of the sputtered surface show much lower intensity – as obvious when considering the noise level of the curves – and have their strongest feature in the band gap which is modelled by the results of the factor analysis as well.

Discussion of the observed Resonances

The band gap states which are typical for reduced SnO₂ surfaces and have been attributed to Sn 5s states by the ResPES study of Themlin et al. [160], show a similar trend in the difference spectra for both surface terminations. This can be most easily seen in the monotonous decrease of the CIS-curves 'A' in figure 8.5 for both, the 4×1 reconstructed and the sputtered surface. This leads, in figure 8.6 B, to an enhancement in the band gap states for the first difference spectrum with an decrease in intensity and finally an inversion towards the difference spectra '120 eV-100 eV'. Since this is the only systematic variance in the spectra of the sputtered surface that

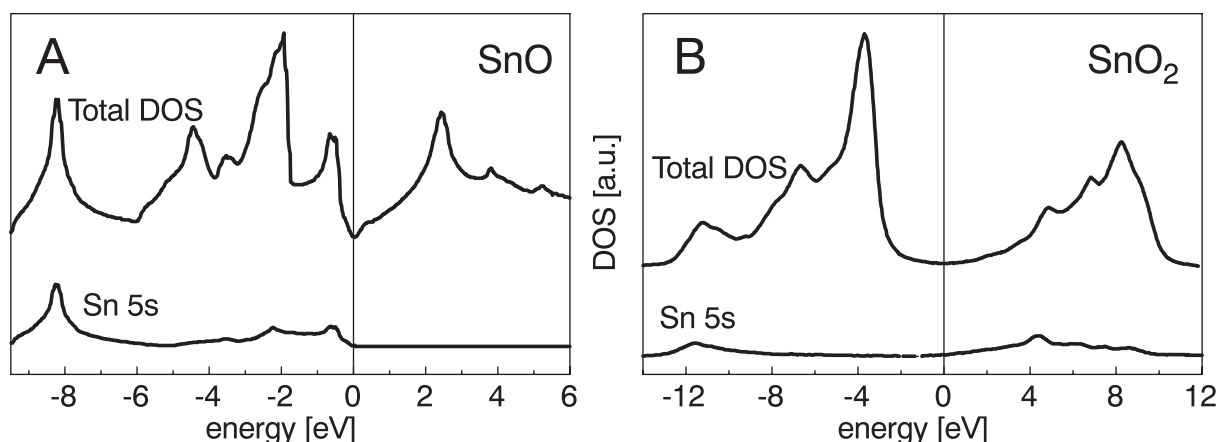


Figure 8.7: DOS curves calculated for bulk SnO [86] and SnO₂ [110]. The energy scale for both curves is related to the Fermi level and the DOS-curves in figure B are calculated with a 0.3 eV Lorentzian broadening. The upper curves show the total density of states and the lower curves the partial density of states attributed to Sn 5s levels.

could be observed in the considered photon energy range of 60 eV-130 eV, the emphasis of the further discussion is on the ordered, 4×1 reconstructed surface.

The shape of the resonance, as shown in figures 8.5 and 8.6 C, with its maximum at $h\nu = 85$ eV shows a tail towards higher photon energies, which would indicate a Fano-type lineshape and therefore a configuration interaction between filled states and a continuum of unfilled states. Such a typical Fano lineshape actually refers to photoabsorption. Since in this case the increase in photoemission intensity is considered, a lineshape similar to the one calculated by Yafet et al. [183] for the Auger current emitted after Fano-type resonances (see figure 3.7) can be expected.

Because of the broadness of the resonance a curve-fit is not likely to be successful. Additionally, the physical system under consideration is far from being the 'ideal' system discussed by Fano [44]. There is no sharp state for a starting point and no homogeneous continuum available as a final state for SnO₂. The involved states may be on the one hand the Sn 4p core-level and on the other hand the Sn 5s derived states in the conduction band. The transition from the Sn 4p core-level to the Sn 5s states is dipole-allowed and the Sn 5s states of the conduction band are situated at the Fermi level in DOS calculations of bulk SnO₂ (see figure 8.7 B). The maximum of

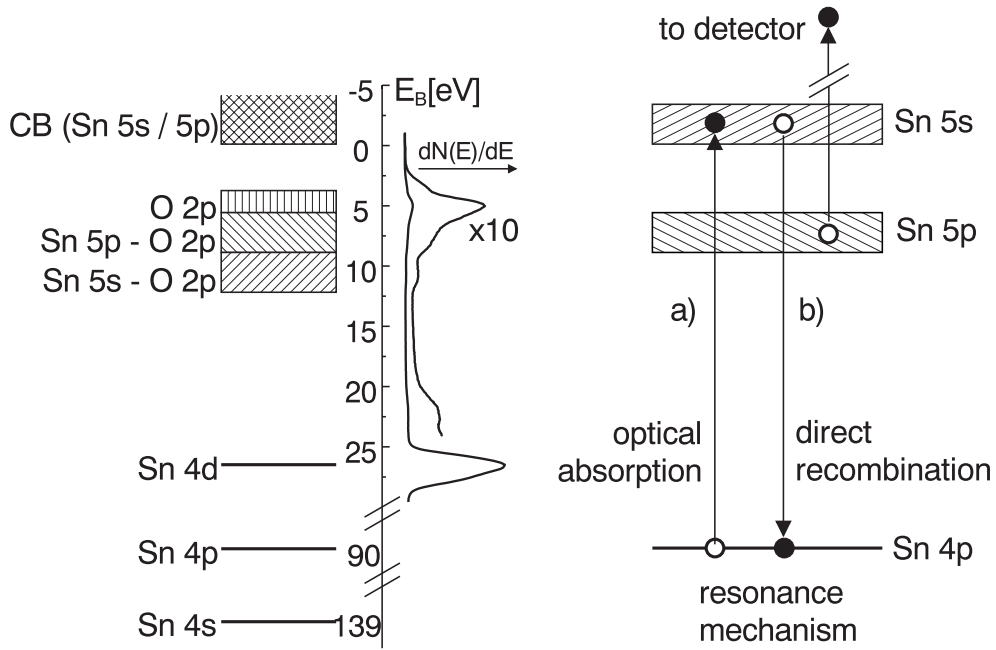
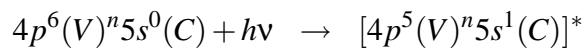


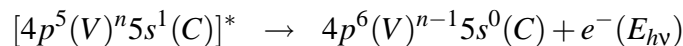
Figure 8.8: On the left hand side, the schematic energy level diagram of the CB-, VB- region and the Sn core-levels is shown [110, 160]. The spectrum of the valence band and Sn 4d region was recorded at $h\nu = 90$ eV. The resonance mechanism proposed on the right hand side of this figure is based upon the ResPES data of 4×1 reconstructed and sputtered SnO₂(110) (see figure 8.4).

the Sn 4p core-level is at a binding energy of 90 eV, i.e. there is a discrepancy to the maximum of the resonance of $h\nu = 5$ eV. This can be explained by the very broad shape of this peak with a FWHM ≈ 20 eV.

This resonance process can now be described according to the resonance process observed by Themlin et al. (see section 3.1.1). Starting with photoabsorption:

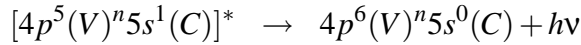


Autoionization is not likely to happen, since the states of the conduction band near the Fermi level are still below the vacuum level and trapped by the surface potential. C denotes states in the conduction band, V states in the valence band and $*$ the excited state with a core-hole. Direct recombination by emitting a valence band electron

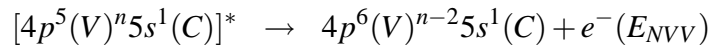


would now result in the same final state and the same kinetic energy of the emitted electron as direct photoemission. That means direct photoemission from the valence band states interferes with the direct recombination and leads to an increase in the detected electron current.

Another process that might happen is fluorescence:



or an Auger decay to fill the core-hole, for example a NVV Auger process:



There is still one question to answer, namely the lack of resonance on the sputtered surface. When considering figure 8.7, it can be easily seen that Sn 5s states are only present in the conduction band for SnO₂, but not for SnO. That means one possible explanation would be that the Sn 5s surface states are pushed down into the valence band by the much higher defect density on the sputtered surface, whereas on the 4×1 reconstructed surface only a small portion is affected in this way. Such an effect would also be reflected by the much higher emission from the band gap states on the sputtered surface compared to the ordered one.

8.2 Nanocrystalline SnO₂

Thick film gas sensors based upon doped and undoped nanocrystalline tin dioxide, see section 4.2, were investigated by photoelectron spectroscopy and SIMS. In order to ensure comparability to gas test measurements under ambient air conditions (see figure 4.4), no UHV preparation like sputtering or annealing, was applied. Therefore sufficiently clean surfaces were required for surface sensitive spectroscopy. The sensors investigated, doped and undoped devices sintered at 450°C fit these needs and show sufficiently low contamination levels to record valence band spectra down to photon energies of $h\nu = 21.22$ eV. The concentration of the two dopants discussed in the following, Pd and Pt, are introduced to the SnO₂ in weight percent, i.e. at the same nominal concentration level almost two times more palladium ($m = 106.42$ u) atoms compared to platinum ($m = 195.08$ u) are introduced to the material.

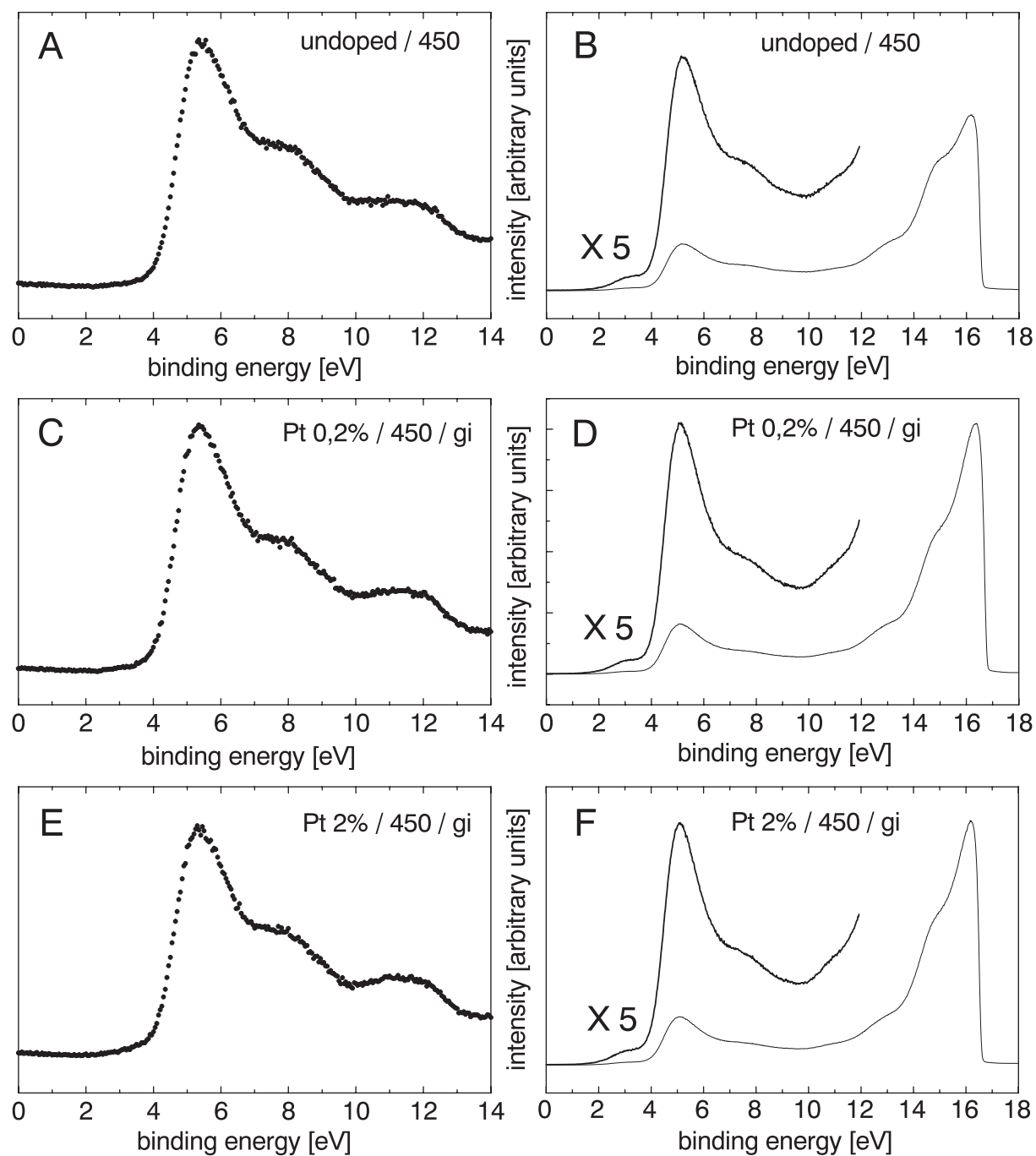


Figure 8.9: UPS He II (left) and He I (right) spectra of undoped and Pt-doped gas sensors. Spectra were recorded at -10 V BIAS at the sample and referenced to the Fermi level of a metal in electrical contact with the sample.

Although photoelectron spectroscopy has a non-negligible information depth, it can be assumed that surface effects are predominant in the spectra. With a mean grain size of around 15 nm of the used nanocrystalline SnO₂ (figure 4.3), the IMFP in the applied photon energy range of 20 eV-120 eV is short enough to not average over whole grains.

Laboratory source UPS results are presented in section 8.2.1, SRPES valence band spectra and the SIMS spectra in section 8.2.2.

8.2.1 Laboratory Source UPS Results

The prerequisite for any systematic investigation of the electronic structure of SnO₂ gas sensors based upon nanocrystalline SnO₂ is the reproducibility of these devices towards the photoemission signal of the valence band region. For this reason, comparative measurements on sensors of the same type but with different dopants were undertaken and the reproducibility of the obtained spectra could be well established. Even for sensors with different dopants or dopant concentrations only little changes in the valence band shape could be detected. This may have two reasons: On the one hand, the laboratory source UPS photon sources only offer photon energies which favor the excitation of electrons bound in oxygen states and on the other hand, the surface sensitivity in this photon energy range is much higher than in the XPS photon energy range. The first reason easily can be supported by comparing the photoionization cross sections of oxygen and tin to each other as shown in table 3.2. The second assumption actually cannot be solved just by photoelectron spectroscopy.

The He II spectra with an according He I spectra, which are also showing the onset of inelastically scattered secondary electrons, are displayed in figure 8.9. The signal in the band gap, obvious in the He I spectra, is due to He I_β excitation, since the used ultraviolet light source is not monochromatic. In order to investigate the band gap, He II spectra are therefore much more favorable as the main satellite line is at around 7.5 eV higher photon energy and not affecting the photoemission signal from the band gap states.

Nevertheless, small differences can be observed when taking difference spectra between undoped and doped devices. Figure 8.10 B shows difference spectra taken from the measurements

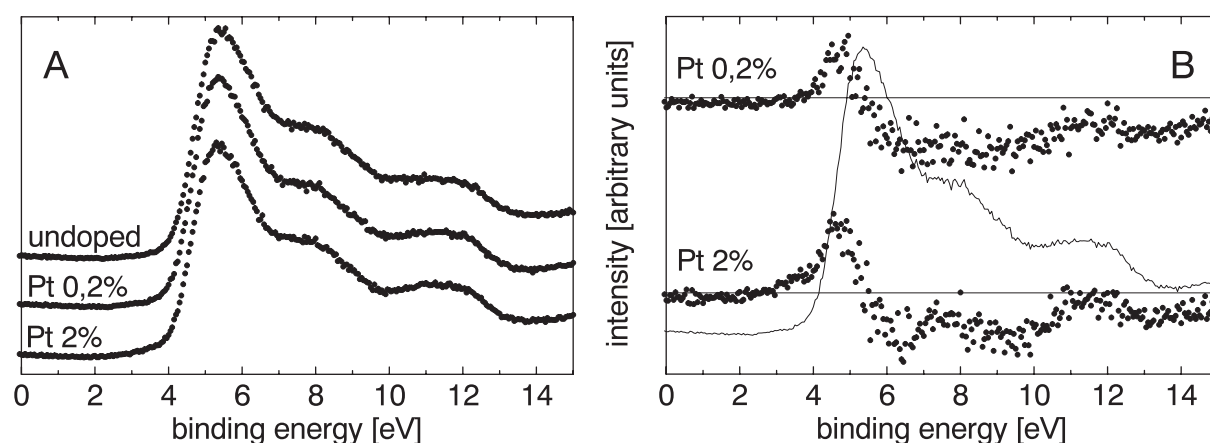


Figure 8.10: UPS He II spectra of undoped and Pt-doped SnO₂ gas sensors (figure A). Difference spectra shown in figure B were generated by subtracting the UPS spectrum of the undoped sensors from the two other spectra respectively.

shown in figure 8.10 A. Before subtracting the spectra from each other, the intensities were normalized to the valence band maximum, i.e. the signal from the O 2*p* states. A band bending is not observable and therefore the energy scale needs no recalibration.

The scale of the intensity is the same for both difference spectra in 8.10 B, i.e. the photoelectron intensity in the band gap (around $E_B = 3.3$ eV), which arises from the doping, is not scaling with the doping amount.

8.2.2 ResPES on doped and undoped Gas Sensors

The electronic structure of undoped, Pd-doped (2% wt.) and Pt-doped (2% wt.) SnO₂ gas sensors was investigated by ResPES in a comparable photon energy range to the ResPES data of SnO₂(110) discussed in section 8.1.2. The sensors were mounted on the manipulator where they stayed during the bakeout of the preparation chamber. Therefore a slight reduction of the surface was unavoidable due to the baking temperature up to 190°C which is most evident when looking at the photoemission signal of the band gap region with its higher density of occupied states compared to the spectra previously discussed in section 8.2.1. No further UHV treatment, like sputtering or annealing to remove contaminations, was applied in order to ensure comparability

to sensors of the same type investigated in gas test measurements under ambient air conditions and laboratory source UPS.

In spite of the apparent bakeout damage of the sensors, a comparative discussion between the investigated sensors is valid, since all three sensors were treated exactly in the same way. In order to clarify differences in the photoemission signal, difference spectra and CIS curves were generated from the raw data. Furthermore, SIMS spectra were taken to get an overview of the impurities present on the sensor's surfaces after carrying out photoemission measurements.

SRPES Raw Data

Valence band spectra were taken under comparable conditions to the ResPES data of the single crystal samples discussed in section 8.1.2. That means detection of photoelectrons with the analyzer perpendicular to the sample, very high photon flux, an instrumental resolution better 30 meV and the sample grounded.

The ResPES data recorded in a photon energy range of 50-120 eV is shown in figure 8.11 A-C for the undoped, Pd-doped and Pt-doped sensor respectively. In figure 8.11 D, the spectra of the photon energies at which difference curves were taken (see figures 8.12 and 8.13 A and B), are shown comparatively. The binding energies of the band gap states at around 3 eV, of the Sn 5*p*/O 2*p* states at around 8 eV and of the Sn 5*s*/O 2*p* states around 11 eV are labeled in figure 8.11 A and D.

The dispersion of the photoemission signal when changing the photon energy can be easily seen. Without any data evaluation, there is an obvious difference between the Pt-doped sensor and the two other sensors in the shape of the valence band spectra. The Pt-doping strongly affects the Sn 5*p*/O 2*p* derived part of the valence band region and also the shape of the valence band maximum (O 2*p*).

Difference Spectra

The aim of taking difference spectra from this dataset is to get comparative information between the different sensors. On the one hand, this can be done by subtracting the valence band spectra

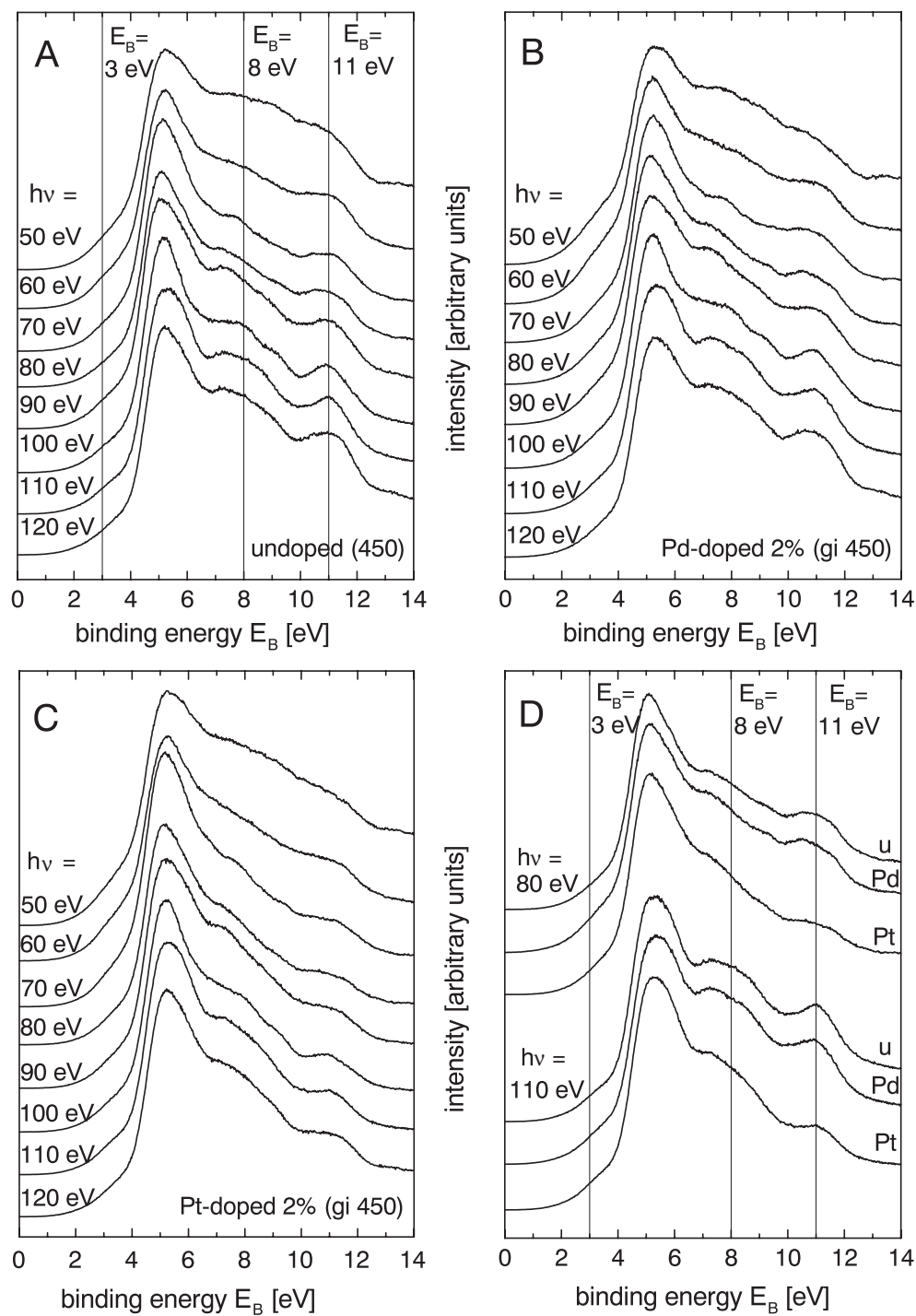


Figure 8.11: ResPES spectra of the undoped, Pd-doped and Pt-doped sensor taken every 10 eV for photon energies of 50-120 eV. Figure 'D' shows direct comparisons between these three types of sensors at two different photon energies.

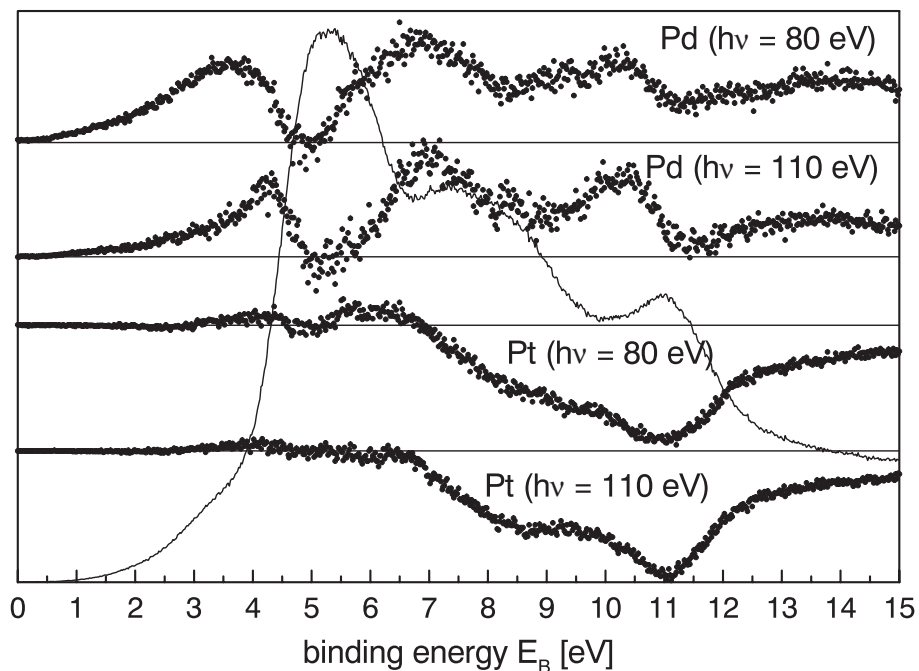


Figure 8.12: Difference spectra of Pd and Pt doped sensors in comparison to the undoped one. Spectra were generated by subtracting the spectra of the undoped sensor at 80 eV and 110 eV photon energy from the valence band spectra of the Pd and Pt doped sensor at the respective photon energy. The valence band spectrum shown in the background was recorded on the undoped sensors at $h\nu = 110$ eV.

of the undoped sensor from the valence band spectra of the other two sensors. The results of this data treatment are collected in figure 8.12. It can be seen that Pd doping results in a higher density of states in the band gap and in the Sn 5*p*/O 2*p* and Sn 5*s*/O 2*p* derived part of the valence band, whereas Pt doping results in a slightly increased photoemission signal in the band gap, but in a decrease in intensity at the binding energies of the oxygen/tin states. On the other hand, difference spectra of the sensors between 'resonance' and 'off-resonance' photon energies can give information about energetic positions in the valence band region which are dispersing.

It can be summarized that difference spectra of the same sensor (shown in figure 8.13) are qualitatively the same for all three sensors. That means only from these difference spectra no significant structure due to the doping can be identified. Nevertheless, there is an effect when considering the difference spectra between the undoped and the doped sensors of figure 8.12. This leads to the conclusion that the nature of the valence band states is not changed by the doping, but the density of certain states is affected. For example the density of states in the band gap is increased by both dopants and the photoemission in the oxygen/tin derived part of the valence band is altered in a contrary way.

CIS Curves

The CIS-curves shown in the right plot of figure 8.13 are consistent with the picture proposed above. Not only the difference curves, but also the way in which the intensities of the chosen binding energies vary as a function of the photon energy point toward the assumption that there are no new structures introduced to the valence band by the dopant. All CIS-curves show the same trend for each sensor when considering a reasonable uncertainty in the measurement and data evaluation.

Factor Analysis Results

This method offers a detailed study of the factors which are relevant for describing changes in a given dataset and is applied to the valence band spectra of the sensors in a similar way to the evaluation of the ResPES valence band spectra of the single crystal surfaces in section 8.1.2. The

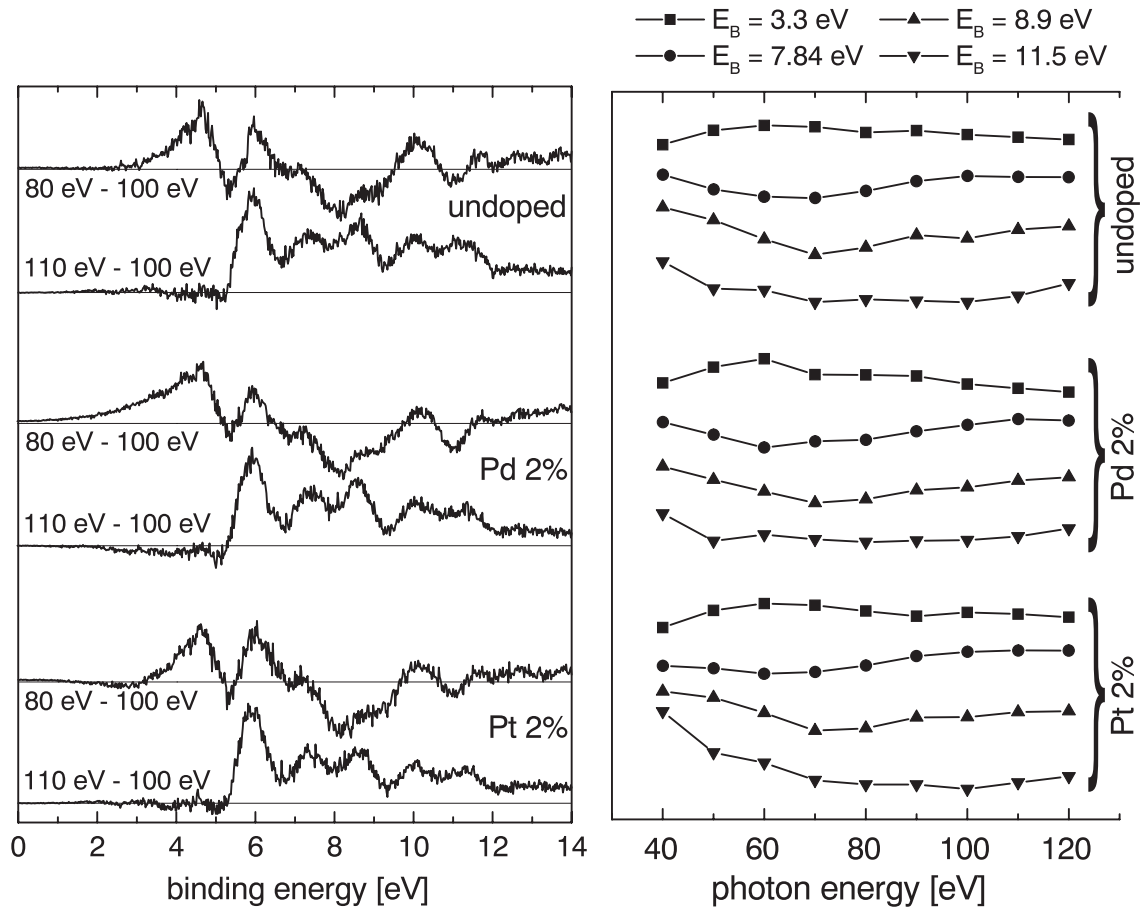


Figure 8.13: Difference spectra of the undoped, Pd and Pt doped sensor were calculated at the photon energies at which resonance effects are likely compared to the measurements on $\text{SnO}_2(110)$. The difference spectra were calculated by subtracting the valence band spectra taken at 100 eV from the spectra taken at 80 and 110 eV. The spectra were normalized by their intensity of the O $2p$ derived valence band maximum. Since the spectra to be subtracted from each other were all taken on the same sensor, band bending is not likely to happen and small shifts in the valence band maximum must be due to dispersing behavior of the O $2p$ states. CIS curves were generated from the raw data (see figure 8.11) at four electron binding energies at which strongest dispersion could be observed. The intensity in the CIS curves at each point is calculated by normalizing the intensity at the given binding energy to the integral intensity of the valence band spectrum for $0 \text{ eV} \leq E_B \leq 14 \text{ eV}$.

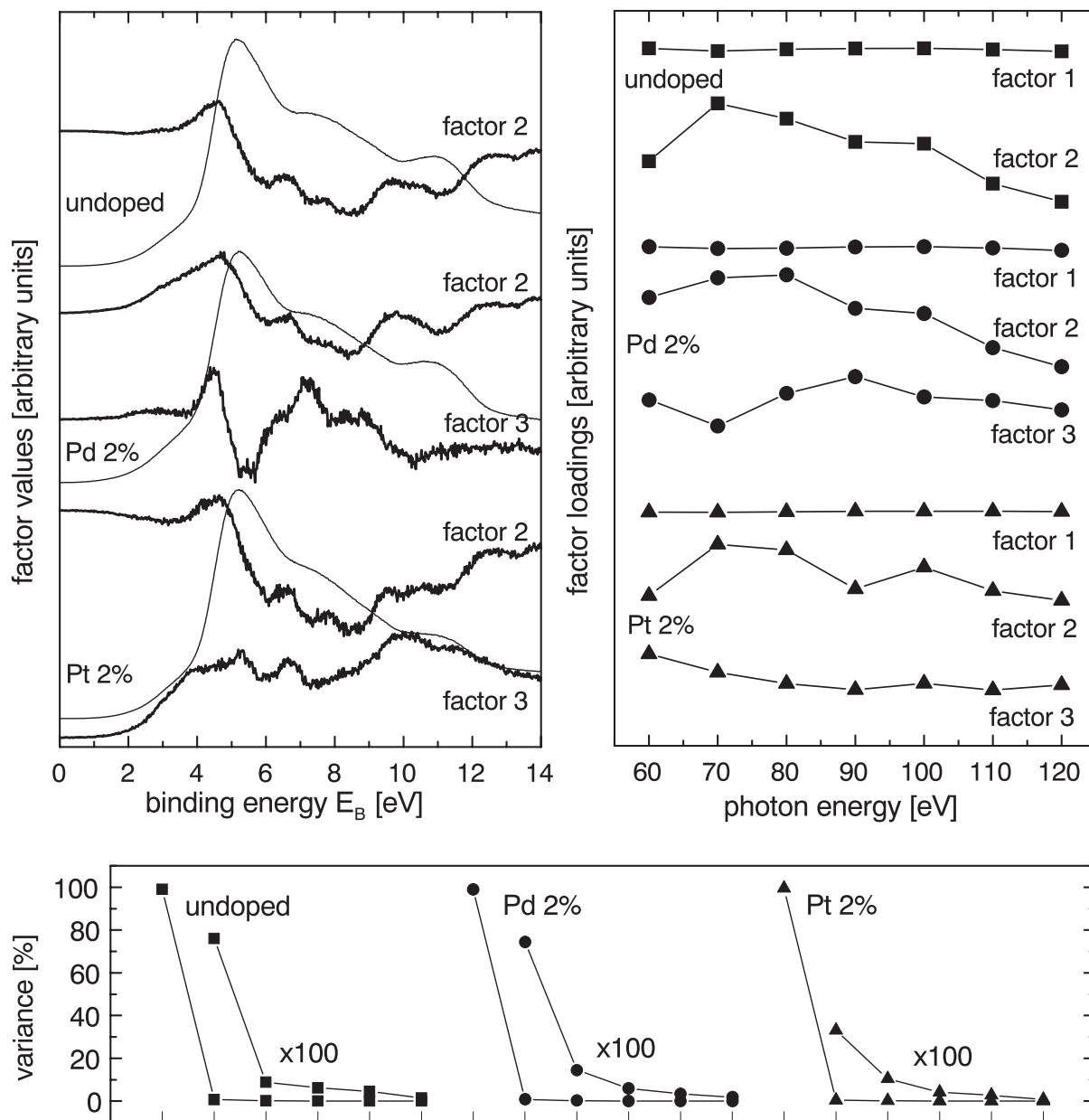


Figure 8.14: The calculated factor values are plotted in the left figure, the corresponding factor loadings in the right figure. When combining both, the raw data can be restored with very little deviation. The lower figure shows a plot of the six first eigenvalues, determined by principal components analysis and weighting on the $h\nu = 90$ eV valence band spectra. It can be seen that the third eigenvalue in the case of the Pd-doped sensor is higher than the corresponding eigenvalues of the other sensors.

factor values and loadings were calculated by principal components analysis with weighting on the valence band spectra taken at $h\nu = 90$ eV. For the undoped sensor only the first and second factor are plotted in figure 8.14, whereas for the doped sensors also the third factor is plotted respectively. The reason for this is that it can be assumed that an influence from the doping would be probably present in the third factor.

In order to judge the validity of the extracted third factors, it is important to look at the eigenvalues of the corresponding factor, which is actually only for the Pd-doped sensor significantly higher than for the undoped sensor. Therefore the results for the third factor of the Pt-doped sensor are only plotted for comparative reasons. That means that also the third factor and the related factor loading of the Pd-doped sensor is much more significant than for example the values and loadings of the third eigenvalue of the Pt-doped sensor.

The first factor is representing the valence band shape which is only marginally dispersing. The second factor is, in agreement with the difference spectra and the CIS-curves, qualitatively the same for all three sensors. Only the Pd-doped sensor shows an interesting structure in the third factor which might be comparable, with its local maximum in the O $2p$ /Sn $5p$ part of the valence band, to the second factor extracted from the valence band spectra of SnO₂(110)- 4×1 (see figure 8.6). Also the factor loading of the third factor fits very well in this picture because of the maximum at around $h\nu = 90$ eV.

To summarize, there was no influence of the dopant detectable in the valence band spectra of the sensors. In comparison to the undoped sensor and the single crystal data, all relevant effects could be traced back to a SnO₂ origin. Therefore it has to be assumed that the doping by gel-impregnation does not lead to an enrichment of the dopant on the grain surfaces, but to an incorporation of the dopant into the bulk material.

SIMS Spectra

As a very sensitive technique to especially detect light elements, SIMS was used to characterize the impurities of the sensor's surfaces following the ResPES experiments. The spectra in figure 8.15 are for all three sensors dominated by carbon compounds, alkaline metals and the tin peaks.

mass of isotopes [u] (amount [%], only for amounts > 5%)						
H	1 (99.99)					
C	12 (98.89)					
O	16 (99.76)					
Na	23 (100)					
K	39 (93.1)	41(6.88%)				
Ca	40 (96.97)					
Pd	104 (10.97)	105 (22.23)	106 (27.33)	108 (26.71)	110 (11.81)	
Sn	116 (14.30)	117 (7.61)	118 (24.03)	119 (8.58)	120 (32.85)	124 (5.94)
Pt	194 (32.9)	195 (33.8)	196 (25.3)	198 (7.21)		

Table 8.1: Elements and their isotopic distribution which are dominant in the SIMS spectra of figure 8.15 or of special interest for the discussion.

For both doped sensors only weak signal from the dopants can be identified. In table 8.1 isotopes with high intensity in the spectra or of interest for the material are listed. All three spectra were recorded under Ar⁺ ion bombardment at a kinetic energy of 10 keV, a beam current of 1.5 nA and a scanning area of about 2 mm². During the measuring time of about 20 min only weak sputter damage can be assumed. Positive secondary ions were collected since metals and their oxides are predominant in SIMS spectra of positive secondary ions, whereas spectra of negative ions are dominated by oxygen, halogens and carbon compounds.

Before discussing the spectra in detail, some typical properties of this method should be shortly reviewed. Since the spectra were recorded with a quadrupole mass spectrometer at constant resolution, the transmission decreases by $1/m$ [5]. Furthermore empirical and theoretical considerations imply a decrease in secondary ion production as a function of the isotopic mass [53, 119]. This leads to a domination of as-recorded SIMS spectra by light elements, especially by the alkaline metals sodium and potassium which are predominantly present as positive ions after sputtering.

It can be easily seen that all sensors are heavily contaminated, but in a very similar way. The

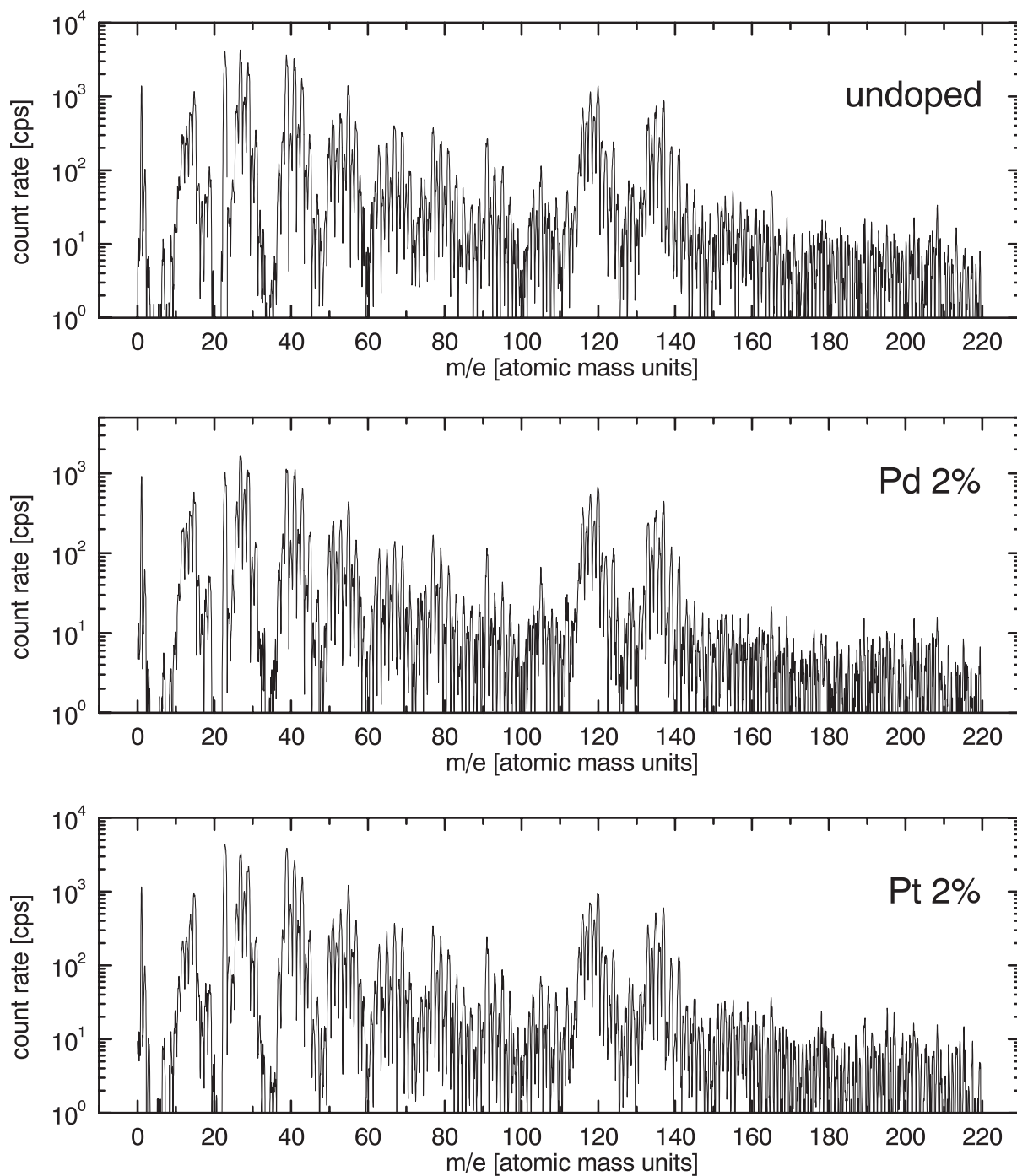


Figure 8.15: SIMS spectra taken on the sensors studied previously by SRPES, see figures 8.11-8.14. See text for further discussion.

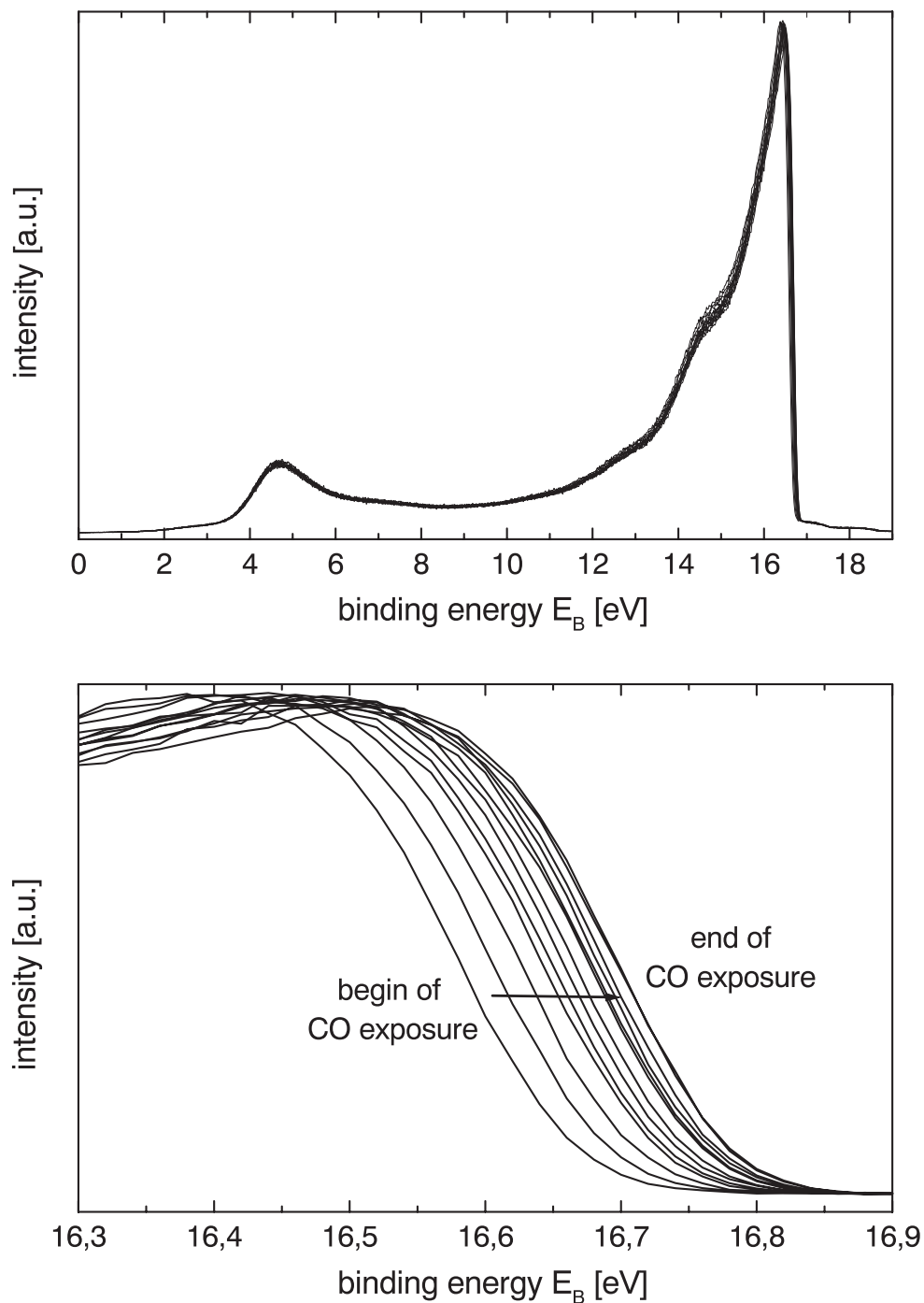


Figure 8.16: UPS spectra recorded one after another on the Pd-doped sensor under dosing CO in three cycles in a partial pressure range of 10^{-7} to 5×10^{-6} mbar.

strongest contamination can be related to carbon compounds (CH_x) at $m = 12-16$ u, which are probably also contributing to signals at higher mass. The dopants for the Pd- and the Pt-doped sensor are hardly detectable which on the one hand is due to the high background of fragment ions and on the other hand to their isotopic pattern which reduces the strongest isotope to 1/3 of the total elemental signal. Tin can be unequivocally identified in the spectra by its typical isotopic pattern. The second appearance at $\Delta m = 17$ higher mass can be related to SnOH^+ ionic molecules. On very pure metal oxide surfaces, only the oxidized signal would be expected. Because of the high amount of hydrogen present on the surface the hydroxylated compound seems to be more favorable. It can be summarized that despite the high level of contaminations all three sensors seem to be affected in a very similar way and therefore comparative considerations and their conclusions should hold.

8.3 CO Exposure monitored by UPS

The work function response of Pt- and Pd-doped SnO_2 gas sensors on CO was investigated by He I UPS. The applicable CO pressures ranging up to 5×10^{-6} mbar are actually very low when comparing them with gas test measurements under atmospheric pressure. A partial pressure of 10^{-6} mbar for example would correspond to the same amount of CO per volume unit than 1 ppb CO under atmospheric pressure. Since higher pressures than the applied CO partial pressures are not advisable when carrying out photoemission measurements, this is a significant restriction for the data acquisition. Nevertheless, a very small systematic change in the onset of He I UPS spectra could be detected for the Pd-doped sensor. Corresponding measurements on a Pt-doped sensor did not show any dependence of the onset on the applied partial pressure of CO.

The Pd-doped sensor was heated during measurement by the platinum heater mounted on the backside of the alumina substrate to around 200°C (see figure 4.2). This heat treatment results in a continuous desorption of surface species like for example water, carbon compounds or oxygen. A reduction of the surface due to the desorption of bridging oxygens can be expected as well. This process leads to a continuous shift at the onset of the spectra, i.e. of the surface's work function. In figure 8.16 the complete spectra (upper figure) and a zoom into the energy range

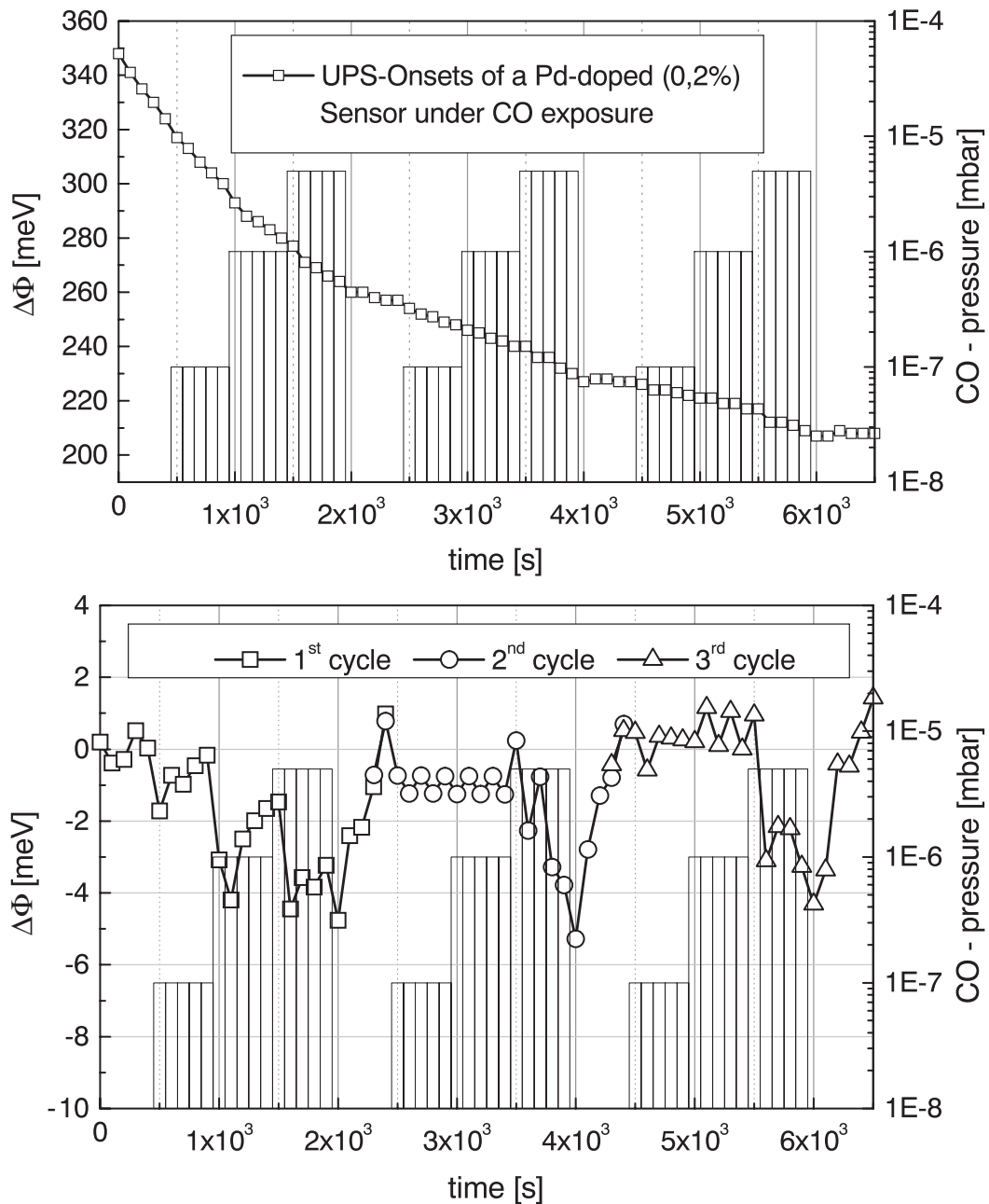


Figure 8.17: Work function changes $\Delta\Phi$ extracted from the UPS He I data shown in figure 8.16. The bargraphs in the background show the applied CO partial pressure in the corresponding period. The data in the lower figure can be obtained by subtracting an exponential decay from the data in the upper figure. It can be seen that the change in the work function is related to the applied CO partial pressure.

of the onset (lower figure) are shown. Since the only change detectable between the spectra is the work function $\Delta\Phi$, this parameter is extracted from the spectra and plotted as a function of time in figure 8.17. The dosed CO partial pressure is indicated by bargraphs in the background and was cycled three times in a pressure range of 10^{-7} to 5×10^{-6} mbar. The $\Delta\Phi$ values plotted in the upper figure of figure 8.17 are decaying exponentially due to the desorption process induced by the heat treatment. Nevertheless, there are small changes visible in this slope which can be correlated to the CO partial pressure applied to the sensor. The lower figure shows the 'background' subtracted data, i.e. the data when subtracting an exponential decay from the $\Delta\Phi$ values. It can be easily seen that there is a systematic correlation between work function change and dosed CO partial pressure.

The effect detected is in a range which is just accessible by photoemission spectroscopy and it points out that such measurements cannot be done in a systematic way by this approach since all measurement parameters were driven to their limits. Nevertheless, it can be summarized that CO dosing under UHV conditions leads to a reproducible and reversible (when only considering the CO pressure) change in the work function under dynamic conditions, i.e. not adsorption of CO at very low temperatures, but interaction of CO at a temperature which is exactly in the temperature range used for gas test measurements under ambient air conditions.

Chapter 9

Conclusions and Outlook

Summary

Real-space microscopy of reduced $\text{SnO}_2(110)$ surfaces could establish – supported by LEED and XPS investigations – a new model for the reconstruction process (section 7.1). Small and large area scans of the 4×1 reconstructed surface (section 7.2.1) point out the importance of this surface termination to be a well-defined model system for SnO_2 with a periodic defect structure. The reduced surface offers – with its high surface conductivity – not only the possibility for STM measurements which are not likely to be successful on stoichiometric surfaces, but also synchrotron radiation photoemission experiments at today's high intensity third generation light sources.

The valence band structure of ordered and disordered single crystal surfaces was investigated by ResPES (section 8.1.2) and doped and undoped SnO_2 gas sensors were measured (section 8.2) in comparison to these results. By establishing first the reproducibility of laboratory source UPS data obtained on these sensors (figures 8.9 and 8.10), a detailed investigation at the synchrotron light source opens up the opportunity to discuss features of the valence band spectrum in more detail.

Metal and gas interaction, Pd-clusters on the $\text{SnO}_2(110)-4 \times 1$ surface (section 7.2.3) and CO on a Pd-doped SnO_2 gas sensors (section 8.3) were presented as well.

Conclusions

Single crystal surface

Atomically resolved STM images could confirm the current model of STM imaging on reduced $\text{SnO}_2(110)$ surfaces and introduce a new surface structure of zigzag oxygen rows corresponding to a 2×1 surface structure (section 7.2.2).

By establishing a new, more detailed and revised reconstruction model and by the new possibility of preparing a well-defined 4×1 reconstruction of the $\text{SnO}_2(110)$ surface by the long-time annealing procedure described in section 7.1, further systematic investigations of gas and metal interaction on this well-defined defect structure are possible. Since gas-exposition experiments with STM and ResPES at room-temperature (H_2O , CO) were not successful during this thesis, i.e. no effect could be observed, such experiments have to be undertaken either at liquid nitrogen temperature or at elevated temperatures under monitoring the changes induced on the surface by reaction with the incoming gas molecules.

The discrepancy in the ResPES data of 4×1 reconstructed and freshly sputtered $\text{SnO}_2(110)$ could be tentatively explained by a Fano-type resonance that appears because of the interaction of the Sn $4p$ core-level with Sn $5s$ states in the conduction band (section 8.1.2).

Some implications specific for $\text{SnO}_2(110)$ should also be pointed out here. Most studies, including this thesis, are restricted to the reduced surface which can be relatively easily prepared by sputtering and annealing under UHV conditions. This concentration on the reduced surface results from two reasons. First, stoichiometric surfaces of $\text{SnO}_2(110)$ can only be prepared by annealing the crystal at temperatures around 700 K in 1 mbar of oxygen or 0.1 mbar of N_2O (the latter one is the stronger oxidant). These pressures are only applicable in separate high pressure cells and are not available at most equipment used for surface spectroscopic single crystal studies. The second reason is the conductivity of the surface. The reduced surface with its significant density of electronic states up to the Fermi level allows high intensity photoemission experiments and even the application of STM. For stoichiometric surfaces with their much lower conductivity, charging problems have to be expected.

The aim of this thesis to broaden the knowledge about reduced SnO₂(110) was successful with respect to the investigation of fundamental properties of the reduced SnO₂(110) surface and in acquiring comparative ResPES spectra between single crystal surfaces and real-life SnO₂ based gas sensors. The latter aspect is of particular importance because the attempt to get valuable information only from laboratory source is restricted to fixed wavelengths and is not offering a detailed assignment of observed structures to atomic levels.

SnO₂ gas sensors

Taking advantage of resonance effects in photoelectron spectra which appear as a function of the photon energy, enables the determination of the electronic valence band structure in much more detail than just by laboratory light sources. By comparing resonance effects on the single crystal surfaces with corresponding observations on doped and undoped SnO₂ material, valence band structures may be assigned either to the SnO₂ itself or to the dopant.

Despite the obvious differences in the valence band spectra of the three investigated sensors (see figure 8.11), the difference spectra of figure 8.13 and the results of the factor analysis (see figure 8.14) match each other very well. Even the deviation in the third factor of the Pd-doped sensor can be traced back to a tin-derived origin and does not seem to arise from the dopant itself. The latter result may be in correlation with the resonance observed on the ordered single crystal surface (see above), i.e. it may arise from the interaction between the Sn *4p* core-level and the conduction band.

All these results imply that the valence band structure is only quantitatively changed by the dopant, i.e. the intensities in the band gap region or at the Sn/O binding states are changed, but no new structure that might be attributed to the dopant itself appears, neither in the difference spectra nor in the CIS-curves (figures 8.11-8.14). This could be explained by the assumption that the dopant is mainly incorporated into the bulk, only in very low concentration present on the surface and therefore not accessible to photoelectron spectroscopy in the applied photon energy range. The changes in the density of states in the band gap which are almost independent of the doping amount in the UPS He II spectra (see figure 8.10), can also be explained by this model.

These states would therefore not be derived from the dopant, but from the SnO₂ material itself. Since the sensors are sintered in air at sufficiently high temperature to reoxidize the surface of undoped SnO₂, these band gap states which are typical for reduced SnO₂ and most probably due to unsaturated tin atoms on the surface, must be influenced and stabilized by the dopant.

This conclusion of course holds only for the influence of the dopant on the valence band structure. A statement about the catalytic properties cannot be made from the measurements presented here. That the doping material is not enriched on the surface may of course be restricted to the special preparation procedures of the nanocrystalline SnO₂ used in this study (see section 4.2).

Outlook

In spite of the strong demand and the effort that has been gone into understanding surface properties of SnO₂, only few aspects are well-established until now. Today's theoretical approaches with finite or infinite ab initio calculations can still only handle small clusters or unit cells. But with rapidly growing computer power more realistic calculations can be expected in the near future, able to handle large unit cells. This for example is a prerequisite for a further characterization of the 4×1 reconstruction.

The lack of experimental work actually is not due to a lack of interest or inadequate experimental techniques. The main reason for this is the lack of suitable substrates, since growing SnO₂ crystals in high quality and sufficient size is a very challenging and expensive task.

But even in the case of the probably best characterized metal oxide surface, the TiO₂(110) surface, for which substrates of very high quality are available, the surface structures appearing in UHV preparation and even the interpretation of STM images are controversially discussed (whereas for the interpretation of STM an almost complete agreement in one model has been developed in the meantime) [45, 102, 105].

The most promising approaches, surface spectroscopy on well-defined single crystal surfaces on the one hand and theoretical approaches on the other hand, are restricted to relatively simple problems compared to reality. Furthermore, most surface spectroscopic techniques require an

UHV or at least HV environment which complicates conclusions on measurements under ambient air conditions. For this reason, other spectroscopic techniques like for example soft X-ray emission spectroscopy (SXES) [180] have to be applied. SXES offers – under glancing incidence geometry – surface sensitivity and may even be applicable to SnO₂ gas sensors under gas-sensing operation in specially designed cells.

Actually, there also may be the possibility for detailed studies on stoichiometric surfaces by enhancing the surface and bulk conductivity in a controlled manner. The approach to only reduce the bulk material by heating to very high temperature – applied for example on TiO₂ samples – is not applicable in the case of SnO₂ crystals. By heat treatment, they are only reduced on the surface without significant oxygen out-diffusion from the bulk. Therefore, controlled doping by a group V element in order to introduce charge carriers to the n-type material, is a promising approach. Antimony doping has been studied in sufficient detail to offer such a perspective [29, 40, 131, 150, 167]. It injects charge carriers to the band gap region and leads to a significant density of occupied states up to the Fermi level and may in this way also be suitable to enable studies on single crystal samples at liquid nitrogen temperature.

Bibliography

- [1] S. R. M. Antunes, J. D. Santos, A. C. Antunes, E. Longo, and J. A. Varela. MNDO theoretical study of ethanol decomposition process on SnO₂ surfaces. *Theochem-Journal of Molecular Structure*, 357(1-2):153–159, 1995.
- [2] R. Z. Bachrach, editor. *Techniques*, volume 1 of *Synchrotron radiation research: Advances in surface and interface science*. Plenum Press, New York and London, 1992.
- [3] R. Z. Bachrach, editor. *Issues and technology*, volume 2 of *Synchrotron radiation research: Advances in surface and interface science*. Plenum Press, New York and London, 1992.
- [4] V. W. H. Baur. Über die Verfeinerung der Kristallstrukturbestimmung einiger Vertreter des Rutiltyps: TiO₂, SnO₂, GeO₂ und MgF₂. *Acta Crystallographica*, 9:515, 1956.
- [5] A. Benninghoven, F. G. Rüdener, and H. W. Werner. *Secondary ion mass spectrometry - basic concepts, instrumental aspects, applications and trends*, volume 86 of *Chemical Analysis*. John Wiley & Sons Inc., New York, 1987.
- [6] B. E. Bent. Mimicking aspects of heterogeneous catalysis: Generating, isolating, and reacting proposed surface intermediates on single crystals in vacuum. *Chemical Review*, 96:1361–1390, 1996.
- [7] G. Binnig and H. Rohrer. Scanning tunneling microscopy – from birth to adolescence. *Reviews of Modern Physics*, 59(3):615–625, 1987.
- [8] D. A. Bonnell, editor. *Scanning tunneling microscopy and spectroscopy: Theory, techniques, and applications*. VCH Publishers, Inc., New York, Weinheim, Cambridge, 1993.
- [9] D. Briggs and M. P. Seah, editors. *Auger and X-ray photoelectron spectroscopy*, volume 1 of *Practical Surface Analysis*. John Wiley & Sons Ltd., Chichester, 1983.
- [10] D. Briggs and M. P. Seah, editors. *Ion and neutral spectroscopy*, volume 2 of *Practical Surface Analysis*. John Wiley & Sons Ltd., Chichester, 1992.
- [11] J. R. Brown, M. T. Cheney, P. W. Haycock, D. J. Houlton, A. C. Jones, and E. W. Williams. The gas-sensing properties of tin oxide thin films deposited by metallorganic chemical vapor deposition. *Journal of the Electrochemical Society*, 144(1):295–299, 1997.

- [12] M. Calatayud, J. Andres, and A. Beltran. A theoretical analysis of adsorption and dissociation of CH_3OH on the stoichiometric $\text{SnO}_2(110)$ surface. *Surface Science*, 430(1-3):213–222, 1999.
- [13] A. C. Camargo, J. A. Iguelda, A. Beltran, R. Llusar, E. Longo, and J. Andres. An ab initio study of structural properties of TiO_2 , SnO_2 and GeO_2 rutile lattices. *Chemical Physics*, 212:381–391, 1996.
- [14] S. Carrez, B. Dragnea, W. Q. Zheng, H. Dubost, and B. Bourguignon. Site selective probe of the desorption of CO from Pd(111) by sum frequency generation and Fourier transform IR: a comparison of thermal and laser desorption. *Surface Science*, 440:151–162, 1999.
- [15] C. R. A. Catlow and G. N. Greaves, editors. *Applications of synchrotron radiation*. Blackie and Son Ltd, Glasgow, London, 1990.
- [16] R. Cavicchi and S. Semancik. Reactivity of Pd and Sn adsorbates on plasma and thermally oxidized $\text{SnO}_2(110)$. *Surface Science*, 257:70–78, 1991.
- [17] R. Cavicchi, V. Sukharev, and S. Semancik. Time-dependent conductance of Pd-dosed $\text{SnO}_2(110)$. *Surface Science*, 418(3):L81–L88, 1998.
- [18] R. Cavicchi, M. Tarlov, and S. Semancik. Preparation of well-ordered, oxygen-rich $\text{SnO}_2(110)$ surfaces via oxygen plasma treatment. *Journal of Vacuum Science and Technology A*, 8(3):2347–52, 1990.
- [19] M. Celino, F. Cleri, G. D’Agostino, and V. Rosato. Mechanical instability of oxidized metal clusters. *Physical Review Letters*, 77(12):2495–2498, 1996.
- [20] W. K. Choi, J. S. Cho, S. K. Song, H. J. Jung, and S.K. Koh. Auger electron and X-ray photoelectron spectroscopy studies of oxidation of tin using SnO_x thin films grown by reactive ion-assisted deposition. *Japanese Journal of Applied Physics Part 1 Regular Papers Short Notes and Review Papers*, 35(11):5820–5824, 1996.
- [21] P. H. Citrin and D. R. Hamann. Phonon broadening of x-ray photoemission line shapes in solids and its independence of hole state lifetimes. *Physical Review B*, 15(6):2923–2928, 1977.
- [22] P. H. Citrin and G. K. Wertheim. Many-body processes in x-ray photoemission line shapes from Li, Na, Mg and Al metals. *Physical Review B*, 16(10):4256–4282, 1977.
- [23] D. F. Cox and T. B. Fryberger. Preferential isotopic labeling of lattice oxygen positions on the $\text{SnO}_2(110)$ surface. *Surface Science Letters*, 227:105–108, 1990.
- [24] D. F. Cox, T. B. Fryberger, J. W. Erickson, and S. Semancik. Summary abstract: Surface properties of clean and gas-dosed $\text{SnO}_2(110)$. *Journal of Vacuum Science and Technology A*, 5:1170–1171, 1987.

- [25] D. F. Cox, T. B. Fryberger, and S. Semancik. Oxygen vacancies and defect electronic states on the $\text{SnO}_2(110)\text{-}1\times 1$ surface. *Physical Review B*, 38:2072–2083, 1988.
- [26] D. F. Cox, T. B. Fryberger, and S. Semancik. Summary abstract: Oxygen-vacancy-derived defect electronic states on the $\text{SnO}_2(110)$ surface. *Journal of Vacuum Science and Technology A*, 6(3):828–829, 1988.
- [27] D. F. Cox, T. B. Fryberger, and S. Semancik. Surface reconstructions of oxygen deficient $\text{SnO}_2(110)$. *Surface Science*, 224:121–142, 1989.
- [28] D. F. Cox, S. Semancik, and P. D. Szuromi. Summary abstract: Structural and electronic properties of clean and waterdosed $\text{SnO}_2(110)$. *Journal of Vacuum Science and Technology A*, 4(3):627–628, 1986.
- [29] P. A. Cox, R. G. Egdell, C. Harding, W. R. Patterson, and P. J. Tavener. Surface properties of antimony doped tin(IV) oxide: A study by electron spectroscopy. *Surface Science*, 123:179–203, 1982.
- [30] A. Cricenti, R. Generosi, M. A. Scarselli, P. Perfetti, P. Siciliano, A. Serra, A. Tepore, C. Coluzza, J. Almeida, and G. Margaritondo. Morphological, chemical and electrical characterization of Pt- SnO_2 thin film grown on rough and mechanically polished Al_2O_3 substrates. *Journal of Physics D Applied Physics*, 29(9):2235–2239, 1996.
- [31] L. C. Davis and L. A. Feldkamp. Interaction of many discrete states with many continua. *Physical Review B*, 15(6):2961–2969, 1977.
- [32] L. C. Davis and L. A. Feldkamp. $M_{2,3}$ spectrum of atomic Mn. *Physical Review A*, 17(6):2012–2022, 1978.
- [33] E. de Frésart, J. Darville, and J. M. Gilles. Surface reconstructions of the $\text{SnO}_2(110)$ face. *Solid State Communications*, 37:13–17, 1980.
- [34] E. de Frésart, J. Darville, and J. M. Gilles. Influence of the surface reconstruction on the work function and surface conductance of (110) SnO_2 . *Applied Surface Science*, 11:637–651, 1982.
- [35] E. de Frésart, J. Darville, and J. M. Gilles. Surface properties of tin dioxide single crystals. *Surface Science*, 126:518–522, 1983.
- [36] A. Dieguez, A. Romano-Rodriguez, J. R. Morante, U. Weimar, M. Schweizer-Berberich, and W. Göpel. Morphological analysis of nanocrystalline SnO_2 for gas sensor applications. *Sensors and Actuators B Chemical*, 31(1-2):1–8, 1996.
- [37] J. E. Drawdy, G. B. Hoflund, M. R. Davidson, B. T. Upchurch, and D. R. Schryer. Characterization study of polycrystalline tin oxide surfaces before and after reduction in CO. *Surface and Interface Analysis*, 19(1-12):559–564, 1992.

- [38] R. G. Egdell, S. Eriksen, and W. R. Flavell. A spectroscopic study of electron and ion beam reduction of SnO₂(110). *Surface Science*, 192:265–274, 1987.
- [39] R. G. Egdell, A. Gulino, C. Rayden, G. Peacock, and P. A. Cox. Nature of donor states in V-doped SnO₂. *Journal of Materials Chemistry*, 5(3):499–504, 1995.
- [40] R. G. Egdell, J. Rebane, T. J. Walker, and D. S. L. Law. Competition between initial- and final-state effects in valence- and core-level X-ray photoemission of Sb-doped SnO₂. *Physical Review B*, 59(3):1792–1799, 1999.
- [41] J. W. Erickson, T. B. Fryberger, and S. Semancik. Metal/semiconductor interfaces on SnO₂(110). *Journal of Vacuum Science and Technology A*, 6(3):1593–1598, 1988.
- [42] J. W. Erickson and S. Semancik. Surface conductivity changes in SnO₂(110): Effects of oxygen. *Surface Science*, 187:L658–L668, 1987.
- [43] G. Ertl and J. Küppers. *Low energy electrons and surface chemistry*. VCH, Weinheim, 1985.
- [44] U. Fano. Effects of configuration interaction on intensities and phase shifts. *Physical Review*, 124(6):1866–1878, 1961.
- [45] H.J. Freund. Introductory Lecture. *Faraday Discussions*, 114:1–31, 1999.
- [46] T. B. Fryberger and S. Semancik. Conductance response of Pd/SnO₂(110) model gas sensors to H₂ and O₂. *Sensors and Actuators B-Chemical*, 2(4):305–309, 1990.
- [47] J. F. Geiger. *Chemische Sensoren auf der Basis von Pd dotiertem SnO₂: Vergleichende grenzflächenspektroskopische und elektrische Messungen*. PhD thesis, Eberhard-Karls-Universität Tübingen, Institut für Physikalische und Theoretische Chemie, Tübingen, 1992.
- [48] J. F. Geiger, P. Beckmann, K. D. Schierbaum, and W. Göpel. Interaction of Pd-overlayers with SnO₂: comparative XPS, SIMS, and SNMS studies. *Fresenius Journal of Analytical Chemistry*, 341:25–30, 1991.
- [49] J. F. Geiger, K. D. Schierbaum, and W. Göpel. Surface spectroscopic studies on Pd-doped SnO₂. *Vacuum*, 41(7-9):1629–1632, 1990.
- [50] V. A. Gercher and D. F. Cox. Formic-acid decomposition on SnO₂(110). *Surface Science*, 312(1-2):106–114, 1994.
- [51] V. A. Gercher and D. F. Cox. Water adsorption on stoichiometric and defective SnO₂(110) surfaces. *Surface Science*, 322(1-3):177–184, 1995.
- [52] V. A. Gercher, D. F. Cox, and J-M. Themlin. Oxygen-vacancy-controlled chemistry on a metal oxide surface: Methanol dissociation and oxidation on SnO₂(110). *Surface Science*, 306:279–293, 1994.

- [53] W. Gerhard and C. Plog. Secondary ion emission by nonadiabatic dissociation of nascent ion molecules with energies depending on solid composition. *Zeitschrift für Physik B - Condensed Matter*, 54:59–70, 1983.
- [54] C. Giacovazzo, editor. *Fundamentals of Crystallography*. Oxford University Press, Oxford, 1992.
- [55] T. Gießel, O. Schaff, C. J. Hirschmugl, V. Fernandez, K.-M. Schindel, A. Theobald, S. Bao, R. Lindsay, W. Berndt, A. M. Bradshaw, C. Baddeley, A. F. Lee, R. M. Lambert, and D. P. Woodruff. A photoelectron diffraction study of ordered structures in the chemisorption system Pd(111)-CO. *Surface Science*, 406:90–102, 1998.
- [56] T. J. Godin and J. P. Lafemina. Surface atomic and electronic structure of cassiterite SnO₂(110). *Physical Review B-Condensed Matter*, 47(11):6518–6523, 1993.
- [57] J. Goniakowski and M. J. Gillan. The adsorption of H₂O on TiO₂ and SnO₂ (110) studied by first-principles calculations. *Surface Science*, 350:145–158, 1996.
- [58] J. Goniakowski, J. M. Holender, L. N. Kantorovich, M. J. Gillan, and J. A. White. Influence of gradient corrections on the bulk and surface properties of TiO₂ and SnO₂. *Physical Review B - Condensed Matter*, 53(3):957–960, 1996.
- [59] D. W. Goodman. Catalysis - from single crystals to the real world. *Surface Science*, 300(1-3):837–848, 1994.
- [60] W. Göpel. Chemisorption and charge transfer at ionic semiconductor surfaces: Implications in designing gas sensors. *Progress in Surface Science*, 20(1):9–103, 1985.
- [61] M. Gostein, E. Watts, and G. O. Sitz. Vibrational relaxation of H₂($\nu=1, J=1$) on Pd(111). *Physical Review Letters*, 79(15):2891–2894, 1997.
- [62] H. Graoui, S. Giorgio, and C. R. Henry. Shape variations of Pd particles under oxygen adsorption. *Surface Science*, 417:350–360, 1998.
- [63] M.-P. Habas, F. Mele, M. Sodupe, and F. Illas. Density functional cluster model study of bonding and coordination modes CO₂ on Pd(111). *Surface Science*, 431:208–219, 1999.
- [64] H. Haken and H. C. Wolf. *Atom- und Quantenphysik*. Springer-Verlag, Berlin, Heidelberg, New York, 1993.
- [65] B. Hammer, Y. Morikawa, and J. K. Norskov. CO chemisorption at metal surfaces and overlayers. *Physical Review Letters*, 76(12):2141–2144, 1996.
- [66] B. Hammer and J. K. Norskov. Adsorbate reorganization at steps: NO on Pd(211). *Physical Review Letters*, 79(22):4441–4444, 1997.

- [67] K. H. Hansen, T. Worren, S. Stempel, E. Laegsgaard, M. Bäumer, and H.-J. Freund. Palladium nanocrystals on Al_2O_3 : Structure and adhesion energy. *Physical Review Letters*, 83(20):4120–4123, 1999.
- [68] G. Heiland and D. Kohl. *Chemical Sensor Technology*, report 2, pages 15–38. Kodansha, Tokyo, 1988.
- [69] A. Heilig. *Selektivitätssteigerung von SnO_2 -Gassensoren*. PhD thesis, Eberhard-Karls-Universität Tübingen, Institut für Physikalische und Theoretische Chemie, Tübingen, 1999.
- [70] A. Heilig, N. Bârsan, U. Weimar, M. Schweizer-Berberich, J. W. Gardner, and W. Göpel. Gas identification by modulating temperatures of SnO_2 based thick film sensors. *Sensors and Actuators B*, 43:45–51, 1997.
- [71] V. E. Henrich. The surfaces of metal oxides. *Reports on Progress in Physics*, 48:1481–1541, 1985.
- [72] V. E. Henrich. Metal-oxide surfaces. *Progress in Surface Science*, 50(1-4):77–90, 1995.
- [73] V. E. Henrich and P. A. Cox. *The Surface Science of Metal Oxides*. Cambridge University Press, Cambridge, 1994.
- [74] M. Henzler and W. Göpel. *Oberflächenphysik des Festkörpers*. B.G. Teubner, Stuttgart, 1994.
- [75] R. I. Hines, N. L. Allan, and W. R. Flavell. Oxidation catalysts: A comparative simulation study of the lattice, defect and surface structure of the stannates ASnO_3 ($A=\text{Ca}$, Sr and Ba) and SnO_2 . *Journal of the Chemical Society Faraday Transactions*, 92(12):2057–2063, 1996.
- [76] M. Hirsimäki, S. Suhonen, J. Pere, M. Valden, and M. Pessa. Adsorption, desorption and surface reactions of CO and NO on Pd(320). *Surface Science*, 402-404:187–191, 1998.
- [77] G. B. Hoflund. Characterization study of oxidized polycrystalline tin oxide surfaces before and after reduction in H_2 . *Chemistry of Materials*, 6(4):562–568, 1994.
- [78] S. Hofmann and J. Steffen. Factor analysis and superposition of Auger electron spectra applied to room temperature oxidation of Ni and $\text{NiCr}_{12}\text{Fe}_{12}$. *Surface and Interface Analysis*, 14:59–65, 1989.
- [79] P. C. Hollamby, P. S. Aldrige, G. Moretti, and R. G. Egdell. The influence of oxygen deficiency and Sb doping on inverse photoemission spectra of SnO_2 . *Surface Science*, 280:393–397, 1993.
- [80] M. Holzwart, M. Wißing, D. S. Simeonova, S. Tzanev, K. J. Snowdon, and O. I. Yordanov. Preparation of atomically smooth surfaces via sputtering under glancing incidence conditions. *Surface Science*, 331-333:1093–1098, 1995.

- [81] J. S. G. Irwin, A. F. Prime, P. J. Hardman, P. L. Wincott, and G. Thornton. The interconversion of SnO₂(110) reduced phases by reaction with formic acid. *Surface Science*, 352:480–484, 1996.
- [82] H. Jacobs, W. Mokwa, D. Kohl, and G. Heiland. Characterization of structure and reactivity of ZnO and SnO₂ supported Pd catalysts. *Vacuum*, 33:869–870, 1983.
- [83] Z. M. Jarzebski and J. P. Marton. Physical properties of SnO₂ materials – I. Preparation and defect structure. *Journal of the electrochemical Society*, 123:199c–205c, 1976.
- [84] Z. M. Jarzebski and J. P. Marton. Physical properties of SnO₂ materials – II. Electrical properties. *Journal of the electrochemical Society*, 123:299c–310c, 1976.
- [85] Z. M. Jarzebski and J. P. Marton. Physical properties of SnO₂ materials – III. Optical properties. *Journal of the electrochemical Society*, 123:333c–346c, 1976.
- [86] V. M. Jiménez, G. Lassaletta, A. Fernández, J. P. Espinós, F. Yubero, and A. R. González-Elipe. Resonant photoemission characterization of SnO. *Physical Review B*, 60(15):11171–11179, 1999.
- [87] Z. H. Jin, H. J. Zhou, Z. L. Jin, R. F. Savinelli, and C. C. Liu. Application of nanocrystalline porous tin oxide thin film for CO sensing. *Sensors and Actuators B-Chemical*, 52(1-2):188–194, 1998.
- [88] L. I. Johansson, J. W. Allen, I. Lindau, M. H. Hecht, and S. B. M. Hagström. Photoemission from Yb: Valence-change-induced Fano resonance. *Physical Review B*, 21(4):1408–1411, 1980.
- [89] F. H. Jones, R. Dixon, J. S. Foord, and R. G. Egdell. The surface structure of SnO₂(110)-(4×1) revealed by scanning tunneling microscopy. *Surface Science*, 376:367–373, 1997.
- [90] I. Z. Jones, R. A. Bennett, and M. Bowker. CO adsorption on Pd(110). *Surface Science*, 402-404:595–598, 1998.
- [91] I. Z. Jones, R. A. Bennett, and M. Bowker. CO oxidation on Pd(110): a high-resolution XPS and molecular beam study. *Surface Science*, 439:235–248, 1999.
- [92] J. Kappler, N. Bârsan, U. Weimar, A. Diègez, J. L. Alay, A. Romano-Rodriguez, J. R. Morante, and W. Göpel. Correlation between XPS, Raman and TEM measurements and gas sensitivity of Pt and Pd doped SnO₂ based gas sensors. *Fresenius Journal of Analytical Chemistry*, 361:110–114, 1998.
- [93] H. Kato, J. Yoshinobu, and M. Kawai. Determination of six types of vibrational mode for bridge CO on Pd(110). *Surface Science*, 427-428:69–73, 1999.
- [94] K. Kimura, Y. Ohno, and T. Matsushima. Translational energy change of desorbing product on steady-state carbon monoxide oxidation on palladium (110). *Surface Science*, 429:L455–L461, 1999.

- [95] D. Kohl, W. Thoren, U. Schnakenberg, G. Schull, and G. Heiland. Decomposition of gaseous acetic-acid on SnO₂. *Journal of the Chemical Society-Faraday Transactions*, 87(16):2647–2653, 1991.
- [96] L. Kövér, Zs. Kovács, R. Sanjinés, G. Moretti, I. Cserny, G. Margaritondo, J. Pálinkás, and H. Adachi. Electronic structure of tin oxides: High-resolution study of XPS and Auger spectra. *Surface and Interface Analysis*, 23:461–466, 1995.
- [97] L. Kövér, G. Moretti, Z. Kovács, R. Sanjinés, I. Cserny, G. Margaritondo, J. Pálinkás, and H. Adachi. High-resolution photoemission and auger parameter studies of electronic-structure of tin oxides. *Journal of Vacuum Science and Technology A*, 13(3):1382–1388, 1995.
- [98] A. K. Kulkarni and S. A. Knickerbocker. Estimation and verification of the electrical properties of indium tin oxide based on the energy band diagram. *Journal of Vacuum Science and Technology A Vacuum Surfaces and Films*, 14(3 Part 2):1709–1713, 1996.
- [99] R. Larciprete, E. Borsella, P. Depadova, M. Mangiantini, P. Perfetti, and M. Fanfoni. Synchrotron radiation photoemission analysis of ArF laser deposited tin oxide. *Journal of Vacuum Science and Technology A*, 11(2):336–340, 1993.
- [100] C. L. Lau and G. K. Wertheim. Oxidation of tin: An ESCA study. *Journal of Vacuum Science and Technology*, 15(2):622–624, 1978.
- [101] V. Ledentu, W. Dong, and P. Sautet. Ab initio study of the dissociative adsorption of H₂ on the Pd(110) surface. *Surface Science*, 412/413:518–526, 1998.
- [102] M. Li, W. Hebenstreit, U. Diebold, M. A. Henderson, and D. R. Jennison. Oxygen-induced restructuring of rutile TiO₂(110): Formation mechanism, atomic models, and influence on surface chemistry. *Faraday Discussions*, 114:245–258, 1999.
- [103] Z. S. Li, Q. L. Guo, and P. J. Møller. Electronic properties of Cu clusters and islands and their reaction with O₂ on SnO₂(110) surfaces. *Zeitschrift für Physik D*, 40(1-4):550–553, 1997.
- [104] D. Loffreda, D. Simon, and P. Sautet. Dependence of stretching frequency on surface coverage and adsorbate-adsorbate interactions: a density-functional theory approach of CO on Pd(111). *Surface Science*, 425:68–80, 1999.
- [105] T. E. Madey. Concluding remarks. *Faraday Discussions*, 114:461–465, 1999.
- [106] I. Manassidis, J. Goniakowski, L.N. Kantorovich, and M.J. Gillan. The structure of the stoichiometric and reduced SnO₂(110) surface. *Surface Science*, 339:258–271, 1995.
- [107] S. Munnix and M. Schmeits. Surface electronic structure of SnO₂(110). *Solid State Communications*, 43(11):867–871, 1982.

- [108] S. Munnix and M. Schmeits. Electronic structure of tin dioxide surfaces. *Physical Review B*, 27(12):7624–7635, 1983.
- [109] S. Munnix and M. Schmeits. Surface electronic structure of rutile-type semiconductors: SnO₂(110) and TiO₂(110). *Surface Science*, 126:20–24, 1983.
- [110] S. Munnix and M. Schmeits. Electronic structure of point defects on oxide surfaces. *Physical Review B*, 33(6):4136–4144, 1986.
- [111] S. Munnix and M. Schmeits. Electronic structure of oxygen vacancies on TiO₂(110) and SnO₂(110) surfaces. *Journal of Vacuum Science and Technology A*, 5(4):910–913, 1987.
- [112] U. Muschiol, P. K. Schmidt, and K. Christmann. Adsorption and absorption of hydrogen on a palladium (210) surface: a combined LEED, TDS, $\Delta\Phi$ and HREELS study. *Surface Science*, 395:182–204, 1998.
- [113] Y. Nagasawa, T. Choso, T. Karasuda, S. Shimomura, F. Ouyang, K. Tabata, and Y. Yamaguchi. Photoemission study of the interaction of a reduced thin film SnO₂ with oxygen. *Surface Science*, 433-435:226–229, 1999.
- [114] P. D. Nolan, B. R. Lutz, P. L. Tanaka, and C. B. Mullins. Direct verification of a high-translational-energy molecular precursor to oxygen dissociation on Pd(111). *Surface Science*, 419:L107–L113, 1998.
- [115] P. De Padova, R. Larciprete, M. Mangiantini, and M. Fanfoni. Cr, Sn and Ag/SnO₂ interface formation studied by synchrotron radiation induced UPS. *Journal of Electron Spectroscopy and Related Phenomena*, 76:499–504, 1995.
- [116] P. De Padova, R. Larciprete, C. Ottaviani, C. Quaresima, P. Perfetti, E. Borsella, C. Astaldi, C. Comicioli, C. Crotti, M. Mateucci, M. Zacchigna, and K. Prince. Synchrotron radiation photoelectron spectroscopy of the O(2s) core level as a tool for monitoring the reducing effects of ion bombardement on SnO₂ thin films. *Surface Science*, 104:349–353, 1996.
- [117] C. L. Pang, S. A. Haycock, H. Raza, P. J. Møller, and G. Thornton. Structures of the 4×1 and 1×2 reconstructions of SnO₂(110). *Physical Review B*, 62(12):R7775–R7778, 2000.
- [118] E. Paparazzo, G. Fierro, G. M. Ingo, and N. Zacchetti. XPS studies on the surface thermal modifications of tin oxides. *Surface and Interface Analysis*, 12:438–439, 1988.
- [119] C. Plog, L. Wiedmann, and A. Benninghoven. Empirical formulae for the calculation of secondary ion yields from oxidized metal surfaces and metal oxides. *Surface Science*, 67:565–580, 1977.
- [120] E. W. Plummer and W. Eberhardt. Angle-resolved photoemission as a tool for the study of surfaces. *Advances in Chemical Physics*, 49:533–656, 1982.

- [121] J. J. Quinn. Range of excited electrons in metals. *Physical Review*, 126(4):1453–1457, 1962.
- [122] M. G. Ramsey, F. P. Leisenberger, F. P. Netzer, A. J. Raval, and R. Roberts. High-resolution core-level photoemission of the CO-induced Pd(110) surface reconstruction. *Surface Science*, 385:207–215, 1997.
- [123] T. Rantala, V. Lantto, and Rantala T. Computational approach to the chemical sensitivity of semiconducting tin dioxide. *Sensors and Actuators B*, 47(1-3):59–64, 1998.
- [124] T. S. Rantala, V. Golovanov, and V. Lantto. A cluster approach for the adsorption of oxygen and carbon-monoxide on SnO₂ and CdS surfaces. *Sensors and Actuators B-Chemical*, 25(1-3):532–536, 1995.
- [125] T. S. Rantala and V. Lantto. Computational approach for the chemical sensitivity of oxide and sulphide semiconductor surfaces. *Physica Scripta*, T69:259–263, 1997.
- [126] T. S. Rantala, V. Lantto, and T. T. Rantala. A cluster approach for modeling of surface characteristics of stannic oxide. *Physica Scripta*, 54:252–255, 1994.
- [127] T. S. Rantala, V. Lantto, and T. T. Rantala. A cluster approach for the SnO₂(110) face. *Sensors and Actuators B-Chemical*, 19(1-3):716–719, 1994.
- [128] T. T. Rantala, T. S. Rantala, and V. Lantto. Surface relaxation of the (110) face of rutile SnO₂. *Surface Science*, 420(1):103–109, 1999.
- [129] C. S. Rastomjee, R. S. Dale, R. J. Schaffer, F. H. Jones, R. G. Egdell, G. C. Georgiadis, M. J. Lee, T. J. Tate, and L. L. Cao. An investigation of doping of SnO₂ by ion implantation and application of ion-implanted films as gas sensors. *Thin Solid Films*, 279(1-2):98–105, 1996.
- [130] C. S. Rastomjee, R. G. Egdell, G. C. Georgiadis, M. J. Lee, and T. J. Tate. n-type doping of SnO₂ thin films by Sb ion implantation. *Journal of Materials Chemistry*, 2(5):511–520, 1992.
- [131] M. Rekas and Z. Szklarski. Defect chemistry of antimony doped SnO₂ thin films 2: Electrical properties. *Bulletin of the Polish Academy of Sciences-Chemistry*, 44(3):163–177, 1996.
- [132] J. A. Rodriguez and D. W. Goodman. High-pressure catalytic reaction over single-crystal metal surfaces. *Surface Science Reports*, 14:1–107, 1991.
- [133] E. Sanchez, L. Guillemot, and V. A. Esaulov. Electron transfer in the interaction of fluorine and hydrogen with Pd(100): The case of a transition metal versus jellium. *Physical Review Letters*, 83(2):428–431, 1999.

- [134] R. Sanjines, D. Rosenfeld, F. Gozzo, P. Almeras, L. Perez, F. Levy, G. Margaritondo, and W. H. Schreiner. ESCA investigation of SnO_x films used as gas sensors. *Surface and Interface Analysis*, 22(1-12):372–375, 1994.
- [135] G. Sberveglieri, G. Faglia, S. Groppelli, P. Nelli, and C. Perego. Oxygen gas-sensing properties of undoped and Li-doped SnO_2 thin-films. *Sensors and Actuators B-Chemical*, 13(1-3):117–120, 1993.
- [136] K. D. Schierbaum. *Elektrische und spektroskopische Untersuchungen an Dünnschicht- SnO_2 -Gassensoren*. PhD thesis, Eberhard-Karls-Universität Tübingen, Institut für Physikalische und Theoretische Chemie, Tübingen, 1987.
- [137] K. D. Schierbaum, U. Kirner, J. Geiger, and W. Göpel. Schottky-barrier and conductivity gas sensors based upon Pd/ SnO_2 and Pt/ TiO_2 . *Sensors and Actuators B*, 4:87–94, 1991.
- [138] K. D. Schierbaum, U. Weimar, and W. Göpel. Comparison of ceramic, thick film and thin film chemical sensors based upon SnO_2 . *Sensors and Actuators B*, 7:709–716, 1992.
- [139] M. Schweizer-Berberich. *Gas sensors based on stannic oxide*. PhD thesis, Eberhard-Karls-Universität Tübingen, Institut für Physikalische und Theoretische Chemie, 1998.
- [140] M. Schweizer-Berberich, JG. Zheng, U. Weimar, W. Göpel, N. Bârsan, E. Pentia, and A. Tomescu. The effect of Pt and Pd surface doping on the response of nanocrystalline tin dioxide gas sensors to CO. *Sensors and Actuators B*, 31(1-2):71–75, 1996.
- [141] J. H. Scofield. Hartree-Slater subshell photoionization cross-sections at 1254 and 1487 eV. *Journal of Electron Spectroscopy and Related Phenomena*, 8:129–137, 1976.
- [142] M. P. Seah and W. A. Dench. Quantitative electron spectroscopy of surfaces: A standard data base for electron inelastic mean free paths. *Surface and Interface Analysis*, 1(1):2–11, 1979.
- [143] S. Semancik and D. F. Cox. Fundamental characterization of clean and gas-dosed tin oxide. *Sensors and Actuators*, 12:101–106, 1987.
- [144] F. R. Sensato, E. Longo, L. O. S. Bulhoes, J. D. Santos, and J. B. L. Martins. A theoretical study of lithium ion interaction with tin oxide. *Theochem-Journal of Molecular Structure*, 394(2-3):259–265, 1997.
- [145] P. Serrini, V. Briois, M. C. Horrillo, A. Traverse, and L. Manes. Chemical composition and crystalline structure of SnO_2 thin films used as gas sensors. *Thin Solid Films*, 304(1-2):113–122, 1997.
- [146] G. L. Shen, R. Casanova, and G. Thornton. Interaction of O_2 with $\text{SnO}_2(110)1 \times 1$ and 4×1 . *Vacuum*, 43(11):1129–1131, 1992.

- [147] G. L. Shen, R. Casanova, G. Thornton, and I. Colera. Correlation between the surface conductivity and structure of SnO₂(110). *Journal of Physics-Condensed Matter*, 3:S291–S296, 1991.
- [148] P. M. A. Sherwood. Valence-band spectra of tin oxides interpreted by X α calculations. *Physical Review B*, 41(14):10151–10154, 1990.
- [149] M. Sinner. Aufbau einer SIMS - Sekundärionenmassenspektrometrie - Apparatur. Master's thesis, Eberhard-Karls-Universität Tübingen, Institut für Physikalische und Theoretische Chemie, Tübingen, 1997.
- [150] B. Slater, R. A. Catlow, D. H. Gay, D. E. Williams, and V. Dusastre. Study of the surface segregation of Antimony on SnO₂ surfaces by computer simulation techniques. *Journal of Physical Chemistry B*, 103:10644–10650, 1999.
- [151] *STATISTICA für Windows [Computer-Programm-Handbuch]*. Statsoft Inc., 2300 East 14th Street, Tulsa, OK 74104, WEB: <http://www.statsoftinc.com>, 1996.
- [152] J. Szuber. Electronic properties and origin of gap states on the clean SnO₂(110) surface exposed to oxygen. *Physics Status Solidi*, 185(K9):183–186, 1994.
- [153] J. Szuber and G. Czempik. Photoemission yield study of the fermi level position on the clean SnO₂(110) surface exposed to oxygen. *Vacuum*, 48:289–291, 1997.
- [154] J. Szuber and M. Piwowarczyk. Electronic properties of the space charge layer of the clean SnO₂(110) surface. *Vacuum*, 45(2-3):215–217, 1994.
- [155] N. Tagushi. Japanese Patent. 45-38200.
- [156] N. Tagushi. Japanese Patent. 47-38840.
- [157] N. Tagushi. US Patent. 3 644 795.
- [158] J. M. Themlin, M. Chtaïb, L. Henrard, P. Lambin, J. Darville, and J. M. Gilles. Characterization of tin oxides by X-ray-photoemission spectroscopy. *Physical Review B*, 46(4):2460–2466, 1992.
- [159] J. M. Themlin, J. M. Gilles, and R. L. Johnson. Oxygen 2s spectroscopy of tin oxides with synchrotron-radiation-induced photoemission. *Journal de Physique IV*, 4(C9):183–186, 1994.
- [160] J. M. Themlin, R. Sporcken, J. Darville, R. Caudano, and J. M. Gilles. Resonant-photoemission study of SnO₂: Cationic origin of the defect band-gap states. *Physical Review B*, 42:11914–11925, 1990.
- [161] B. Thiel and R. Helbig. Growth of SnO₂ single crystals by a vapour phase reaction method. *Journal of Crystal Growth*, 32:259–264, 1976.

- [162] W. Thoren, D. Kohl, and G. Heiland. Kinetic studies of the decomposition of CH_3COOH and CH_3COOD on SnO_2 single crystals. *Surface Science*, 162:402–410, 1985.
- [163] P. Türkes, Ch. Pluntke, and R. Helbig. Thermal conductivity of SnO_2 single crystals. *Journal of Physics C Solid State Physics*, 13:4941–51, 1980.
- [164] O. K. Varghese, L. K. Malhotra, and G. L. Sharma. High ethanol sensitivity in sol-gel derived SnO_2 thin films. *Sensors and Actuators B-Chemical*, 55(2-3):161–165, 1999.
- [165] J. Vetrone, Y. W. Chung, R. Gavicchi, and S. Semancik. Role of initial conductance and gas pressure on the conductance response of single-crystal SnO_2 thin films to H_2 , O_2 , and CO . *Journal of Applied Physics*, 73:8371–8376, 1993.
- [166] J. C. Vickerman, A. Brown, and N. M. Reed, editors. *Secondary ion mass spectrometry - principles and applications*, volume 17 of *International Series of Monographs on Chemistry*. Clarendon Press, Oxford, 1989.
- [167] H. Virola and L. Niinisto. Controlled growth of antimony-doped tin dioxide thin films by atomic layer epitaxy. *Thin Solid Films*, 251:127–135, 1994.
- [168] K. Watanabe, H. Ohnuma, H. Kimpara, H. Uetsuka, and K. Kunimori. Dynamics and kinetics of CO oxidation on $\text{Pd}(335)$: infrared chemiluminescence of CO_2 . *Surface Science*, 402-404:100–103, 1998.
- [169] T. Weiß. *Organische Monoschichten zur molekularen Erkennung*. PhD thesis, Eberhard-Karls-Universität Tübingen, Institut für Physikalische und Theoretische Chemie, Tübingen, 1998.
- [170] D. Wetzig, M. Rutkowski, W. Etterich, R. David, and H. Zacharias. Rotational alignment in associative desorption of H_2 from $\text{Pd}(100)$. *Surface Science*, 402-404:232–235, 1998.
- [171] G. Williams and G. S. V. Coles. Gas sensing properties of nanocrystalline metal oxide powders produced by a laser evaporation technique. *Journal of Materials Chemistry*, 8(7):1657–1664, 1998.
- [172] M. Wißing, M. Batzill, and K. J. Snowdon. Preparation by glancing incidence ion irradiation of CaF_2 surfaces with ångström-scale RMS roughness. *Nanotechnology*, 8:40–45, 1997.
- [173] K. Wolter, O. Seiferth, H. Kuhlenbeck, M. Bäumer, and H.-J. Freund. Infrared spectroscopic investigation of CO adsorbed on Pd aggregates deposited on an alumina model support. *Surface Science*, 399:190–198, 1998.
- [174] E. A. Wood. Vocabulary of Surface Crystallography. *Journal of Applied Physics*, 35(4):1306–1311, 1964.

- [175] D. P. Woodruff and T. A. Delchar. *Modern Techniques of Surface Science*. Cambridge University Press, Cambridge, 1986.
- [176] <http://www.matphys.kth.se/>.
- [177] <http://www.maxlab.lu.se/>.
- [178] <http://www.omicron-instruments.com/>.
- [179] <http://www.scienta.se/>.
- [180] <http://usx218.fysik.uu.se/>.
- [181] <http://www.vgmicrotech.com/>.
- [182] <http://www.vsw.co.uk/>.
- [183] Y. Yafet. Photoelectron spectrum, including that of Auger electrons, of Fano resonances in atoms. *Physical Review B*, 21(11):5023–5030, 1980.
- [184] Y. Yafet. Effect of shake-up transitions on the spectrum of Auger electrons in Fano resonances. *Physical Review B*, 23(7):3558–3559, 1981.
- [185] K. Yagi and H. Fukutani. Oxygen adsorption site of Pd(110)c(2×4)-O: analysis of ARUPS compared with STM-image. *Surface Science*, 412/413:489–494, 1998.
- [186] K. Yagi, D. Sekiba, and H. Fukutani. Adsorption and desorption kinetics of oxygen on the Pd(110) surface. *Surface Science*, 442:307–317, 1999.
- [187] Y. Yamaguchi, Y. Nagasawa, A. Murakami, and K. Tabata. Stability of oxygen anions and hydrogen abstraction from methane on reduced SnO₂(110) surface. *International Journal of Quantum Chemistry*, 69(5):669–678, 1998.
- [188] Y. Yamaguchi, Y. Nagasawa, S. Shimomura, K. Tabata, and E. Suzuki. A density functional theory study of the interaction of oxygen with a reduced SnO₂(110) surface. *Chemical Physics Letters*, 316:477–482, 2000.
- [189] N. Yamazoe, J. Fuchigami, and M. Kishikawa. Interactions of tin oxide surface with O₂, H₂O and H₂. *Surface Science*, 86:335–344, 1979.
- [190] Y. Yasui, M. Sawada, T. Aruga, N. Takagi, and M. Nishijina. Mechanisms of the CO oxidation on the Pd(110)c(2×4)-O surface. *Surface Science*, 397:295–305, 1998.
- [191] J. J. Yeh and I. Lindau. Atomic subshell photoionization cross sections and asymmetry parameters: $1 \leq Z \leq 103$. *Atomic Data and Nuclear Tables*, 32:1–155, 1985.

Appendix

List of Publications

Poster Contributions

1. J. Kappler, M. Sinner, A. Heilig, and W. Göpel. Stannic oxide nanocrystals for gas sensing devices. *Poster presented at ANfV'98 (Advanced Nanomaterials from Vapors)*. Uppsala, Sweden, 1998.
2. M. Sinner-Hettenbach, J. Kappler, N. Barsan, U. Weimar, and W. Göpel. Nanocrystalline SnO₂ gas-sensors: Influence of doping on electronic structure. *Poster presented at 114th Faraday Discussions*. Ambleside, UK, 1999.
3. M. Sinner-Hettenbach, N. Barsan, U. Weimar, T. Weiß, C. Ziegler, H. von Schenck, M. Göthelid, N. Papageorgiou, G. Terzian, J.-M. Layet, L. Giovanelli, and G. Le Lay. Resonant photoemission on doped and undoped SnO₂ gas sensors. *Poster presented at Eurosenors XIV*. Copenhagen, Denmark, 2000.

Oral Presentations

1. M. Sinner-Hettenbach. STM on SnO₂(110). *Joint seminary of Materials Physics at KTH Stockholm and Soft-X-ray Physics at Uppsala University*. Stockholm and Helsinki, 1999.
2. M. Sinner-Hettenbach, T. Weiß, N. Barsan, U. Weimar, M. Göthelid, G. Le Lay. STM, LEED and Photoemission results on SnO₂(110) and SnO₂ gas sensors. *presented at the*

SGS 2000 Workshop. Gliwice, Poland, 2000.

To be partly published in *Thin Solid Films*: M. Sinner-Hettenbach, N. Barsan, U. Weimar, T. Weiß, H. von Schenck, M. Göthelid, L. Giovanelli, and G. Le Lay. High Resolution Photoemission Study on SnO₂ Gas Sensors. *submitted to Thin Solid Films*, 2000.

Regular Papers

1. M. Sinner-Hettenbach, T. Weiß, N. Barsan, U. Weimar, H. von Schenck, M. Göthelid, L. Giovanelli, and G. Le Lay. Electronic structure of SnO₂(110)-4×1 and sputtered SnO₂(110) revealed by resonant photoemission. *in preparation*, 2000.
2. M. Sinner-Hettenbach, M. Göthelid, J. Weissenrieder, H. von Schenck, T. Weiß, N. Barsan, U. Weimar. Reconstruction process of oxygen-deficient SnO₂(110): A STM, LEED and XPS study. *submitted to Surface Science*, 2000.

Other Publications (not relevant for this thesis)

1. L. Giovanelli, H. von Schenck, M. Sinner-Hettenbach, N. Papageorgiou, M. Göthelid and G. Le Lay. Synchrotron radiation photoelectron spectroscopy study of PbPc thin films on InSb(100)-(4×2)/c(8×2). *submitted to Surface Science*, 2000.

Danksagung

Herrn Prof. Wolfgang Göpel möchte ich herzlich für die Stellung des Themas und die Betreuung dieser Arbeit bis zu seinem unerwarteten Tod danken. Frau Prof. Christiane Ziegler gilt mein Dank für die freundliche Übernahme des Themas und der Betreuung.

Herrn Prof. Klaus-Dieter Schierbaum gilt mein Dank sowohl für die Übernahme des Koreferats als auch für zahlreiche Diskussionen zu Beginn meiner Doktorarbeit.

Ganz herzlichen Dank an Dr. Tilo Weiß für die immer vorhandene Hilfsbereitschaft bei theoretischen und praktischen Problemen. Vielen Dank auch für viele Aufmunterungen und den Optimismus, besonders zu Beginn dieser Arbeit.

An Elke Nadler und Wolfgang Neu möchte ich meinen Dank für die persönliche Atmosphäre und für tatkräftige experimentelle Unterstützung während meiner Doktorarbeit im 'Großgerätelabor' richten.

Vielen Dank auch an Dr. Nicolae Barsan und Dr. Udo Weimar für die Bereitstellung der Sensoren, ihr Interesse an den Meßergebnissen und zahlreiche Diskussionen.

Special thanks to Dr. Mats Göthelid and Prof. Ulf Karlsson who invited me to their workgroup in Stockholm and provided optimum working conditions for the period of my stay. Thanks also for discussing my manuscripts.

For the practical help at the STM systems in Stockholm, I would like to thank Jonas Weissenrieder and Henrik von Schenck.

I especially would like to thank Prof. Guy Le Lay for the opportunity to perform the SRPES measurements on the SnO₂ samples and for his interest in discussing the results.

Bei Prof. Reinhard Helbig möchte ich mich ganz herzlich für die großzügige Bereitstellung der SnO₂ Einkristalle bedanken.

Meiner Frau Katrin möchte ich für ihre Geduld und Unterstützung während dieser Doktorarbeit danken.

Vielen Dank an Katrin Farian, die diese Arbeit Korrektur gelesen hat.

Michael Wandel gebührt mein Dank für seine schnelle Hilfe bei Netzwerk und Computerproblemen, Dr. Gerd Nötzel für seine zahlreichen Elektroniktips und allen noch nicht genannten Mitgliedern der Arbeitsgruppe für die gute Atmosphäre und für die Zusammenarbeit in den zurückliegenden Jahren.

Liste der akademischen Lehrer

Meine akademischen Lehrer waren:

M. Baumann, H. Clement, H. Fischer, K.-H. Gaukler, W. Göpel, P. Grabmayr, W.-D. Hartmann, R. Hübener, J. Ihringer, H. Kaul, D. Kern, K. Knorr, O. Lutz, G. Mertens, H. Müther, W. Nakel, H. Pfister, E. Plies, W. Prandl, H. Reinhardt, R. Schief, E. Schweda, A. Schwenk, G. Staudt, G. J. Wagner, D. Wharam, M. Wolff, C. Ziegler.

Lebenslauf

Angaben zur Person

Name: Martin Sinner-Hettenbach, geb. Sinner
Anschrift: Im Feuerhägle 18, 72072 Tübingen,
martin.sinner@ipc.uni-tuebingen.de
Geburtsdatum und -ort: 5. 2. 1972 in Tübingen
Familienstand: verheiratet
Staatsangehörigkeit: deutsch

Schulische Ausbildung

1978 – 1982 Grundsule: Ludwig-Krapf Schule in Tübingen-Derendingen
1982 – 1983 Kepler Gymnasium in Tübingen
1983 – 1991 Carlo-Schmid-Gymnasium in Tübingen
06/1991 Abiturprüfung

Weiterer Werdegang

10/1991 – 10/1992 Zivildienst im Deutschen Roten Kreuz Tübingen
10/1992 – 09/1997 Studium der Physik an der Eberhard-Karls-Universität Tübingen
11/1996 – 09/1997 Anfertigung der Diplomarbeit am Institut für Physikalische und Theoretische Chemie (IPC) der Universität Tübingen unter Anleitung von Prof. Wolfgang Göpel. Thema: 'Aufbau einer SIMS – Sekundärionenmassenspektrometrie – Apparatur'
01/1997 – 09/1997 Anstellung am IPC als ungeprüfte wissenschaftliche Hilfskraft
30. 9. 1997 Diplomprüfung in Physik
Seit 10/1997 Anfertigung der Doktorarbeit am Institut für Physikalische und Theoretische Chemie (IPC) der Universität Tübingen unter Anleitung von Prof. Wolfgang Göpel und Prof. Christiane Ziegler mit dem Titel: 'SnO₂(110) and Nano-SnO₂: Characterization by Surface Analytical Techniques'
10/1997 – 03/1998 Anstellung am IPC als geprüfte wissenschaftliche Hilfskraft
Seit 04/1998 Wissenschaftlicher Angestellter am IPC der Universität Tübingen als Mitarbeiter im europäischen Verbundprojekt 'Oxide Based Sensors and Catalysts'
10/1999 – 12/1999 Forschungsaufenthalt an der KTH Stockholm in der Materialphysik, Arbeitsgruppe von Prof. Ulf Karlsson

Tübingen, den 14. Dezember 2000